



CHORUS

This is the accepted manuscript made available via CHORUS. The article has been published as:

Dielectron production in Au + Au collisions at $\sqrt{s_{NN}}=200$ GeV

A. Adare *et al.* (PHENIX Collaboration
)

Phys. Rev. C **93**, 014904 — Published 11 January 2016

DOI: [10.1103/PhysRevC.93.014904](https://doi.org/10.1103/PhysRevC.93.014904)

Dielectron production in Au+Au collisions at $\sqrt{s_{NN}}=200$ GeV

1

2 A. Adare,¹³ C. Aidala,^{40,45} N.N. Ajitanand,⁶⁴ Y. Akiba,^{58,59} R. Akimoto,¹² J. Alexander,⁶⁴ M. Alfred,²⁴
3 H. Al-Ta'ani,⁵² A. Angerami,¹⁴ K. Aoki,^{33,58} N. Apadula,^{29,65} Y. Aramaki,^{12,58} H. Asano,^{36,58} E.C. Aschenauer,⁷
4 E.T. Atomssa,⁶⁵ R. Averbeck,⁶⁵ T.C. Awes,⁵⁴ B. Azmoun,⁷ V. Babintsev,²⁵ M. Bai,⁶ N.S. Bandara,⁴⁴ B. Banner,⁶⁵
5 K.N. Barish,⁸ B. Bassalleck,⁵¹ S. Bathe,^{5,59} V. Baublis,⁵⁷ S. Baumgart,⁵⁸ A. Bazilevsky,⁷ M. Beaumier,⁸
6 S. Beckman,¹³ R. Belmont,^{13,45,69} A. Berdnikov,⁶¹ Y. Berdnikov,⁶¹ D.S. Blau,³⁵ J.S. Bok,^{51,52,72} K. Boyle,⁵⁹
7 M.L. Brooks,⁴⁰ J. Bryslawskyj,⁵ H. Buesching,⁷ V. Bumazhnov,²⁵ S. Butsyk,⁵¹ S. Campbell,^{14,29,65} P. Castera,⁶⁵
8 C.-H. Chen,^{59,65} C.Y. Chi,¹⁴ M. Chiu,⁷ I.J. Choi,²⁶ J.B. Choi,¹⁰ S. Choi,⁶³ R.K. Choudhury,⁴ P. Christiansen,⁴²
9 T. Chujo,⁶⁸ O. Chvala,⁸ V. Cianciolo,⁵⁴ Z. Citron,^{65,70} B.A. Cole,¹⁴ M. Connors,⁶⁵ M. Csanád,¹⁸ T. Csörgő,⁷¹
10 S. Dairaku,^{36,58} D. Danley,⁵³ A. Datta,^{44,51} M.S. Daugherty,¹ G. David,⁷ K. DeBlasio,⁵¹ K. Dehmelt,⁶⁵
11 A. Denisov,²⁵ A. Deshpande,^{59,65} E.J. Desmond,⁷ K.V. Dharmawardane,⁵² O. Dietzsch,⁶² L. Ding,²⁹
12 A. Dion,^{29,65} P.B. Diss,⁴³ J.H. Do,⁷² M. Donadelli,⁶² L. D'Orazio,⁴³ O. Drapier,³⁷ A. Drees,⁶⁵ K.A. Drees,⁶
13 J.M. Durham,^{40,65} A. Durum,²⁵ S. Edwards,⁶ Y.V. Efremenko,⁵⁴ T. Engelmores,¹⁴ A. Enokizono,^{54,58,60}
14 S. Esumi,⁶⁸ K.O. Eyser,^{7,8} B. Fadem,⁴⁶ N. Feege,⁶⁵ D.E. Fields,⁵¹ M. Finger,⁹ M. Finger, Jr.,⁹ F. Fleuret,³⁷
15 S.L. Fokin,³⁵ J.E. Frantz,⁵³ A. Franz,⁷ A.D. Frawley,²⁰ Y. Fukao,⁵⁸ T. Fusayasu,⁴⁹ K. Gainey,¹ C. Gal,⁶⁵
16 P. Gallus,¹⁵ P. Garg,³ A. Garishvili,⁶⁶ I. Garishvili,³⁹ H. Ge,⁶⁵ F. Giordano,²⁶ A. Glenn,³⁹ X. Gong,⁶⁴ M. Gonin,³⁷
17 Y. Goto,^{58,59} R. Granier de Cassagnac,³⁷ N. Grau,² S.V. Greene,⁶⁹ M. Grosse Perdekamp,²⁶ T. Gunji,¹² L. Guo,⁴⁰
18 H.-Å. Gustafsson,^{42,*} T. Hachiya,⁵⁸ J.S. Haggerty,⁷ K.I. Hahn,¹⁹ H. Hamagaki,¹² H.F. Hamilton,¹ S.Y. Han,¹⁹
19 J. Hanks,^{14,65} S. Hasegawa,³⁰ T.O.S. Haseler,²¹ K. Hashimoto,^{58,60} E. Haslum,⁴² R. Hayano,¹² X. He,²¹
20 T.K. Hemmick,⁶⁵ T. Hester,⁸ J.C. Hill,²⁹ R.S. Hollis,⁸ K. Homma,²³ B. Hong,³⁴ T. Horaguchi,⁶⁸ Y. Hori,¹²
21 T. Hoshino,²³ N. Hotvedt,²⁹ J. Huang,⁷ S. Huang,⁶⁹ T. Ichihara,^{58,59} H. Inuma,³³ Y. Ikeda,^{58,68} K. Imai,³⁰
22 J. Imrek,¹⁷ M. Inaba,⁶⁸ A. Iordanova,⁸ D. Isenhower,¹ M. Issah,⁶⁹ D. Ivanishchev,⁵⁷ B.V. Jacak,⁶⁵ M. Javani,²¹
23 M. Jezghani,²¹ J. Jia,^{7,64} X. Jiang,⁴⁰ B.M. Johnson,⁷ K.S. Joo,⁴⁷ D. Jouan,⁵⁵ D.S. Jumper,²⁶ J. Kamin,⁶⁵
24 S. Kanda,¹² S. Kaneti,⁶⁵ B.H. Kang,²² J.H. Kang,⁷² J.S. Kang,²² J. Kapustinsky,⁴⁰ K. Karatsu,^{36,58} M. Kasai,^{58,60}
25 D. Kawall,^{44,59} A.V. Kazantsev,³⁵ T. Kempel,²⁹ J.A. Key,⁵¹ V. Khachatryan,⁶⁵ A. Khanzadeev,⁵⁷ K.M. Kijima,²³
26 B.I. Kim,³⁴ C. Kim,³⁴ D.J. Kim,³¹ E.-J. Kim,¹⁰ G.W. Kim,¹⁹ H.J. Kim,⁷² K.-B. Kim,¹⁰ M. Kim,⁶³ Y.-J. Kim,²⁶
27 Y.K. Kim,²² B. Kimelman,⁴⁶ E. Kinney,¹³ Á. Kiss,¹⁸ E. Kistenev,⁷ R. Kitamura,¹² J. Klatsky,²⁰ D. Kleinjan,⁸
28 P. Kline,⁶⁵ T. Koblesky,¹³ Y. Komatsu,^{12,33} B. Komkov,⁵⁷ J. Koster,²⁶ D. Kotchetkov,⁵³ D. Kotov,^{57,61} A. Král,¹⁵
29 F. Krizek,³¹ G.J. Kunde,⁴⁰ K. Kurita,^{58,60} M. Kurosawa,^{58,59} Y. Kwon,⁷² G.S. Kyle,⁵² R. Lacey,⁶⁴ Y.S. Lai,¹⁴
30 J.G. Lajoie,²⁹ A. Lebedev,²⁹ B. Lee,²² D.M. Lee,⁴⁰ J. Lee,¹⁹ K.B. Lee,³⁴ K.S. Lee,³⁴ S. Lee,⁷² S.H. Lee,⁶⁵ S.R. Lee,¹⁰
31 M.J. Leitch,⁴⁰ M.A.L. Leite,⁶² M. Leitgab,²⁶ B. Lewis,⁶⁵ X. Li,¹¹ S.H. Lim,⁷² L.A. Linden Levy,¹³ M.X. Liu,⁴⁰
32 B. Love,⁶⁹ D. Lynch,⁷ C.F. Maguire,⁶⁹ Y.I. Makdisi,⁶ M. Makek,^{70,73} A. Manion,⁶⁵ V.I. Manko,³⁵ E. Mannel,^{7,14}
33 S. Masumoto,^{12,33} M. McCumber,^{13,40} P.L. McGaughey,⁴⁰ D. McGlinchey,^{13,20} C. McKinney,²⁶ A. Meles,⁵²
34 M. Mendoza,⁸ B. Meredith,²⁶ Y. Miake,⁶⁸ T. Mibe,³³ A.C. Mignerey,⁴³ A. Milov,⁷⁰ D.K. Mishra,⁴ J.T. Mitchell,⁷
35 Y. Miyachi,^{58,67} S. Miyasaka,^{58,67} S. Mizuno,^{58,68} A.K. Mohanty,⁴ S. Mohapatra,⁶⁴ P. Montuenga,²⁶ H.J. Moon,⁴⁷
36 T. Moon,⁷² D.P. Morrison,^{7,†} S. Morschwiller,⁴⁶ T.V. Moukhanova,³⁵ T. Murakami,^{36,58} J. Murata,^{58,60} A. Mwai,⁶⁴
37 T. Nagae,³⁶ S. Nagamiya,^{33,58} K. Nagashima,²³ J.L. Nagle,^{13,‡} M.I. Nagy,^{18,71} I. Nakagawa,^{58,59} H. Nakagomi,^{58,68}
38 Y. Nakamiya,²³ K.R. Nakamura,^{36,58} T. Nakamura,⁵⁸ K. Nakano,^{58,67} C. Nattrass,⁶⁶ A. Nederlof,⁴⁶
39 P.K. Netrakanti,⁴ M. Nishashi,^{23,58} T. Niida,⁶⁸ S. Nishimura,¹² R. Nouicer,^{7,59} T. Novák,^{32,71} N. Novitzky,^{31,65}
40 A.S. Nyanin,³⁵ E. O'Brien,⁷ C.A. Ogilvie,²⁹ K. Okada,⁵⁹ J.D. Orjuela Koop,¹³ J.D. Osborn,⁴⁵ A. Oskarsson,⁴²
41 M. Ouchida,^{23,58} K. Ozawa,^{12,33} R. Pak,⁷ V. Pantuev,²⁷ V. Papavassiliou,⁵² B.H. Park,²² I.H. Park,¹⁹ J.S. Park,⁶³
42 S. Park,⁶³ S.K. Park,³⁴ S.F. Pate,⁵² L. Patel,²¹ M. Patel,²⁹ H. Pei,²⁹ J.-C. Peng,²⁶ H. Pereira,¹⁶ D.V. Perepelitsa,^{7,14}
43 G.D.N. Perera,⁵² D.Yu. Peressouanko,³⁵ J. Perry,²⁹ R. Petti,^{7,65} C. Pinkenburg,⁷ R. Pinson,¹ R.P. Pisani,⁷
44 M. Proissl,⁶⁵ M.L. Purschke,⁷ H. Qu,¹ J. Rak,³¹ B.J. Ramson,⁴⁵ I. Ravinovich,⁷⁰ K.F. Read,^{54,66} D. Reynolds,⁶⁴
45 V. Riabov,^{50,57} Y. Riabov,^{57,61} E. Richardson,⁴³ T. Rinn,²⁹ D. Roach,⁶⁹ G. Roche,^{41,*} S.D. Rolnick,⁸ M. Rosati,²⁹
46 Z. Rowan,⁵ J.G. Rubin,⁴⁵ B. Sahlmueller,⁶⁵ N. Saito,³³ T. Sakaguchi,⁷ H. Sako,³⁰ V. Samsonov,^{50,57} M. Sano,⁶⁸
47 M. Sarsour,²¹ S. Sato,³⁰ S. Sawada,³³ B. Schaefer,⁶⁹ B.K. Schmoll,⁶⁶ K. Sedgwick,⁸ R. Seidl,^{58,59} A. Sen,^{21,66}
48 R. Seto,⁸ P. Sett,⁴ A. Sexton,⁴³ D. Sharma,^{65,70} I. Shein,²⁵ T.-A. Shibata,^{58,67} K. Shigaki,²³ M. Shimomura,^{29,48,68}
49 K. Shoji,^{36,58} P. Shukla,⁴ A. Sickles,^{7,26} C.L. Silva,^{29,40} D. Silvermyr,^{42,54} K.S. Sim,³⁴ B.K. Singh,³ C.P. Singh,³
50 V. Singh,³ M. Slunečka,⁹ M. Snowball,⁴⁰ R.A. Soltz,³⁹ W.E. Sondheim,⁴⁰ S.P. Sorensen,⁶⁶ I.V. Sourikova,⁷
51 P.W. Stankus,⁵⁴ E. Stenlund,⁴² M. Stepanov,^{44,*} A. Ster,⁷¹ S.P. Stoll,⁷ T. Sugitate,²³ A. Sukhanov,⁷ T. Sumita,⁵⁸
52 J. Sun,⁶⁵ J. Sziklai,⁷¹ E.M. Takagui,⁶² A. Takahara,¹² A. Taketani,^{58,59} Y. Tanaka,⁴⁹ S. Taneja,⁶⁵ K. Tanida,^{59,63}
53 M.J. Tannenbaum,⁷ S. Tarafdar,^{3,70} A. Taranenko,^{50,64} E. Tennant,⁵² H. Themann,⁶⁵ R. Tieulent,²¹ A. Timilsina,²⁹

54 T. Todoroki,^{58,68} L. Tomášek,²⁸ M. Tomášek,^{15,28} H. Torii,²³ C.L. Towell,¹ R. Towell,¹ R.S. Towell,¹ I. Tserruya,⁷⁰
 55 Y. Tsuchimoto,¹² T. Tsuji,¹² C. Vale,⁷ H.W. van Hecke,⁴⁰ M. Vargyas,¹⁸ E. Vazquez-Zambrano,¹⁴
 56 A. Veicht,¹⁴ J. Velkovska,⁶⁹ R. Vértesi,⁷¹ M. Virius,¹⁵ A. Vossen,²⁶ V. Vrba,^{15,28} E. Vznuzdaev,⁵⁷
 57 X.R. Wang,^{52,59} D. Watanabe,²³ K. Watanabe,⁶⁸ Y. Watanabe,^{58,59} Y.S. Watanabe,^{12,33} F. Wei,^{29,52} R. Wei,⁶⁴
 58 A.S. White,⁴⁵ S.N. White,⁷ D. Winter,¹⁴ S. Wolin,²⁶ C.L. Woody,⁷ M. Wysocki,^{13,54} B. Xia,⁵³ L. Xue,²¹
 59 S. Yalcin,⁶⁵ Y.L. Yamaguchi,^{12,58,65} R. Yang,²⁶ A. Yanovich,²⁵ J. Ying,²¹ S. Yokkaichi,^{58,59} J.H. Yoo,³⁴ I. Yoon,⁶³
 60 Z. You,⁴⁰ I. Younus,^{38,51} H. Yu,⁵⁶ I.E. Yushmanov,³⁵ W.A. Zajc,¹⁴ A. Zelenski,⁶ S. Zhou,¹¹ and L. Zou⁸

(PHENIX Collaboration)

¹Abilene Christian University, Abilene, Texas 79699, USA

²Department of Physics, Augustana University, Sioux Falls, South Dakota 57197, USA

³Department of Physics, Banaras Hindu University, Varanasi 221005, India

⁴Bhabha Atomic Research Centre, Bombay 400 085, India

⁵Baruch College, City University of New York, New York, New York, 10010 USA

⁶Collider-Accelerator Department, Brookhaven National Laboratory, Upton, New York 11973-5000, USA

⁷Physics Department, Brookhaven National Laboratory, Upton, New York 11973-5000, USA

⁸University of California-Riverside, Riverside, California 92521, USA

⁹Charles University, Ovocný trh 5, Praha 1, 116 36, Prague, Czech Republic

¹⁰Chonbuk National University, Jeonju, 561-756, Korea

¹¹Science and Technology on Nuclear Data Laboratory, China Institute of Atomic Energy, Beijing 102413, P. R. China

¹²Center for Nuclear Study, Graduate School of Science, University of Tokyo, 7-3-1 Hongo, Bunkyo, Tokyo 113-0033, Japan

¹³University of Colorado, Boulder, Colorado 80309, USA

¹⁴Columbia University, New York, New York 10027 and Nevis Laboratories, Irvington, New York 10533, USA

¹⁵Czech Technical University, Zikova 4, 166 36 Prague 6, Czech Republic

¹⁶Dapnia, CEA Saclay, F-91191, Gif-sur-Yvette, France

¹⁷Debrecen University, H-4010 Debrecen, Egyetem tér 1, Hungary

¹⁸ELTE, Eötvös Loránd University, H-1117 Budapest, Pázmány P. s. 1/A, Hungary

¹⁹Ewha Womans University, Seoul 120-750, Korea

²⁰Florida State University, Tallahassee, Florida 32306, USA

²¹Georgia State University, Atlanta, Georgia 30303, USA

²²Hanyang University, Seoul 133-792, Korea

²³Hiroshima University, Kagamiyama, Higashi-Hiroshima 739-8526, Japan

²⁴Department of Physics and Astronomy, Howard University, Washington, DC 20059, USA

²⁵IHEP Protvino, State Research Center of Russian Federation, Institute for High Energy Physics, Protvino, 142281, Russia

²⁶University of Illinois at Urbana-Champaign, Urbana, Illinois 61801, USA

²⁷Institute for Nuclear Research of the Russian Academy of Sciences, prospekt 60-letiya Oktyabrya 7a, Moscow 117312, Russia

²⁸Institute of Physics, Academy of Sciences of the Czech Republic, Na Slovance 2, 182 21 Prague 8, Czech Republic

²⁹Iowa State University, Ames, Iowa 50011, USA

³⁰Advanced Science Research Center, Japan Atomic Energy Agency, 2-4

Shirakata Shirane, Tokai-mura, Naka-gun, Ibaraki-ken 319-1195, Japan

³¹Helsinki Institute of Physics and University of Jyväskylä, P.O.Box 35, FI-40014 Jyväskylä, Finland

³²Károly Róberts University College, H-3200 Gyöngyös, Mátraiút 36, Hungary

³³KEK, High Energy Accelerator Research Organization, Tsukuba, Ibaraki 305-0801, Japan

³⁴Korea University, Seoul, 136-701, Korea

³⁵National Research Center "Kurchatov Institute", Moscow, 123098 Russia

³⁶Kyoto University, Kyoto 606-8502, Japan

³⁷Laboratoire Leprince-Ringuet, Ecole Polytechnique, CNRS-IN2P3, Route de Saclay, F-91128, Palaiseau, France

³⁸Physics Department, Lahore University of Management Sciences, Lahore 54792, Pakistan

³⁹Lawrence Livermore National Laboratory, Livermore, California 94550, USA

⁴⁰Los Alamos National Laboratory, Los Alamos, New Mexico 87545, USA

⁴¹LPC, Université Blaise Pascal, CNRS-IN2P3, Clermont-Fd, 63177 Aubiere Cedex, France

⁴²Department of Physics, Lund University, Box 118, SE-221 00 Lund, Sweden

⁴³University of Maryland, College Park, Maryland 20742, USA

⁴⁴Department of Physics, University of Massachusetts, Amherst, Massachusetts 01003-9337, USA

⁴⁵Department of Physics, University of Michigan, Ann Arbor, Michigan 48109-1040, USA

⁴⁶Muhlenberg College, Allentown, Pennsylvania 18104-5586, USA

⁴⁷Myongji University, Yongin, Kyonggido 449-728, Korea

⁴⁸Nara Women's University, Kita-uoya Nishi-machi Nara 630-8506, Japan

⁴⁹Nagasaki Institute of Applied Science, Nagasaki-shi, Nagasaki 851-0193, Japan

⁵⁰National Research Nuclear University, MEPhI, Moscow Engineering Physics Institute, Moscow, 115409, Russia

⁵¹University of New Mexico, Albuquerque, New Mexico 87131, USA

⁵²New Mexico State University, Las Cruces, New Mexico 88003, USA

⁵³Department of Physics and Astronomy, Ohio University, Athens, Ohio 45701, USA

⁵⁴ Oak Ridge National Laboratory, Oak Ridge, Tennessee 37831, USA

⁵⁵ IPN-Orsay, Univ. Paris-Sud, CNRS/IN2P3, Universit Paris-Saclay, BP1, F-91406, Orsay, France

⁵⁶ Peking University, Beijing 100871, P. R. China

⁵⁷ PNPI, Petersburg Nuclear Physics Institute, Gatchina, Leningrad region, 188300, Russia

⁵⁸ RIKEN Nishina Center for Accelerator-Based Science, Wako, Saitama 351-0198, Japan

⁵⁹ RIKEN BNL Research Center, Brookhaven National Laboratory, Upton, New York 11973-5000, USA

⁶⁰ Physics Department, Rikkyo University, 3-34-1 Nishi-Ikebukuro, Toshima, Tokyo 171-8501, Japan

⁶¹ Saint Petersburg State Polytechnic University, St. Petersburg, 195251 Russia

⁶² Universidade de São Paulo, Instituto de Física, Caixa Postal 66318, São Paulo CEP05315-970, Brazil

⁶³ Department of Physics and Astronomy, Seoul National University, Seoul 151-742, Korea

⁶⁴ Chemistry Department, Stony Brook University, SUNY, Stony Brook, New York 11794-3400, USA

⁶⁵ Department of Physics and Astronomy, Stony Brook University, SUNY, Stony Brook, New York 11794-3800, USA

⁶⁶ University of Tennessee, Knoxville, Tennessee 37996, USA

⁶⁷ Department of Physics, Tokyo Institute of Technology, Oh-okayama, Meguro, Tokyo 152-8551, Japan

⁶⁸ Center for Integrated Research in Fundamental Science and Engineering, University of Tsukuba, Tsukuba, Ibaraki 305, Japan

⁶⁹ Vanderbilt University, Nashville, Tennessee 37235, USA

⁷⁰ Weizmann Institute, Rehovot 76100, Israel

⁷¹ Institute for Particle and Nuclear Physics, Wigner Research Centre for Physics, Hungarian Academy of Sciences (Wigner RCP, RMKI) H-1525 Budapest 114, POBox 49, Budapest, Hungary

⁷² Yonsei University, IPAP, Seoul 120-749, Korea

⁷³ University of Zagreb, Faculty of Science, Department of Physics, Bijenička 32, HR-10002 Zagreb, Croatia

We present measurements of e^+e^- production at midrapidity in Au+Au collisions at $\sqrt{s_{NN}} = 200$ GeV. The invariant yield is studied within the PHENIX detector acceptance over a wide range of mass ($m_{ee} < 5$ GeV/ c^2) and pair transverse momentum ($p_T < 5$ GeV/ c), for minimum bias and for five centrality classes. The e^+e^- yield is compared to the expectations from known sources. In the low-mass region ($m_{ee} = 0.30$ – 0.76 GeV/ c^2) there is an enhancement that increases with centrality and is distributed over the entire pair p_T range measured. It is significantly smaller than previously reported by the PHENIX experiment and amounts to $2.3 \pm 0.4(\text{stat}) \pm 0.4(\text{syst}) \pm 0.2^{\text{model}}$ or to $1.7 \pm 0.3(\text{stat}) \pm 0.3(\text{syst}) \pm 0.2^{\text{model}}$ for minimum bias collisions when the open heavy flavor contribution is calculated with PYTHIA or MC@NLO, respectively. The inclusive mass and p_T distributions as well as the centrality dependence are well reproduced by model calculations where the enhancement mainly originates from the melting of the ρ meson resonance as the system approaches chiral symmetry restoration. In the intermediate-mass region ($m_{ee} = 1.2$ – 2.8 GeV/ c^2), the data hint at a significant contribution in addition to the yield from the semileptonic decays of heavy flavor mesons.

PACS numbers: 25.75.Dw

* Deceased

† PHENIX Co-Spokesperson: morrison@bnl.gov

‡ PHENIX Co-Spokesperson: jamie.nagle@colorado.edu

I. INTRODUCTION

152 Dileptons are important diagnostic tools of the Quark Gluon Plasma (QGP) formed in ultra-relativistic heavy ion
 153 collisions [1]. They are unique observables for their sensitivity to the chiral symmetry restoration phase transition
 154 expected to take place together with, or at similar conditions to, the deconfinement phase transition [2, 3]. When
 155 chiral symmetry is restored, the chiral doublets, such as the ρ and the a_1 mesons, become degenerate in mass. As the
 156 a_1 meson is very difficult to observe experimentally, the ρ meson is the main observable in this context. Due to its very
 157 short lifetime ($\tau \sim 1.3$ fm/ c), the ρ meson quickly decays after its formation and is therefore a sensitive probe of the
 158 medium where it is formed. The ρ meson is mostly produced close to the phase boundary and possible modifications
 159 of its spectral function in the high temperature and density conditions prevailing there are thus imprinted in its decay
 160 products. The decay into dileptons, as opposed to hadrons, is of particular interest as they escape unaffected by the
 161 interaction region, thus carrying this information to the detectors.

162 Dileptons are sensitive to the thermal radiation emitted by the system, both the partonic thermal radiation (quark
 163 annihilation into virtual photons, $q\bar{q} \rightarrow \gamma^* \rightarrow l^+l^-$) emitted in the early stage of the collisions as well as the thermal
 164 radiation emitted later in the collision by the hadronic system. The main channel of the latter is pion annihilation,
 165 mediated through vector meson dominance by the ρ meson ($\pi^+\pi^- \rightarrow \rho \rightarrow \gamma^* \rightarrow l^+l^-$). Dileptons are produced by a
 166 variety of sources all along the entire history of the collision and it is necessary to know precisely all these sources in
 167 order to single out the interesting signals characteristic of the QGP related to chiral symmetry restoration or thermal
 168 radiation [4].

169 The CERES experiment pioneered the study of dielectrons at the Super Proton Synchrotron (SPS). A strong
 170 enhancement of low-mass electron pairs ($m_{ee} < 1$ GeV/ c^2) with respect to the cocktail of expected hadronic sources,
 171 was found in all nuclear systems studied, in S+Au collisions at 200 AGeV [5], in Pb+Au collisions at 158 AGeV [6, 7]
 172 and in Pb+Au collisions at 40 AGeV [8]. The enhancement was confirmed and further studied by the high statistics
 173 NA60 experiment that measured dimuons in In+In collisions at 160 AGeV [9–12]. In both experiments, the low-mass
 174 dilepton enhancement is explained by in-medium modification of the ρ meson spectral function [13–18]. The data
 175 rule out the conjectured dropping mass of the ρ meson as the system approaches chiral symmetry restoration [19–21].
 176 Instead, the data are well reproduced by a scenario in which the ρ meson copiously produced by $\pi^+\pi^-$ annihilation is
 177 broadened by the scattering off baryons in the dense hadronic medium. The low-mass dilepton excess is thus identified
 178 as the thermal radiation signal from the hadron gas phase with a modified ρ meson spectral function. A recent paper
 179 shows that in-medium modifications of vector and axial vector spectral functions lead to degeneracy of the ρ and a_1
 180 meson masses providing a direct link between the broadening of the ρ meson spectral function and the restoration of
 181 chiral symmetry [22].

182 NA60 found also an excess at higher masses ($m_{l+l^-} = 1-3$ GeV/ c^2). Using precise vertex information this excess
 183 was associated with a prompt source originating at the vertex, as opposed to semi-leptonic decays of D mesons that
 184 originate at displaced vertices. The excess can be explained as thermal radiation from the QGP [9–12, 15] but other
 185 interpretations based on hadronic models, similar to those that explain the low mass excess [13, 14], or on hadronic
 186 rates constrained by chiral symmetry considerations [16] can also reproduce the data.

187 At the Relativistic Heavy Ion Collider (RHIC), the PHENIX experiment reported a strong enhancement of low
 188 mass pairs in Au+Au collisions at $\sqrt{s_{NN}} = 200$ GeV [23]. In the 0%–10% most central collisions, where the excess
 189 is concentrated, the enhancement factor, defined as the ratio of the measured yield over the cocktail yield reaches an
 190 average value of $7.6 \pm 0.5(\text{stat}) \pm 1.3(\text{syst}) \pm 1.5$ (cocktail) in the mass range $m_{ee} = 0.15-0.75$ GeV/ c^2 . All models
 191 that successfully reproduce the SPS results fail to explain the PHENIX data [23, 24].

192 The PHENIX result [23] was characterized by a considerable hadron contamination of the electron sample and by
 193 a small signal to background (S/B) ratio. In an effort to improve upon this measurement, a hadron-blind detector
 194 (HBD) was developed and installed in the PHENIX experiment [25–27]. The HBD provides additional electron
 195 identification, additional hadron rejection and improves the signal sensitivity.

196 In this paper we present dielectron results obtained with the HBD in 2010 for Au+Au collisions at $\sqrt{s_{NN}} = 200$ GeV.
 197 The paper is organized as follows. Section II describes the PHENIX detector with special emphasis on the HBD. In
 198 Section III we give a detailed account of the various steps of the data analysis including electron identification, pair
 199 cuts and background subtraction that is the crucial step in this analysis. The raw mass spectra, efficiency corrections
 200 and systematic uncertainties of the data are also discussed in this section. Section IV describes the procedures used
 201 to calculate the expected dielectron yield from the known hadronic sources. The results, including invariant mass
 202 spectra, p_T distributions and centrality dependence, are presented in Section V. In the same section, the results are
 203 discussed with respect to previously published results and compared to available theoretical calculations. A summary
 204 is given in Section VI.

II. PHENIX DETECTOR

205

206 Figure 1 shows a schematic beam view of the PHENIX central arm detector, as used during 2010 data taking.
 207 A detailed description of the detector, except the HBD, can be found in [28]. In this section, we give only a brief
 208 description of the PHENIX sub-systems relevant for the present analysis: global detectors, central magnet, central arm
 209 detectors, including drift chambers (DC), pad chambers (PC), ring-imaging Čerenkov (RICH) detectors, time-of-flight
 210 (TOF) detectors and electromagnetic calorimeters (EMCAL) and the HBD.

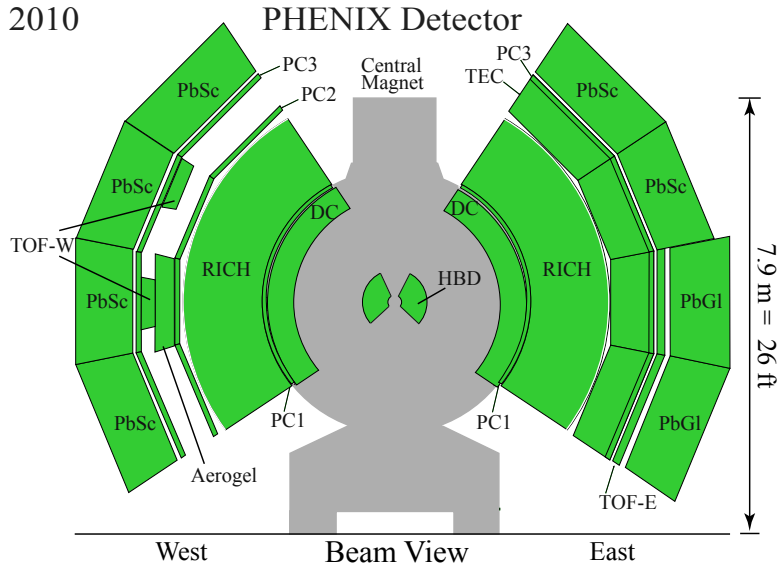


FIG. 1. (Color online) Beam view (at $z = 0$) of the PHENIX central arm spectrometers during 2010 data taking.

211

A. Global detectors

212 The measurement of the collision-vertex position, time, and centrality, as well as the minimum-bias (MB) trigger,
 213 is provided by two beam-beam counters (BBC) [29]. Each BBC comprises 64 quartz Čerenkov counters, located
 214 at ± 144 cm along the beam axis from the center of PHENIX, with 2π azimuthal coverage over the pseudorapidity
 215 interval $3.0 < |\eta| < 3.9$. The collision-vertex position along the beam direction z is determined from the difference
 216 of the average hit time of the photomultiplier tubes (PMTs) between the north and the south BBC. The z -vertex
 217 resolution ranges from ~ 0.5 cm in central Au+Au collisions to ~ 2 cm in $p+p$ collisions. The MB trigger requires a
 218 coincidence between at least two hits in each of the BBC arrays thus capturing $92 \pm 3\%$ of the total inelastic cross
 219 section [30].

220

B. Central magnet

221 The PHENIX central magnet comprises two pairs of concentric coils, an inner coil pair and an outer coil pair, that
 222 can be operated independently and create an axial magnetic field parallel to the beam axis [31]. The coils are usually
 223 operated with current flowing in the same direction (the $++$ or $--$ configuration) so that their magnetic fields add
 224 together. For the dilepton measurement with the HBD in the 2010 run, the coils were operated with equal currents
 225 flowing in opposite directions. In this so called $+ -$ configuration, the inner coil counteracts the action of the outer
 226 coil so that their magnetic fields cancel each other, creating an almost field free region in the inner space extending
 227 from the beam axis out to a radial distance of ~ 60 cm where the inner coil is located (see Fig. 1 of Ref. [27]). The
 228 field free region preserves the opening angle of e^+e^- pairs and this is an essential pre-requisite for the operation of
 229 the HBD. The HBD exploits the fact that the opening angle of e^+e^- pairs originating from γ conversions or from π^0
 230 Dalitz decays is very small. When only one of the two tracks is reconstructed in the central arms, the HBD can reject
 231 them by applying an opening angle cut or a double signal cut on the HBD hits (see Section II D). In this configuration
 232 however, the total field integral is $\int B \cdot dl = 0.43$ Tm, about 40% of the value in the $++$ configuration.

C. Central arm detectors

PHENIX measurements at midrapidity are made with two central arm spectrometers, as shown in Fig. 1. Each central arm covers pseudorapidity $|\eta| < 0.35$ and azimuthal angle $\Delta\phi = \pi/2$.

Charged-particle tracks are reconstructed using hit information from the DC, the first layer of PC (PC1) and the collision point along the z-direction [32]. The DCs are located outside the magnetic field in the radial distance 2.02–2.46 m from the beam axis. They provide an accurate measurement of the particle trajectory in the plane perpendicular to the beam axis. The PC1s are multiwire proportional chambers located just behind the DC at 2.47–2.52 m in radial distance from the beam axis [33]. They provide a three dimensional space point that is used to determine the track origin along the beam axis. The transverse momentum (p_T) of each particle is determined from the bending of its trajectory in the azimuthal direction. The total momentum p is determined by combining p_T with the polar angle information of PC1 and the vertex position z . The reconstructed tracks are projected onto the HBD (see next subsection) and onto the central-arm detectors that provide electron identification: RICH, EMCal, and TOF.

The RICH is the primary central-arm detector used for electron identification in PHENIX [34], and is located in the radial region of 2.5–4.1 m, just behind PC1. The RICH uses CO₂ as the gas radiator at atmospheric pressure, and has a Čerenkov threshold of $\gamma = 35$. This corresponds to a momentum threshold of 18 MeV/ c for electrons and 4.7 GeV/ c for pions. Two spherical mirrors reflect the Čerenkov light and focus it onto two arrays of 1280 PMTs each located outside the acceptance on each side of the RICH entrance window. The average number of hit PMTs per electron track is ~ 5 , and the average number of photo-electrons detected is ~ 10 . Below the pion threshold, the pion rejection is $\sim 10^4$ in $p+p$ or low multiplicity collisions. However, in high-multiplicity collisions, hadron tracks are misidentified as electrons when their trajectory is nearly parallel to that of a genuine electron. This effect limits the e/π separation to $\sim 10^{-3}$ in central Au+Au collisions and requires special care as described below.

The EMCal measures the energy deposited by electrons and their shower shape [35]. It comprises eight sectors each covering $\Delta\phi \approx \pi/8$ in azimuth, where six sectors are made from lead-scintillator (PbSc) with an energy resolution $4.5\% \oplus 8.3\%/\sqrt{E}$ [GeV] and two are lead-glass (PbGl) with an energy resolution $4.3\% \oplus 7.7\%/\sqrt{E}$ [GeV]. The radial distance from the beam axis is 5.10 m for PbSc and 5.50 m for PbGl (see Fig. 1). The matching of the measured energy to the track momentum is used to identify electrons. The latter are all relativistic in the accepted momentum range ($p_T > 0.2$ GeV/ c), hence the energy-to-momentum ratio is close to unity.

To further separate electrons and hadrons we use the time-of-flight information from the PbSc part of the EMCal which covers 75% of the acceptance but has a valid time response for 64% of the acceptance. In addition, we use the time-of-flight information from the TOF-east detector (TOF-E) [36] covering an additional 16% of the acceptance. The former has a time resolution of ~ 450 ps, while the latter has a resolution of ~ 150 ps. The rest of the acceptance, 9%, does not have a usable TOF coverage, because the time resolution of ~ 700 ps provided by PbGl detectors is not sufficient for an effective separation of electrons and hadrons.

D. The Hadron Blind Detector

The HBD was installed in PHENIX prior to 2010. A detailed description of the concept, construction and performance of the HBD is given in Ref. [27]. Only a brief account is given here with emphasis on the specific aspects relevant to the present analysis.

The HBD provides additional electron identification and additional hadron rejection to the central arm detectors. Its main task is to recognize and reject γ conversions and π^0 Dalitz decays which are the dominant sources of the combinatorial background. Very often, only one of the two tracks of an e^+e^- pair from these sources is detected in the central arm, whereas the second one is lost because it falls out of the acceptance, is curled by the magnetic field or is not detected due to the inability to reconstruct low momentum tracks with $p_T < 200$ MeV/ c . The HBD exploits the fact that most of these pairs have a very small opening angle and thus produce two overlapping hits in the HBD, resulting in a charge response with an amplitude double the one corresponding to a single hit. Being sensitive to electrons down to very low momentum (see below), the HBD can detect both tracks and can effectively reject them by applying a double hit cut on the HBD signal. On the other hand, decays with a large opening angle between the electron and positron produce two well separated single hits on the HBD pad plane as illustrated in Fig. 2. The ability to distinguish single from double hits is one of the main performance parameters of the HBD. This is illustrated in Fig. 3, which shows the HBD response to single and double electron hits in real data. Single and double hits are selected from reconstructed low-mass pairs with large (> 100 mrad) and small (< 50 mrad) opening angles, respectively.

The HBD is a Čerenkov detector. It has a 50 cm long radiator directly coupled, in a windowless configuration, to a triple gas-electron-multiplier (GEM) detector [37] which has a CsI photocathode evaporated on the top face of the

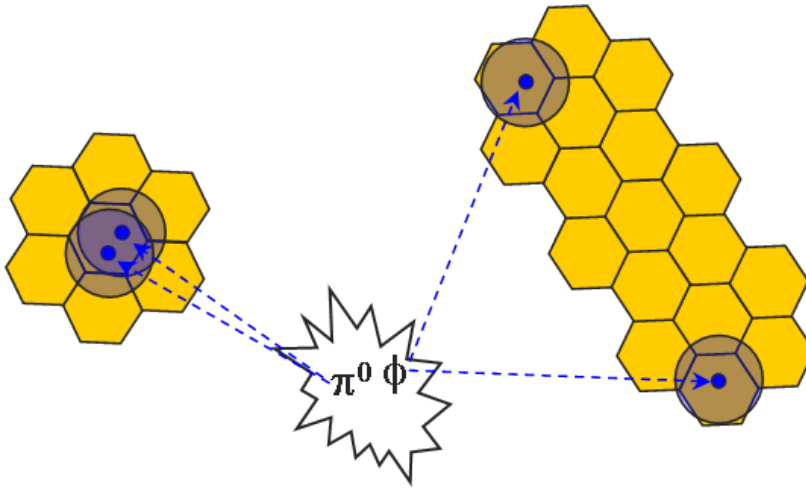


FIG. 2. (Color online) Sketch illustrating the HBD response to an e^+e^- pair from π^0 Dalitz decay and from a ϕ meson decay. The circles represent the Čerenkov blobs whereas the hexagons are the hexagonal pads of the HBD readout plane.

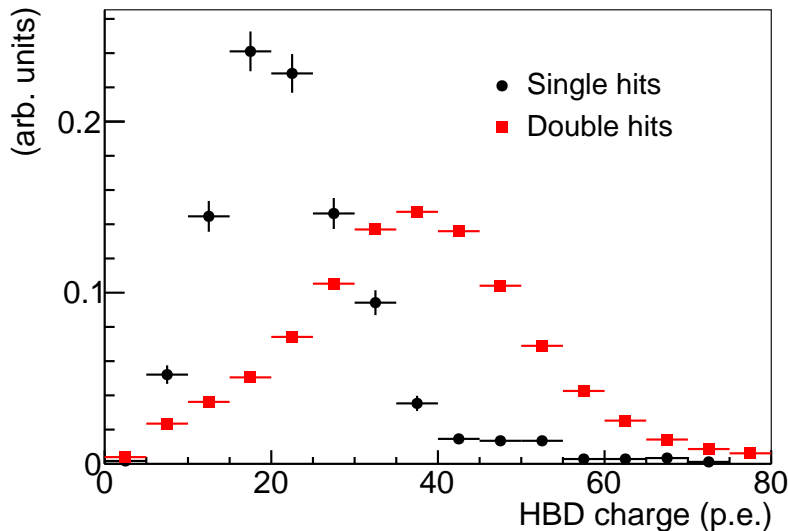


FIG. 3. (Color online) HBD response to single electron hits and double electron hits in the 60%–92% centrality bin. The two distributions are normalized to give an integral yield of one.

287 upper-most GEM foil and pad readout at the bottom of the GEM stack (see Fig. 4). The HBD uses pure CF_4 at
 288 atmospheric pressure that has an average Čerenkov threshold of $\gamma = 28.8$ over the detector bandwidth, corresponding
 289 to a momentum threshold of $\sim 15 \text{ MeV}/c$ for electrons and $\sim 4.0 \text{ GeV}/c$ for pions. In this scheme, Čerenkov radiation
 290 from particles passing through the radiator is directly collected on the photocathode forming a circular blob image
 291 rather than a ring as in a RICH detector. The pad readout plane comprises hexagonal cells with a hexagon side of
 292 1.55 cm . One cell subtends an opening angle of approximately 50 mrad and has an area of 6.2 cm^2 , comparable to
 293 the blob size which has a maximum area of 10 cm^2 . The electron response of the HBD is thus typically distributed
 294 over a maximum of 3 readout cells and subtends a maximum opening angle of 75 mrad .

295 The hadron blindness property of the HBD is achieved by operating the detector in reverse bias mode where the
 296 mesh defining the detection volume is set at a lower voltage with respect to the CsI photocathode [25, 26] (see Fig. 4).
 297 Consequently, the ionization electrons produced by charged particles in the drift region defined by the entrance mesh
 298 and the photocathode are mostly repelled towards the mesh. Only the ionization electrons created in a thin layer
 299 of $\sim 100 \mu\text{m}$ above the photocathode are collected and amplified by the GEM stack leading to a very small signal,
 300 equivalent to a few p.e., localized in one single cell of the pad plane.

301 The choice of CF_4 in a windowless configuration as the common gas for the radiator and the detector amplification

FIG. 4. (Color online) Triple GEM stack operated in reverse bias mode where ionization electrons produced by a charged particle are repelled toward the mesh.

medium, results in a large bandwidth of UV photon sensitivity from 6.2 eV (the threshold of the CsI photocathode) up to 11.1 eV (the CF_4 cut-off). This translates into an average yield of 20 photo-electrons (p.e.) per electron, as shown in Fig. 3, corresponding to a measured figure of merit N_0 of 330 cm^{-1} , very high for a gas Čerenkov detector [27].

The HBD is located close to the interaction vertex, in the field-free region, starting immediately after the beam pipe at $r = 5 \text{ cm}$ and extending up to $r = 60 \text{ cm}$. The detector comprises two identical arms, each covering 112.5° in azimuth and ± 0.45 units of pseudorapidity. The active area of each arm is subdivided into 10 detector modules, 5 along the azimuthal axis and 2 along the z axis. With this segmentation, each detector module is $\sim 23 \times 27 \text{ cm}^2$ in size. The material budget (See Table I) in front of the GEM detectors is 0.62% of a radiation length dominated by the CF_4 contribution of 0.56%. To this, one has to add the contribution of the GEM stack, the vessel back plane and the front-end electronics attached to the vessel to give a total of 2.4% of a radiation length for the entire detector.

TABLE I. Material budget of the HBD within the central arm acceptance [27].

Component	Radiation length (%)
Window (aclar/kapton)	0.04
Gas (CF_4)	0.56
GEM stack	0.42
Vessel back plane + front-end electronics	1.4
Total	2.4

Good gain calibration is crucial to achieve the best possible separation between single and double hits in the HBD. Gain variations occur as a function of time due to two main factors: (i) variations of temperature and pressure and (ii) charging effects of the GEM foils produce an initial rise of the gain after switching on the HV, that can last for

several hours before stabilizing [38]. These gain variations are taken into account by performing a gain calibration of each module every three minutes during data collection. This is done by exploiting the scintillation light produced by charged particles traversing the CF_4 radiator. The scintillation signal is easily identified by the characteristic exponential shape of single electrons in the HBD pulse height distribution of low-multiplicity Au+Au collisions [27]. Furthermore, the average cell charge per event was found to slowly decrease by 10%–15% over the 10 week duration of the run for some of the modules. This is attributed to a slow deterioration of the quantum efficiency of the photocathodes. This effect was noticed in $\sim 40\%$ of the modules, the others did not show any sign of aging although all photocathodes were produced under identical procedures. An additional time dependent correction factor is applied to account for this effect.

In high multiplicity Au+Au collisions, a large amount of scintillation light is produced by charged particles traversing the CF_4 gas, resulting in a large detector occupancy. The number of photoelectrons per cell can be as high as ~ 10 in the most central collisions. This underlying event background is subtracted on an event-by-event basis. For each event and for each module the average charge per unit area $\langle Q \rangle$ is calculated as:

$$\langle Q \rangle = \sum Q_{cell} / \sum a_{cell}, \quad (1)$$

where Q_{cell} and a_{cell} are the cell charge and area, respectively. The summation is carried out over all the cells of a given module, excluding the cells that are matched to an electron track and their first neighbors. The cell charge used for further analysis Q_{cell}^* , is then given by:

$$Q_{cell}^* = Q_{cell} - \langle Q \rangle \times a_{cell} \quad (2)$$

After subtraction of the underlying event charge, two independent algorithms are used for the HBD hit recognition. The first is a stand-alone algorithm in which a cluster is formed by a seed cell with $Q_{cell}^* > 3$ p.e. together with the fired cells (defined as $Q_{cell}^* > 1$ p.e.) among its first six neighbors. Such clusters can have up to seven cells. A central arm electron track projected onto the HBD readout plane is then matched to the closest cluster. This algorithm works very well in $p+p$ or peripheral Au+Au collisions producing a typical single electron response with an average of 20 p.e.. In higher multiplicity events, this algorithm yields a higher charge per electron and a higher fraction of fake hits as it picks up more charge from the fluctuations of the underlying event background. Figure 5(a) shows an example of a seed cell and three of its first neighbors forming a four cell cluster.

The second algorithm uses the track projection point onto the HBD to form a cluster around it. The pointing resolution of a track to HBD is ~ 3 mm at $p_T \sim 0.5$ GeV/c which is much smaller than the size of a pad. The algorithm allows only up to three cells in a cluster, depending on the track projection position within the cell. If the track projection points to the middle part of the cell, only that cell is used, but if it points to the edge of a cell one or two additional neighboring cells are summed up in the cluster [39]. The same pattern of fired cells shown in Fig. 5(a) would result in a three cell cluster in the projection-based algorithm as illustrated in Fig. 5(b). The projection-based algorithm results in a more precise selection of the true hit, less fake hits and less pick up of charge from underlying event fluctuations.

This is especially important in the most central collisions. On the other hand, the limited cluster size truncates the charge information, resulting in a somewhat reduced efficiency and less power to discriminate between single and double hits. Therefore both algorithms are utilized in a complementary way, the stand alone providing a higher efficiency and better single to double hit separation and the projection-based providing a better rejection of fake hits.

E. Acceptance

1. Acceptance during 2010 run

As mentioned in Section II B, the PHENIX central arm magnets were operated in the $+-$ configuration during the 2010 run. Compared to the standard $++$ magnetic field configuration of PHENIX, the $+-$ configuration has an increased acceptance for low p_T tracks of about 20%.

Charged particles are bent in the azimuthal direction, ϕ , by the magnetic field. Because the DC and RICH are needed to reconstruct the tracks and select the electron candidates, the azimuthal electron acceptance depends on their charge and p_T and on the radial location of each detector subsystem. We define the ideal track acceptance of the PHENIX detector in the $+-$ field configuration by the following set of conditions:

$$\phi_{\min} \leq \phi_0 + q \frac{k_{\text{DC}}}{p_T} \leq \phi_{\max} \quad (3)$$

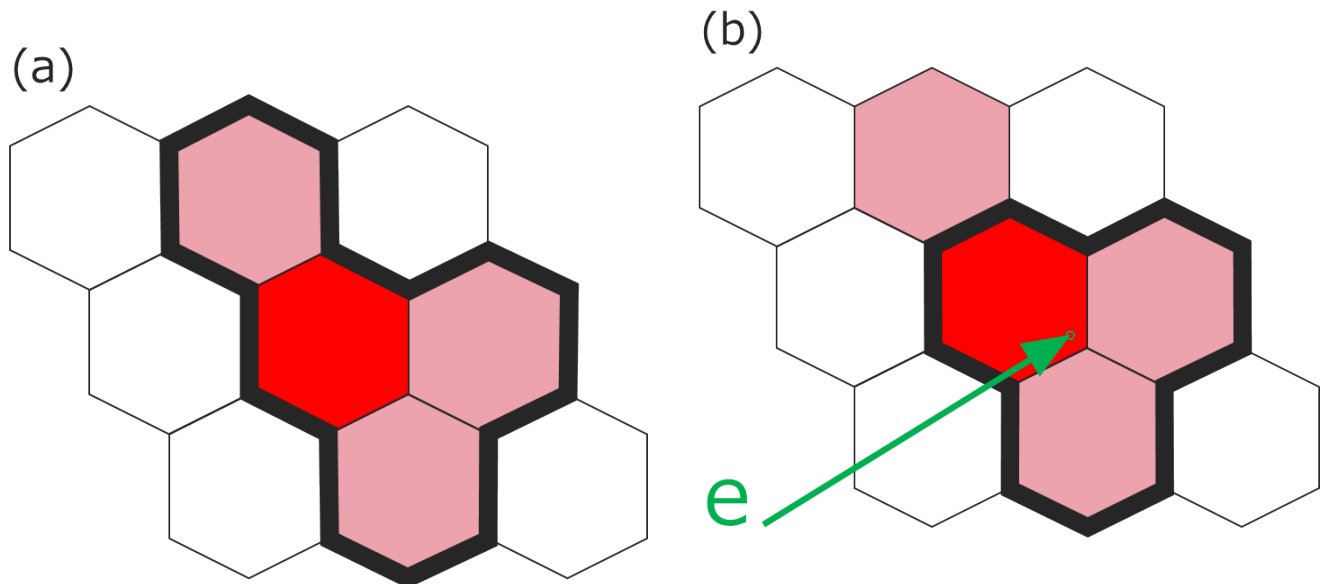


FIG. 5. (Color online) (a) Stand-alone cluster formed by a seed cell (red) and three of its first neighbors resulting in a four cell cluster. Fired cells are colored. (b) The same pattern results in a three cell cluster with the projection-based algorithm that uses the projection point of an electron track onto the pad plane.

$$\phi_{\min} \leq \phi_0 + q \frac{k_{\text{RICH}}}{p_T} \leq \phi_{\max} \quad (4)$$

$$\theta_{\min} \leq \theta_0 \leq \theta_{\max} \quad (5)$$

for tracks originating at $z=0$ with charge q , transverse momentum p_T and emission angles ϕ_0 and θ_0 . $k_{\text{DC}} = 0.060 \text{ rad} \times \text{GeV}/c$ and $k_{\text{RICH}} = 0.118 \text{ rad} \times \text{GeV}/c$ are the effective azimuthal bends to the DC and the RICH, respectively. The polar angle boundaries of $\theta_{\min}=1.23 \text{ rad}$ and $\theta_{\max}=1.92 \text{ rad}$ are defined by the PHENIX central-arms pseudorapidity acceptance $|\eta| < 0.35$. One of the arms covers the azimuthal range from $\phi_{\min} = -\frac{3}{16}\pi$ to $\phi_{\max} = \frac{5}{16}\pi$ and the other from $\phi_{\min} = \frac{11}{16}\pi$ to $\phi_{\max} = \frac{19}{16}\pi$. The results shown in Section V, indicated as “in the PHENIX acceptance”, refer to the results filtered according to this parametrization of the ideal acceptance.

366

2. Fiducial cuts

Several fiducial cuts are applied to remove inactive areas of subsystems or areas with intermittent response, in order to homogenize the detector response over sizable fractions of the run time. Regarding the operation of the drift chamber, the entire 200 GeV Au+Au data set is divided into five groups, with fiducial cuts applied to each group separately such that inside each group the drift chamber has a stable active area. The nonactive DC areas correspond to 19%–31% of the total DC acceptance, depending on the run group.

Fiducial cuts are also applied to the HBD to exclude tracks pointing to one inactive module out of the 20 modules of the HBD. Another fiducial cut removes conversion electrons originating from the HBD support structure, which are strongly localized in ϕ near the edges of the acceptance. Other fiducial cuts are applied to remove inactive or low efficiency areas in PC1 and ECal.

In summary, the ideal PHENIX acceptance is reduced by the fiducial cuts by an amount that varies between 32% and 42%, depending on the run group, with an average of 36% for all selected runs.

378

III. ANALYSIS

This section describes the basic steps of the Au+Au data analysis. It is organized as follows. The data set and event selection cuts are presented in subsection III A. Subsection III B describes the track reconstruction. The methods applied to identify electrons are presented in detail in subsection III C and the cuts applied to electron pairs are explained in subsection III D. A detailed account of the various background sources and their subtraction is provided

383 in subsection III E. Next we present the raw spectra and corrections (subsection III F) and discuss the systematic
 384 uncertainties (subsection III G). In the final subsection III H we discuss a second independent analyses used as a cross
 385 check of the main analysis.

386

A. Data set and event selection

387 The Au+Au collision data at $\sqrt{s_{NN}} = 200$ GeV were collected during 2010. Collisions were triggered using the
 388 beam-beam counters, with the MB trigger condition (see subsection II A).

389 The centrality is determined for each Au+Au collision from the sum of the measured charge in both BBCs combined
 390 with a Glauber model of the collision [40] as described in Ref. [41]. In this analysis, the data sample is divided into
 391 five centrality classes: 0%–10%, 10%–20%, 20%–40%, 40%–60% and 60%–92%. The average number of participants
 392 $\langle N_{\text{part}} \rangle$ and collisions $\langle N_{\text{coll}} \rangle$ together with their systematic uncertainties associated with each centrality bin are
 393 summarized in Table II.

TABLE II. Average values of the number of participants $\langle N_{\text{part}} \rangle$ and number of collisions $\langle N_{\text{coll}} \rangle$ for Au+Au collisions at
 $\sqrt{s_{NN}} = 200$ GeV with the corresponding uncertainties. The values are derived from a Glauber calculation [40, 41].

Centrality	$\langle N_{\text{part}} \rangle$ (syst)	$\langle N_{\text{coll}} \rangle$ (syst)
0%–10%	324.0 (5.7)	951.1 (98.6)
10%–20%	231.0 (7.3)	590.1 (61.1)
20%–40%	135.6 (7.0)	282.4 (28.4)
40%–60%	56.0 (5.3)	82.6 (9.3)
60%–92%	12.5 (2.6)	12.1 (3.1)
0%–92%	106.3 (5.0)	251.1 (26.7)

394 The data were recorded with an online vertex selection of either ± 20 cm (narrow vertex) or ± 30 cm (wide vertex).
 395 The former selection was applied to the data recorded at the beginning of each store, when the luminosity was relatively
 396 high. For the latter selection, an additional-offline vertex cut of $30 < z < 25$ cm was applied. This asymmetric cut is
 397 needed to avoid the increased yield of conversion electrons originating from the side panels of the HBD. These cuts
 398 resulted in 1.8×10^9 events with the narrow-vertex selection, 3.8×10^9 events with the wide-vertex selection, and a
 399 total of 5.6×10^9 MB events.

400

B. Track reconstruction

401 Charged particle tracks are reconstructed in the central arms using the DC and PC1 [32]. The procedure assumes
 402 that all tracks originate from the collision vertex. Each reconstructed track is then projected onto the other detectors,
 403 RICH, EMCal, TOF and HBD, and the projection points are associated to reconstructed hits in these detectors.

404 After a track is reconstructed, the initial momentum vector of the track at the z vertex is calculated. The transverse
 405 momentum p_T is determined by measuring the angle α between the reconstructed particle trajectory and a line that
 406 connects the z -vertex point to the particle trajectory at a reference radius $R = 220$ cm. The angle α is approximately
 407 proportional to charge/ p_T . In the reverse field configuration used in the 2010 run, the momentum resolution is found
 408 to be 1.6% at $p_T = 0.5$ GeV/ c .

409

C. Electron identification

410

1. Detectors and variables used for electron identification

411 For electron identification, the present analysis uses the HBD along with the central arm detectors RICH and
 412 EMCal and the time-of-flight information from the TOF-E detector and the EMCal. The relevant variables for
 413 electron identification from these detectors are:

414

n0: number of hit PMTs in the RICH in the expected range of a Čerenkov ring.

415

disp: distance between a track projection and its associated ring center in the RICH.

416 **chi2/npe0**: a χ^2 -like shape variable of the RICH ring associated with the track per *npe0*, the number of
 417 photoelectrons measured in the ring.

418 **emcsdr**: distance between the track projection point onto the EMCal and the associated EMCal cluster,
 419 measured in units of standard deviation of the momentum dependent matching distribution.

420 **prob**: probability that the EMCal cluster is of electromagnetic origin, based on the shower shape.

421 **dep**: variable quantifying the energy-momentum matching for electrons. It is defined as $dep = \frac{E/p-1}{\sigma_{E/p}}$, where *E*
 422 is the energy measured by the EMCal, *p* is the track momentum and $\sigma_{E/p}$ is the momentum-dependent standard
 423 deviation of the Gaussian-like *E/p* distribution.

424 **stof(PbSc) and stof(TOF-E)**: time-of-flight deviation from the one expected for electrons measured by either
 425 the EMCal-PbSc or the TOF-E detector, converted in units of standard deviation of the Gaussian-like time-of-
 426 flight distribution.

427 **hbdcharge(P), hbdsz(P)**: cluster charge and size from the HBD projection-based algorithm.

428 **hbdid**: reduced cluster charge threshold from the projection-based algorithm. This is the threshold of the
 429 hbdcharge(P) variable, that has been tuned to reduce the number of the nongenuine HBD hits by a fixed factor.
 430 E.g. by requiring hbdid \geq 10, the number of the nongenuine HBD hits is reduced to 1/10 of the initial number.
 431 These thresholds are tuned depending on event multiplicity and HBD cluster size.

432 **maxpadcharge(S)**: charge of the single pad with largest charge in the cluster of the stand-alone algorithm.

433 **hbdcharge(S), hbdsz(S)**: cluster charge and size from the stand-alone algorithm.

434 First, electron candidates are selected from the total sample of tracks that contains mostly hadrons. This is
 435 accomplished by applying very loose cuts such as *n0* > 0, which requires at least one fired PMT around the track
 436 projection in the RICH and *E/p* > 0.4 which rejects the tracks that strongly deviate from the expected *E/p* of \sim 1.
 437 The sample of electron candidates selected in such a way comprises the signal electrons, background electrons (mostly
 438 conversions from the HBD back plane), and a relatively large number of misidentified hadrons.

439 2. Exclusion of RICH photo-multipliers

440 The RICH detector in PHENIX uses spherical mirrors to project the Čerenkov light created by electrons in the
 441 radiator gas onto the PMT plane. As a consequence of this mirror geometry, parallel tracks after the field are projected
 442 to the same point in the PMT plane. In other words, if a hadron track is parallel to an electron track that produces
 443 a genuine response in the RICH, the hadron will appear to have the same response as the electron and thus it will
 444 be misidentified as an electron. Figure 6 shows a typical example of this ring sharing effect. In this example, an
 445 electron-positron pair is generated by a photon conversion in the HBD backplane. After the magnetic field, a hadron
 446 track is parallel to the positron track. Consequently, the hadron and the positron share the same photomultipliers in
 447 the RICH detector and the hadron is misidentified as an electron.

448 This ring sharing effect occurs because the RICH reconstruction algorithm allows multiple use of fired PMTs by
 449 different tracks. The ring sharing is a significant effect. In the 2010 run, the majority of electrons are generated
 450 by γ conversion in the HBD backplane. Although these conversions can successfully be rejected by the HBD, their
 451 response in the RICH remains and there is some probability that the misidentified hadron will also remain in the pool
 452 of electron candidates.

453 To reduce PMT sharing by different tracks in the RICH, the original RICH algorithm is modified. The PMTs fired
 454 by electrons that are clearly identified as background electrons, are removed, the ring reconstruction algorithm is re-
 455 applied and new *n0*, *npe0*, *disp*, χ^2 variables are derived. These background electrons are mainly conversion electrons
 456 from the HBD backplane, electron tracks pointing outside the HBD acceptance, electrons produced by conversion on
 457 the HBD support structure or low *p_T* electrons with *p_T* < 200 MeV/*c*.

458 3. The neural networks

459 After the initial rejection of nonsignal electrons and the reduction of the ring sharing effect, the sample of electron
 460 candidates is still highly contaminated by background electrons and misidentified hadrons. A standard procedure
 461 to increase the purity of the electron sample would be to apply a sequence of one-dimensional cuts on all or some
 462 of the fourteen variables listed above. However, such a procedure results in a large efficiency loss that becomes
 463 significant in the e^+e^- pair analysis where the pair efficiency is approximately equal to the single track efficiency

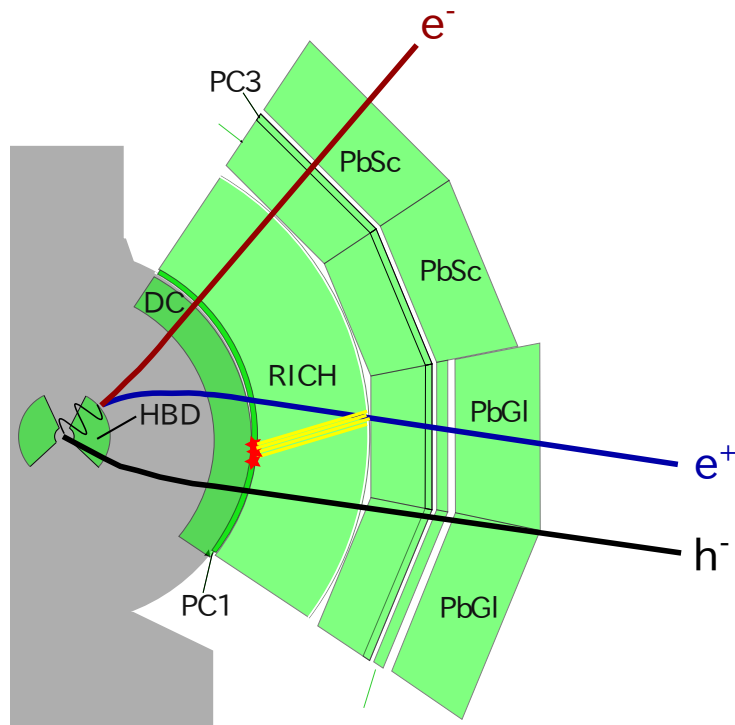


FIG. 6. (Color online) Illustration of a case leading to ring sharing in the RICH detector. The hadron track parallel to the positron track after the magnetic field will be misidentified as an electron.

squared. In this analysis we implement instead a multivariate approach that is based on the neural network package TMultilayerPerceptron from ROOT [42].

The neural network comprises three layers: the input layer, the hidden layer and the output layer. The input layer is composed of all the input variables normalized to have their values between 0 and 1. The hidden layer comprises a selected number of neurons and the output layer comprises a single output variable. The number of neurons in the hidden layer determines the ability of the neural network to distinguish between the signal and the background, but this ability saturates with increasing number of neurons. For each neural network, we make sure that the number of neurons is sufficiently large to provide the best possible performance, typically 10–15 neurons. In addition, we make sure that a sufficient number of tracks is selected for the training sample, such that the performance of the neural network does not depend on the training statistics. The neural network output is a single probability-like variable, in which values closer to 1 mostly correspond to signal, while values closer to 0 mostly correspond to background (examples of the neural network output distributions will be shown below). By selecting the tracks above a certain threshold, we can reject most of the background while keeping a large fraction of the signal.

We use three different neural networks specially trained on subsets of the large list of eID variables to reject (i) hadrons misidentified as electrons in the central arms (NN_h), (ii) background electrons which are mostly HBD backplane conversions (NN_e) and (iii) double hits in the HBD (NN_d). In this way we basically have three handles to separately treat each type of background. The neural networks learn to distinguish the signal and the background on well defined samples. The first two neural networks, NN_h and NN_e , are trained on HIJING events. The third neural network NN_d is trained on a sample of single particle event simulations, $\phi \rightarrow e^+e^-$ decays for single response and $\pi^0 \rightarrow \gamma e^+e^-$ Dalitz decays for double response. The training is done separately for each centrality bin in order to properly treat the multiplicity effects. For centralities $> 40\%$, we use the neural network trained for the 20%–40% centrality bin, where the statistics of the training sample is higher. This is justified because already in the 20%–40% centrality bin, multiplicity effects are unimportant and the separation between signal and background is good. The training is also done separately for the three cases of time-of-flight information (TOF-E, PbSc-TOF, no time-of-flight information).

The simulated events are passed through a GEANT simulation of the PHENIX detector and through the same reconstruction code that is used for the data analysis. They are divided into two samples. One is used for training purposes and the other one to monitor the neural network output. The simulated events are not used to determine

492 absolute efficiencies (those are determined from simulation as discussed later in Section III F. They are used only for
 493 training and monitoring purposes and the HIJING events are particularly valuable in this respect. They allow us to
 494 assess the origin and relative magnitude of the various background sources at each step of the electron identification
 495 chain, as well as the neural network performance in its ability to reject the background while preserving the signal.
 496 Details of the three neural networks are given below.

497

4. Hadron rejection

498 The first neural network, NN_h , aims at reducing the hadron contamination. It exploits the information from all
 499 the relevant detectors, HBD, RICH, EMCal and TOF-E. The signal (S) for the training of NN_h comprises electron
 500 tracks originating at the collision vertex, whereas the background (B) comprises all the remaining misidentified hadron
 501 tracks in the sample.

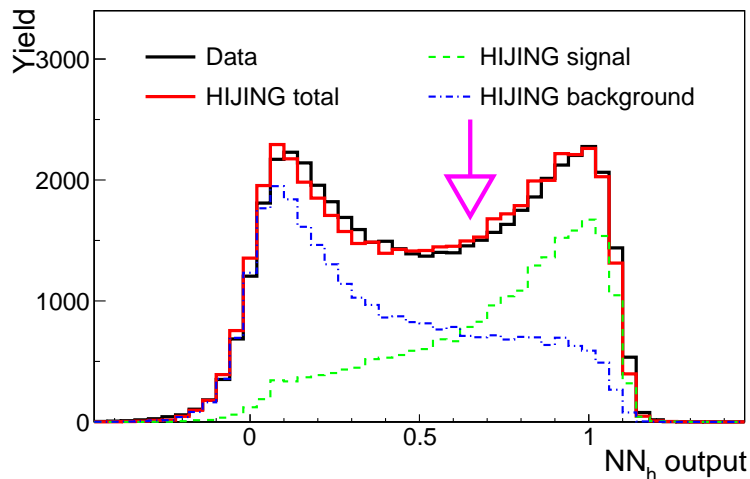


FIG. 7. (Color online) Comparison of the output values of the neural network NN_h for the 0%–10% centrality bin applied to the HIJING monitoring sample (red line) and to real data (black line). The figure also shows the signal (green) and the background (blue) components of the HIJING simulation. The arrow represents the average final cut selected by the cut optimization procedure. See text in Section III C 7.

502 Figure 7 shows the output values of NN_h for the HIJING monitoring sample (red line) and also shows the output of
 503 NN_h applied on real data (black line). The truth information from the HIJING events in terms of signal and background
 504 is shown separately. It should be noted that in the HIJING monitoring sample, all electron tracks are considered. The
 505 signal comprises the genuine electrons excluding the HBD backplane conversions and the background is all remaining
 506 tracks.

507

5. Background electron rejection

508 After rejecting hadrons in the previous step, the dominant background in the electron sample comes from the
 509 conversions in the HBD backplane that were not rejected by the conservative process described in III C 2. Because
 510 these conversions do not leave a signal in the HBD they can be recognized and rejected if the tracks do not have a
 511 matching HBD response. The rejection capability is however limited by fluctuations remaining after the underlying
 512 event subtraction in the HBD. To provide the optimal rejection of the remaining backplane conversions we use a neural
 513 network, NN_e , which is based on the HBD information reconstructed by both the stand-alone and the projection-based
 514 algorithms. The signal tracks for the training of NN_e comprise all signal electrons remaining after the previous step,
 515 while the background sample includes only the electrons originating from the HBD backplane.

516 Figure 8 shows the distribution of output values of NN_e applied to the HIJING monitoring sample (red line) and to
 517 data (black line). The signal and background components of the HIJING simulation are shown separately.

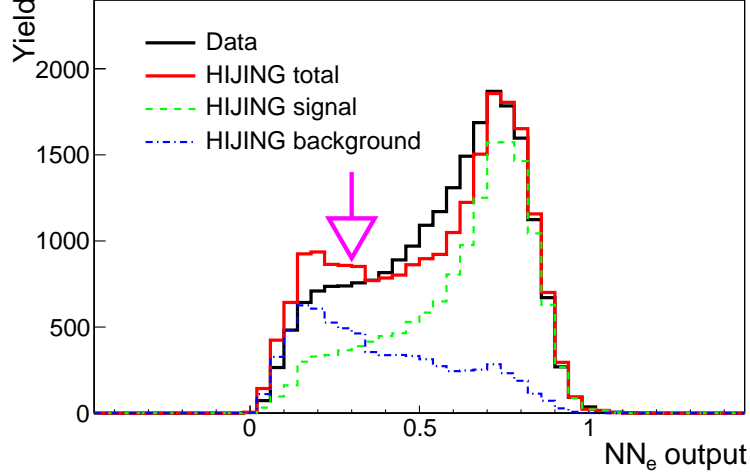


FIG. 8. (Color online) Comparison of the output values of the neural network NN_e for the 0%–10% centrality bin applied to the HIJING monitoring sample (red line) and to real data (black line). The figure also shows the signal (green) and the background (blue) components of the HIJING simulation. The arrow represents the average final cut selected by the cut optimization procedure. See text in Section III C 7.

518

6. Double-hit rejection in the HBD

519 After removing hadrons and backplane conversions as much as possible, the major sources of background are the
 520 beam-pipe and radiator conversions and electrons from π^0 Dalitz decays where only one track is reconstructed in the
 521 central arms. These electrons have a zero or very small opening angle and most of them lead to a double hit in the
 522 HBD. Double hits can be recognized using the HBD response reconstructed in parallel by both the stand-alone and
 523 the projection-based algorithms. The response is coupled in a neural network, NN_d separately optimized for different
 524 HBD cluster sizes as well as centrality classes. The NN_d cut is an implicit small opening angle cut given by the
 525 maximum cluster size which is of the order of 75 mrad.

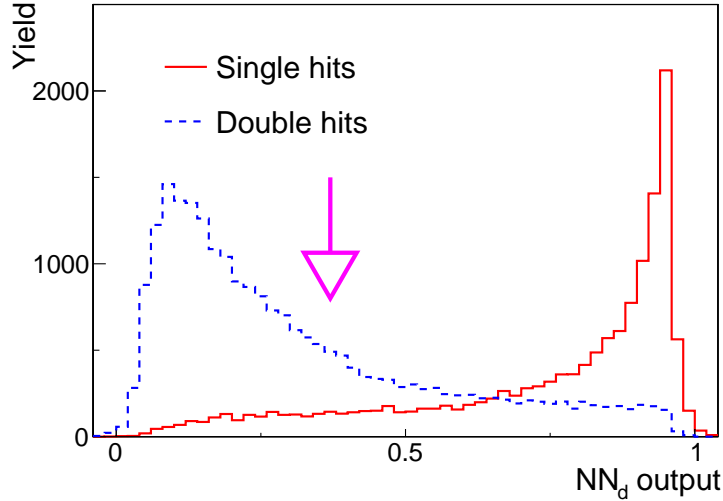


FIG. 9. (Color online) The output of the neural network NN_d for the recognition of single and double hits in the HBD. Single response (solid line) is provided by electrons from simulated $\phi \rightarrow e^+e^-$ decays and double response (dashed line) by electrons from $\pi^0 \rightarrow \gamma e^+e^-$ Dalitz decays. This example is for 30%–40% centrality and for a three cell cluster size. The arrow represents the average final cut selected by the cut optimization procedure. See text in Section III C 7.

526 Figure 9 shows the distribution of the output variable of the neural network NN_d for the separation of single and
 527 double hits in the HBD. The single response is provided by electrons from simulated $\phi \rightarrow e^+e^-$ decays and the double
 528 response by electrons from $\pi^0 \rightarrow \gamma e^+e^-$ Dalitz decays. The simulations are embedded into real HBD background
 529 events in order to take into account centrality dependent occupancy effects.

530

7. Cut optimization

531 The final selection of cuts on each neural network output variable is optimized using HIJING events. The thresholds
 532 are varied separately to maximize the effective signal, S/\sqrt{B} . Because the statistics of the HIJING samples are by far
 533 insufficient for a pair analysis, for the signal S we use the number of single electrons from charm decay per event,
 534 which is an easily identified signal in HIJING, and for the background B we use the total number of electrons per
 535 event. The cut optimization is done separately for each centrality class, for two p_T ranges ($p_T < 300$ MeV/ c and p_T
 536 > 300 MeV/ c), for each cluster size, and for each TOF configuration. The effective signal for each setup is maximized
 537 subject to the following conditions:

- 538 • The three types of TOF configuration (with PbSc timing information, with TOF-east timing information and
 539 without any timing information), have similar efficiencies with differences of less than 15%.
- 540 • Hadron contamination less than 5% for TOF-E and PbSc-TOF and less than 10% for the no-TOF case.

541 The arrows in Figs. 7-9 represent the average final cuts selected by the cut optimization procedure for these
 542 particular cases. The final cuts produce an electron sample with small hadron contamination, of less than 5%, for
 543 all centralities. Strong cuts on the HBD are needed to achieve this small hadron contamination, resulting in a single
 544 electron efficiency of 25%–40% depending on centrality, at $p_T > 0.5$ GeV/ c (See Section III F).

545

D. Pair cuts

546 The track selection criteria described above provide an electron sample with high purity. However, besides these
 547 criteria which are applied on a track-by-track basis, this analysis implements a series of dielectron cuts, based on the
 548 pair properties. These cuts are needed in order to remove ghost pairs i.e. pairs correlated by the close proximity of
 549 tracks in one of the detectors. Such correlations cannot be described by the mixed background, by definition, therefore
 550 this part of the phase-space must be removed from both the foreground and the mixed background. In the present
 551 analysis we remove the whole event, if such a pair is found, as was done in Ref. [23]. This procedure removes only
 552 $\sim 2\%$ more of the total pair yield than discarding the pairs, because the average pair multiplicity is relatively low.

553 The most prominent detector correlation comes from the ring sharing effect in the RICH detector, discussed in
 554 Section III C 2, which arises when two tracks are parallel after the magnetic field, with at least one of them being an
 555 electron.

556 As mentioned above, the detector-correlated pairs are identified by applying a cut on the physical proximity of the
 557 tracks forming a pair in every detector and the cut value is determined by the corresponding double hit resolution. In
 558 the RICH detector, the cut selects pairs whose rings are closer than 36 cm, which is twice the diameter of the RICH
 559 ring (~ 16.8 cm). In the EMCal, the cut removes a region of 2.5×2.5 towers around the hit. In PC1 the pairs are
 560 selected for removal if their tracks are within 5 cm in z or 0.02 rad in ϕ .

561 The effect of these three pair cuts on the like-sign and unlike-sign mass spectra is shown in Fig. 10. The like-sign
 562 yield close to $m_{ee} \sim 0$ GeV/ c^2 is affected by all cuts. On the other hand, in the unlike-sign foreground spectrum, the
 563 cuts affect well localized regions producing two clearly visible dips. The dip at $m_{ee} \sim 0.25$ GeV/ c^2 is created by the
 564 RICH pair cut and the dip at $m_{ee} \sim 0.15$ GeV/ c^2 is created by the PC1 pair cut. The EMCal pair cut removes yield
 565 around 0.20 GeV/ c^2 , but the effect is small compared to the other two cuts.

566 In addition to the RICH, EMCal and DC/PC1 ghost cuts, a 100 mrad opening angle cut is applied to remove
 567 ghost pairs in the HBD. This is a proximity cut that translates to a distance of two cells in the pad readout and
 568 roughly corresponds to the double hit separation of the HBD. This cut affects the yield at $m_{ee} \sim 0$ GeV/ c^2 in both
 569 the like-sign and unlike-sign mass spectra.

570

E. Background Pair Subtraction

571 Because the origin of the electron track candidates is not known, all electrons and positrons in the same event are
 572 paired to form the unlike-sign (FG_{+-}) and like-sign (FG_{++} and FG_{--}) foreground mass spectra. This gives rise to

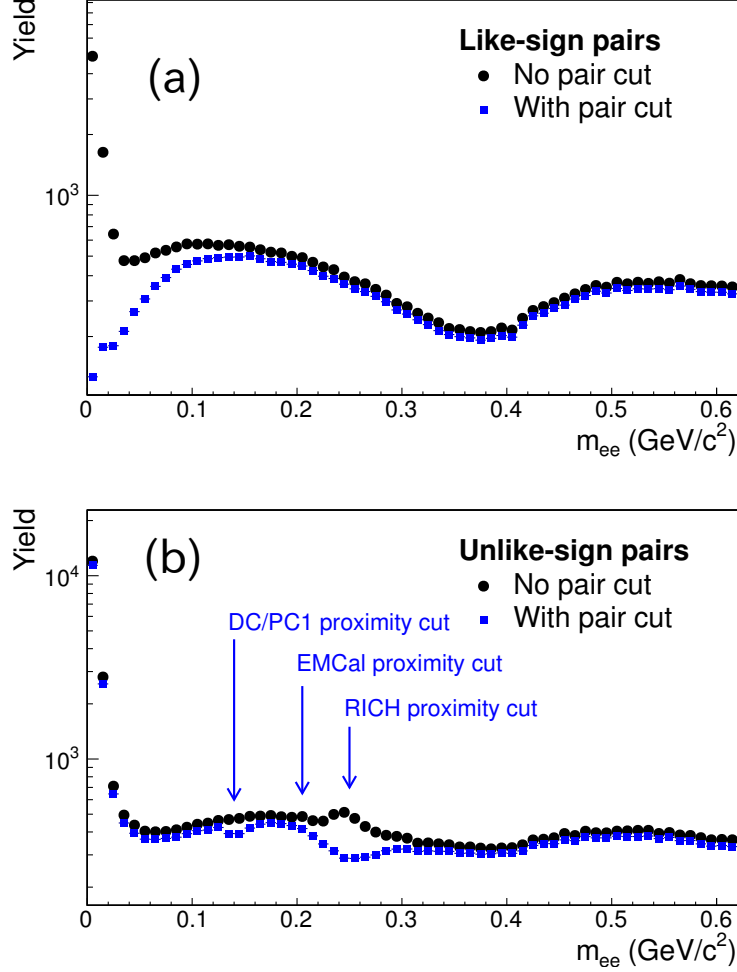


FIG. 10. (Color online) (a) Like-sign and (b) unlike-sign foreground spectra without any pair cuts (Black) and with RICH, EMCal and PC1 pair proximity cuts (Blue) for MB events.

573 a large combinatorial background that increases quadratically with the event multiplicity. In addition to that, there
 574 are several background sources of correlated pairs. The evaluation and subtraction of the background is the crucial
 575 step in the analysis of dileptons in particular in situations, like the present one, where the S/B is at the sub-percent
 576 level. In this section, we describe in detail the various sources contributing to the background and the methodology
 577 used to evaluate each of them.

578

1. Background sources

579 The unlike-sign foreground spectrum FG_{+-} contains, in addition to the physical signal (S), a large background
 580 comprising the following sources:

- 581 • Uncorrelated combinatorial background (CB): It arises from the random combinations of electrons and positrons
 582 originating from different parent particles and is an inherent consequence of pairing all electrons with all positrons
 583 in the same event. The combinatorial background accounts for most of the total background, more than 99% in
 584 the most central collisions and more than 90% in peripheral collisions. The two electron tracks of combinatorial
 585 pairs are uncorrelated. However, they carry a global modulation induced by the collective flow of each individual
 586 collision. The evaluation of the combinatorial background together with the flow modulation is described in
 587 detail in the following subsection. (See Section III E 2.)
- 588 • Correlated background pairs. There are three different sources of correlated background pairs:

- 589 – Cross pairs (*CP*): A cross pair can be produced when there are two e^+e^- pairs in the final state of a single
590 meson decay. One such case is $\pi^0 \rightarrow e^+e^-\gamma \rightarrow e^+e^-e^+e^-$. The pair formed by an electron directly from
591 π^0 and a positron from γ conversion does not come from the same parent particle but it is a correlated
592 pair through the same primary particle. (See Section III E 3.)
- 593 – Jet pairs (*JP*): The jet pairs are produced by two electrons generated in the same jet or in back-to-back
594 jets. (See Section III E 4.)
- 595 – Electron-hadron pairs (*EH*): Whereas the previous two sources of correlated pairs are of physics origin,
596 the electron-hadron pairs are an artifact that results from residual detector correlations that cannot be
597 handled by the pair cuts. (See Section III E 5.)

598 One can then write:

$$FG_{+-} = S + CB_{+-} + CP_{+-} + JP_{+-} + EH_{+-} \quad (6)$$

599 All the background sources listed above form the yield of the like-sign foreground mass spectra FG_{++} and FG_{--} .
600 There is no signal in these spectra with the exception of a very small contribution of e^+e^+ and e^-e^- pairs from $b\bar{b}$
601 decays (*BB*). So one can write:

$$FG_{++} = CB_{++} + CP_{++} + JP_{++} + EH_{++} + BB_{++} \quad (7)$$

602

$$FG_{--} = CB_{--} + CP_{--} + JP_{--} + EH_{--} + BB_{--} \quad (8)$$

603 Usually the like-sign pairs are subtracted from the unlike-sign pairs to obtain the signal. This is a convenient
604 approach in a detector with 2π azimuthal coverage, which ensures that the uncorrelated background is charge sym-
605 metric, under the assumption that the correlated background is also charge symmetric, i.e. it produces the same yield
606 and mass distribution of like and unlike pairs. These conditions are not met in the present situation. The two central
607 arm configuration of the PHENIX detector results in a substantial acceptance difference between like and unlike-sign
608 pairs. Furthermore, the like-sign pairs contain a small signal component from $b\bar{b}$ decays that needs to be calculated
609 separately. Finally, as shown below, the electron-hadron pairs are not charge symmetric. For these reasons, in this
610 analysis we adopt a different approach in which each source is evaluated separately for a quantitative understanding
611 of the like-sign yield. Once this is demonstrated, the background sources, *CB*, *CP*, *JP* and *EH* are subtracted from
612 the inclusive foreground unlike-sign spectrum in order to obtain the mass spectrum of the signal pairs. The following
613 subsections outline the evaluation of the various background sources.

614 The *BB* contribution which is part of the signal is needed only for the quantitative evaluation of the like-sign
615 spectra. The contribution is calculated using MC@NLO (See Section IV for details), which generates both like-sign
616 and unlike-sign contributions from $B\bar{B}$. The small like-sign contribution from $D\bar{D}$ is neglected.

617

2. Combinatorial background (*CB*)

618 The combinatorial background is determined using the event mixing technique, in which tracks from different events
619 but with similar characteristics are combined into pairs. In this analysis, all events are classified into 11 bins in z
620 vertex between -30 cm and $+25$ cm, and 10 bins in centrality between 0% and 92%.

621 In principle, the event mixing technique is expected to reproduce the shape of the combinatorial background with
622 great statistical accuracy, because one can mix as many events as needed to reduce the statistical uncertainty to
623 a negligible level. In fact it does not reproduce the shape. There is a small difference between the foreground
624 combinatorial background and the mixed event background. The former is affected by the elliptic flow which is
625 intrinsic to heavy ion collisions, whereas the latter is obtained by randomly picking up two tracks from different
626 events and thus on the average does not have any flow effect.

627 To take into account the effect of flow in the mixed-events, one could make reaction plane bins, in addition to the
628 vertex and centrality bins, so that only events with similar reaction plane are mixed. However, the method is limited
629 by the reaction plane resolution and in PHENIX, the latter is not sufficient to reproduce the shape of the foreground
630 combinatorial background. Instead, in the present analysis, a weighting method, based on an analytical calculation
631 of the flow modulation, is used to account for the flow effects in the mixed events.

632 If particles are generated according to the following distribution function:

$$1 + 2v_2 \cos 2(\phi - \psi), \quad (9)$$

633 where ϕ is the particle emission angle in azimuth, ψ is the reaction plane angle and v_2 is the elliptic flow coefficient,
 634 then random pairs formed from these particles are distributed as (See Appendix A for the derivation):

$$P(\phi_a - \phi_b) = 1 + 2v_{2,a}v_{2,b} \cos 2(\phi_a - \phi_b), \quad (10)$$

635 where $\phi_{a(b)}$ is the azimuthal emission angle and $v_{2,a(b)}$ the elliptic flow of the two particles forming the pair.

636 In the weighting method, each mixed background pair is weighted by Eq. (10). The v_2 values of inclusive electrons
 637 are determined from the present data prior to the pair analysis as a function of centrality and electron p_T using the
 638 reaction plane method [43]. Exactly the same cuts as in the data analysis are used in the v_2 calculation. The obtained
 639 v_2 values are in very good agreement with the inclusive electron v_2 values reported in Ref. [44].

640 We use a Monte-Carlo (MC) simulation to evaluate the method. The simulation generates electrons and positrons
 641 following a Poisson distribution with a mean value of three ¹. The particles are uniformly distributed in pseudorapidity
 642 between ± 0.35 and their momentum distribution is taken from data. The azimuthal emission angle ϕ is determined
 643 according to the distribution $1 + 2v_2 \cos 2(\phi - \psi)$, where ψ is the reaction plane angle, which is uniformly distributed
 644 between $\pm \frac{\pi}{2}$. The v_2 values are taken from the 20%–40% centrality bin. The tracks that pass the PHENIX acceptance
 645 filter are used in the pair analysis.

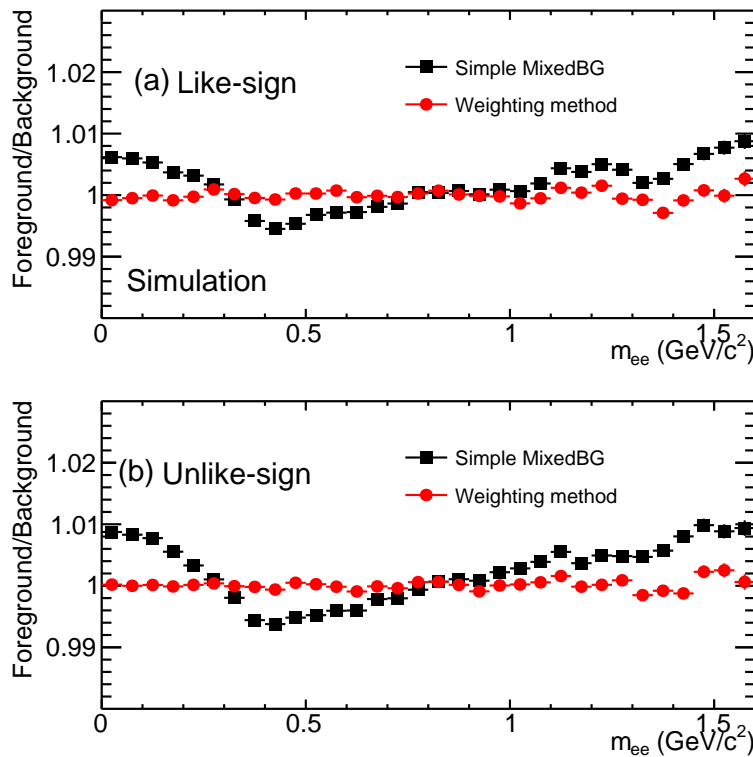


FIG. 11. (Color online) Foreground to mixed background ratio of (a) like-sign and (b) unlike-sign mass spectra ratio in a MC simulation. The foreground is generated with flow, whereas the mixed events are produced without flow i.e. using a simple mixed-event technique (squares) and with flow modulation using the weighting method (circles).

646 Figure 11 shows the ratio of the foreground to mixed background mass spectra. The squares correspond to the
 647 simple mixed-event technique without correcting for flow. We can see that in this approach the ratio is not flat, i.e.
 648 the foreground shape is not reproduced by the mixed background shape. The circles correspond to the weighting
 649 method. The ratio is completely flat over the entire mass range demonstrating that the weighting method properly
 650 accounts for the flow modulation.

651 A similar MC study was performed to evaluate whether triangular flow v_3 also induces shape distortion of the mass
 652 spectrum. For the most central collisions, where v_3 is comparable to v_2 at high p_T [45], the simulations show that the
 653 v_3 effect is at least one order of magnitude smaller than for v_2 and we thus ignore triangular flow in the determination
 654 of the combinatorial background shape.

¹ There is not much meaning to the mean value of 3 of the Poisson distribution. It is a convenient choice to have one pair per event with a high probability.

3. Cross pairs (CP)

Cross pairs can be produced when a hadron decay produces two e^+e^- pairs in the final state. The following hadron decays and subsequent photon conversions lead to cross pairs:

$$\pi^0 \rightarrow e_1^+ e_1^- \gamma \rightarrow e_1^+ e_1^- e_2^+ e_2^- \quad (11)$$

$$\pi^0 \rightarrow \gamma_1 \gamma_2 \rightarrow e_1^+ e_1^- e_2^+ e_2^- \quad (12)$$

$$\eta \rightarrow e_1^+ e_1^- \gamma \rightarrow e_1^+ e_1^- e_2^+ e_2^- \quad (13)$$

$$\eta \rightarrow \gamma_1 \gamma_2 \rightarrow e_1^+ e_1^- e_2^+ e_2^- \quad (14)$$

The cross combinations give rise to two unlike-sign pairs ($e_1^+ e_2^-$ and $e_2^+ e_1^-$) as well as two like-sign pairs ($e_1^+ e_2^+$ and $e_1^- e_2^-$) that are not purely combinatorial, but correlated via the π^0 or η mass and momentum. Therefore, this contribution is not reproduced by the event-mixing technique.

To calculate the cross pairs, we use EXODUS (see Section IV) to generate π^0 and η with the following input parameters:

- Flat-vertex distribution within $|z| < 30$ cm. The final results are weighted to restore the measured vertex distribution.
- Flat pseudorapidity distribution within $|\eta| < 0.6$ and uniform in ϕ within $0 < \phi < 2\pi$.
- Momentum distributions based on PHENIX measurements (see Section IV).

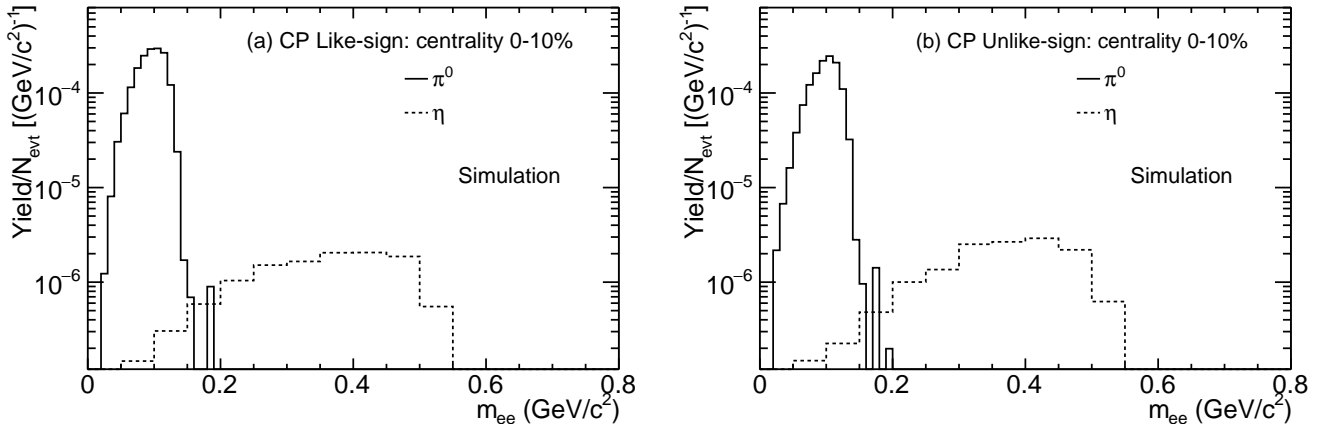


FIG. 12. Absolutely normalized (a) like-sign and (b) unlike-sign spectra of cross pairs (CP) from EXODUS and GEANT simulations for the 0%–10% centrality bin. The π^0 and η contributions are shown separately.

The generated π^0 and η are passed through a GEANT simulation of the PHENIX detector. By selecting reconstructed cross pairs, one can determine the shape of the cross-pair invariant mass spectrum. The spectra are then absolutely normalized using the rapidity density values dN_{π^0}/dy and dN_{η}/dy as a function of centrality, summarized in Section IV. The absolutely normalized mass spectra of cross pairs for the 0%–10% centrality bin are shown in Fig. 12.

4. Jet pairs (JP)

The jet pairs are produced using the PYTHIA 6.319 code with CTEQ5L parton distribution functions [46]. The following hard quantum-chromodynamics (QCD) processes are activated [23]:

- MSUB 11: $f_i f_j \rightarrow f_i f_j$

- 678 • MSUB 12: $f_i \bar{f}_i \rightarrow f_k \bar{f}_k$
- 679 • MSUB 13: $f_i \bar{f}_i \rightarrow gg$
- 680 • MSUB 28: $f_i g \rightarrow f_i g$
- 681 • MSUB 53: $gg \rightarrow f_k \bar{f}_k$
- 682 • MSUB 68: $gg \rightarrow gg$

683 where g denotes a gluon, $f_{i,j,k}$ are fermions with flavor i, j, k and $\bar{f}_{i,j,k}$ are the corresponding antiparticles. A
 684 Gaussian width of 1.5 GeV/ c for the primordial k_T distribution (MSTP(91)=1, PARP(91)=1.5) and 1.0 for the K-
 685 factor (MSTP(33)=1, PARP(31)=1.0) are used. The minimum parton p_T is set to 2 GeV/ c (CKIN(3)=2.0). The z
 686 coordinate of the vertex position is produced uniformly between ± 30 cm and then weighted to reproduce the measured
 687 distribution. From the PYTHIA output, π^0 and η are extracted and passed through the GEANT simulator of PHENIX
 688 in order to generate the inclusive e^+e^- pairs.

689 In addition to the jet pairs we are interested in, the foreground pairs from PYTHIA events contain also “physical”
 690 pairs, cross pairs and combinatorial pairs. The “physical” pairs and cross pairs are excluded from the foreground
 691 pairs by requiring that the two electrons or positrons of the pair do not share the same particle in their history.
 692 The combinatorial background is statistically subtracted using the event-mixing technique. The mixed event like-sign
 693 pairs are normalized to the foreground like-sign pairs in the range $\Delta\phi_0^{prim} \sim \pi/2$, where $\Delta\phi_0^{prim}$ is the difference in
 694 the azimuthal angle of the primary particles, π^0 or η . Figure 13 shows the $\Delta\phi_0^{prim}$ distributions of the foreground
 695 pairs and the normalized mixed-event pairs. The excess yield around $\Delta\phi_0^{prim} \sim 0$ represents the dileptons from the
 696 same jet whereas the excess yield at $\Delta\phi_0^{prim} \sim \pi$ corresponds to the dileptons from opposite or back-to-back jets.

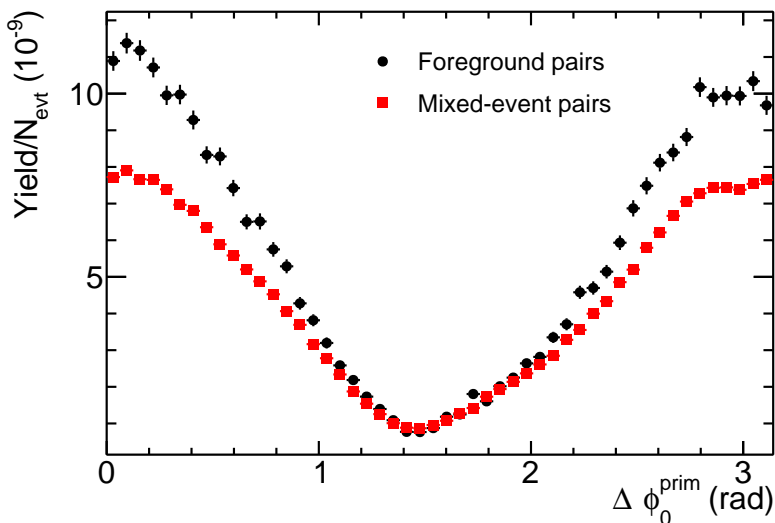


FIG. 13. (Color online) $\Delta\phi_0^{prim}$ (difference in the azimuthal angle of the primary particles, π^0 or η) distributions of foreground and normalized mixed-event background like-sign pairs as obtained from the PYTHIA simulations.

697 After subtracting the combinatorial background, the PYTHIA spectra are scaled to give the pion yield per $p+p$ MB
 698 event. The scaling factor is determined such that the π^0 yield in the PYTHIA simulation matches the measured π^0
 699 yield in $p+p$ collisions [47] and found to be 1/3.9.

700 The spectra need to be further scaled to obtain the jet contribution in Au+Au collisions for each centrality bin.
 701 This scaling is done following Ref. [48]: an ee jet pair originating from primary particles with momenta $p_{T,1}$ and $p_{T,2}$
 702 is scaled by the average number of binary collisions $\langle N_{coll} \rangle$ for each centrality bin, times $R_{AA}(p_{T,1})$, times $I_{AA}(p_{T,2})$.
 703 The same jet or opposite jet $I_{AA}(p_{T,2})$ values are applied depending on the pair opening angle. The absolutely
 704 normalized jet pair spectra for the 0%–10% centrality bin are shown in Fig. 14.

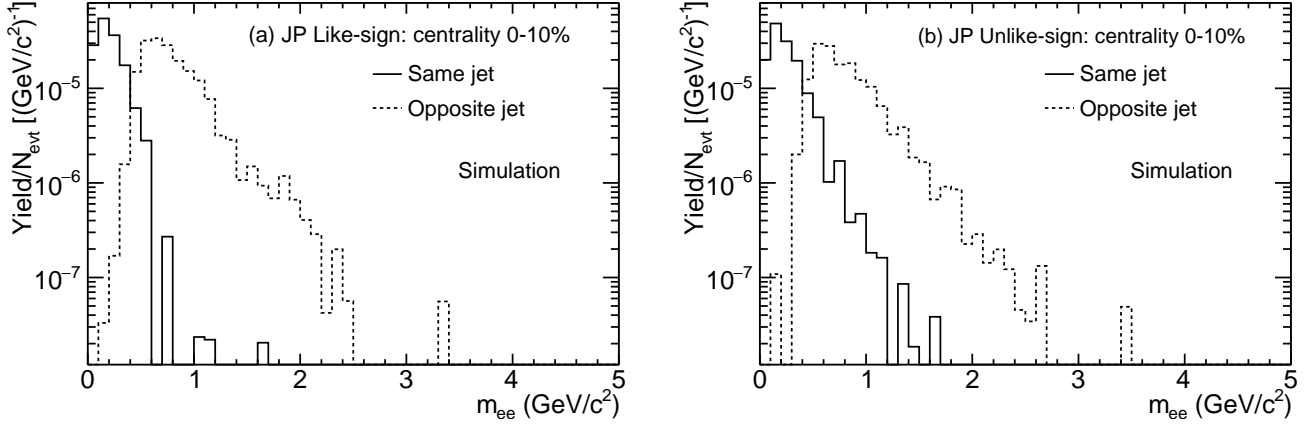


FIG. 14. Absolutely normalized (a) like-sign and (b) unlike-sign spectra of jet pairs (JP) simulated by PYTHIA and GEANT for the 0%–10% centrality bin. The near-side and away-side contributions are shown separately.

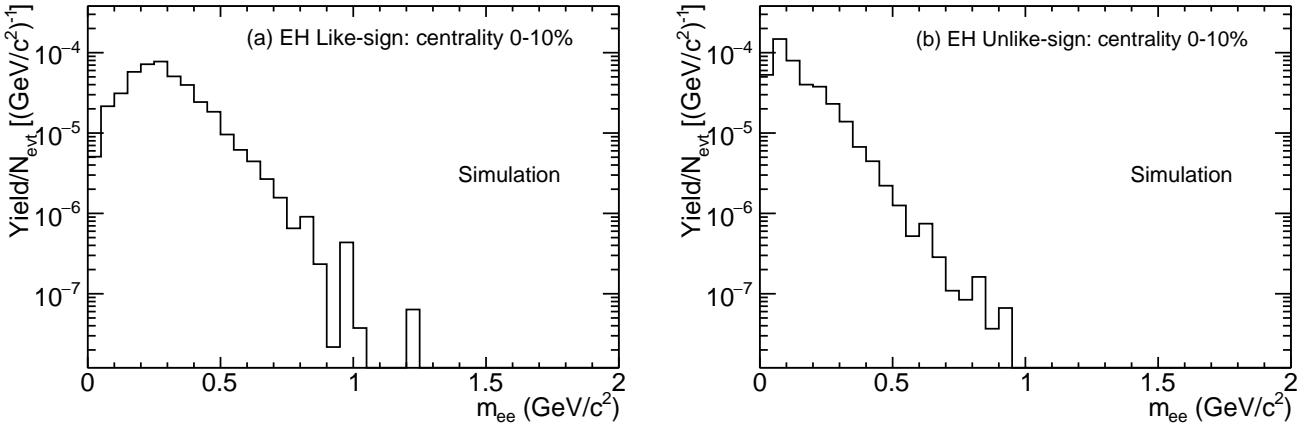


FIG. 15. Absolutely normalized (a) like-sign and (b) unlike-sign spectra of simulated electron-hadron pairs (EH) for the 0%–10% centrality bin. See text for details.

705

5. Electron-hadron pairs (EH)

706 Even after applying the pair cuts described in Section III D, electron-hadron pairs correlated through detector effects
 707 remain in the foreground pairs. An example of such an electron-hadron pair can be illustrated with the sketch of
 708 Figure 6 discussed in Section III C 2. In this example, if both the positron and the mis-identified hadron are detected,
 709 the pair is identified as a RICH ghost pair and the entire event is rejected by the RICH ghost pair cut as described in
 710 Section III D. However, if the positron is not detected due to detector dead areas or reconstruction inefficiency, the
 711 pair formed by the electron and the mis-identified hadron is not rejected and remains in the sample. This pair is not
 712 a combinatorial pair but correlated through the positron. Although the mis-identification of hadrons via hit sharing
 713 occurs in all detectors, the RICH detector is the dominant contributor to these electron-hadron pairs. Therefore, only
 714 the RICH detector is considered as the source of such correlated pairs.

715 We simulate electron-hadron pairs using electrons from π^0 and η simulations and hadrons from real events. The π^0
 716 and η simulations are the same ones that are used for the cross pair simulation. The hadrons from real events are all
 717 the reconstructed tracks that fail the eID cuts.

718 The simulation is performed in the following way: First, a combined event is formed using electrons from one
 719 Dalitz decay of π^0 or η generated with EXODUS and hadrons from a real event. Second, the information from their
 720 associated fired PMTs is merged and new rings are reconstructed. Using the new RICH ring variables, the regular
 721 analysis procedure, including eID cuts and pair cuts, is performed on the combined event. Finally, the pairs formed
 722 by the combination of an electron track from simulation and a hadron track from data are extracted. The spectra are

absolutely normalized using the π^0 dN/dy values shown in Section IV. The absolutely normalized electron-hadron pair spectra for the 0%–10% centrality bin are shown in Fig. 15. Contrary to the cross pairs and the jet pairs where the like- and unlike-sign spectra have a very similar shape, the electron-hadron pairs exhibit a sizable difference between the like- and unlike-sign spectra. The yield of electron-hadron pairs has a strong centrality dependence. It increases by a factor of ~ 50 from peripheral to central collisions with respect to the π^0 rapidity density. This increase is mainly due to the expected scaling of the electron-hadron pairs with the square of the event multiplicity.

729

6. Background normalization

The cross pairs, jet pairs, electron-hadron pairs and $b\bar{b}$ decay pairs are absolutely normalized. The mixed event technique provides only the shape of the combinatorial background. It needs to be normalized in order to be able to subtract the background and extract the signal. The only free parameters of the entire procedure are thus the normalization factors of the mixed event background like-sign spectra nf_{++} and nf_{--} . They are determined by normalizing the mixed event background yield ($N_{MIX_{++(---)}}$) to the foreground yield ($N_{FG_{++(---)}}$), integrated over a selected region of phase space, after subtracting the correlated pairs integrated over the same region:

$$nf_{++} = \frac{N_{FG_{++}} - N_{CP_{++}} - N_{JP_{++}} - N_{EH_{++}} - N_{BB_{++}}}{N_{MIX_{++}}}$$

$$nf_{--} = \frac{N_{FG_{--}} - N_{CP_{--}} - N_{JP_{--}} - N_{EH_{--}} - N_{BB_{--}}}{N_{MIX_{--}}}$$

where $N_{CP_{++(---)}}$, $N_{JP_{++(---)}}$, $N_{EH_{++(---)}}$ and $N_{BB_{++(---)}}$ are the integral yields of each source in the normalization region. The normalization region is a window in the azimuthal angular distance of the two tracks $\Delta\phi_0$. It needs to satisfy two competing conditions. On the one hand, a small normalization window containing only combinatorial pairs is preferred to avoid being affected by any residual yield (and systematic uncertainties) from the correlated background sources. On the other hand, a wide normalization window is required to reduce statistical uncertainty. The normalization windows used in this analysis for each centrality bin are shown in Table III together with the corresponding number of like-sign pairs ($N_{LS} = N_{FG_{++}} + N_{FG_{--}}$). The region of small opening angles that correspond to small masses where the correlated pairs CP , JP and EH mostly contribute, is excluded in all centrality bins.

TABLE III. Normalization window for each centrality bin. The number of like-sign pairs N_{LS} in the window is also shown.

Centrality	Normalization window $\Delta\phi_0$	N_{LS}
0%–10%	0.7 - 3.14	5.1M
10%–20%	0.7 - 2.1	1.1M
20%–40%	0.7 - 2.1	660K
40%–60%	0.9 - 2.1	48K
60%–92%	0.9 - 2.1	3K

The combinatorial background in Eqs. (7) and (8) is thus given by the normalized mixed-event background:

$$CB_{++}(m_{ee}) = nf_{++} \cdot MIX_{++}(m_{ee}) \quad (15)$$

$$CB_{--}(m_{ee}) = nf_{--} \cdot MIX_{--}(m_{ee}) \quad (16)$$

As long as electrons and positrons are produced in pairs and these pairs are uncorrelated, the total unlike-sign combinatorial background yield is the geometric mean of the total like-sign combinatorial yield, independent of single electron efficiency and acceptance [23]:

$$CB_{+-} = 2\sqrt{CB_{++} \cdot CB_{--}} \quad (17)$$

A similar relation holds true for the integral yields of the mixed-event background:

$$MIX_{+-} = 2\sqrt{MIX_{++} \cdot MIX_{--}} \quad (18)$$

749 The normalization factor nf_{+-} of the unlike-sign mixed event background is thus deduced from the normalization
 750 factors of the like-sign mixed background, nf_{++} and nf_{--} as:

$$nf_{+-} = \sqrt{nf_{++} \cdot nf_{--}} \quad (19)$$

751 In the present analysis, the square root relation, Eq. (17), is violated by two independent factors. First, the relation
 752 does not hold true when pair cuts are applied to the spectra because pair cuts affect differently the unlike-sign and
 753 like-sign spectra. Second, elliptic flow induces an inherent distortion of the square root relation. Flow does not create
 754 or destroy particles. It only affects their azimuthal distribution and therefore in a perfect 2π detector there is no
 755 effect and Eq. (17) is obeyed. However, in the case of the PHENIX detector, which is not a 2π detector, the relation
 756 is violated as demonstrated in Appendix B. Relation (19) can still be used provided that the violation is the same in
 757 the data and the mixed events. In the present analysis, we make sure that this is the case. We start from a situation
 758 in which the mixed events satisfy Eq. (18). We then apply to the mixed events the pair cuts, exactly as to the
 759 foreground events, and the flow modulation using a weighting factor procedure that is based on an exact analytical
 760 calculation. Thus we make sure that Eq. (19) is still valid.

761

7. Quantitative understanding of the background

762 To illustrate our understanding of the background in quantitative terms, Fig. 16 shows a comparison of the MB
 763 mass spectra for the foreground and the calculated background like-sign pairs.

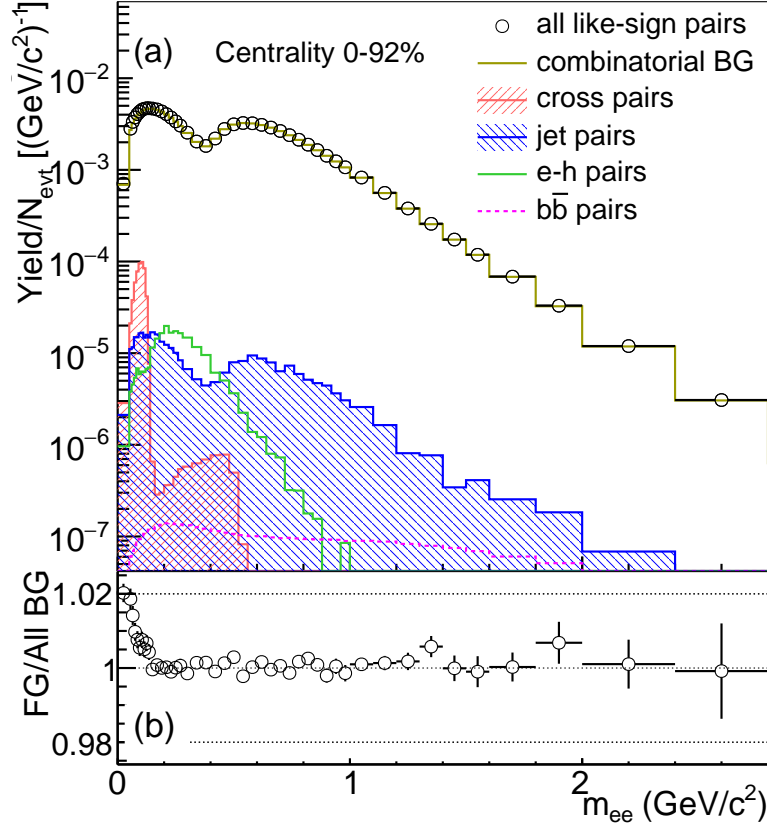


FIG. 16. (Color online) (a) Measured like-sign spectrum (open circles) together with the calculated background components (histograms) for MB events. (b) Ratio of the like-sign spectrum to the sum of all the background components.

764 The top panel shows the foreground like-sign mass spectrum (open circles) together with the various background
 765 components discussed above (the normalized combinatorial background, and the absolutely calculated cross pairs,
 766 jet pairs and e - h pairs) and the $b\bar{b}$ pairs calculated as described in Section IV. The bottom panel shows the ratio
 767 of the foreground like-sign spectrum to the sum of all the background components. Similar comparisons for the five
 768 centrality bins used in this analysis are shown in Fig. 17.

769 In general the background is well reproduced both in shape and magnitude. In particular, for the most central
 770 bins, the background is reproduced with sub-percent accuracy. There are, however, a couple of regions where the
 771 ratio foreground/background is different from one. There is a deviation of the order of a few percent at masses
 772 $m_{ee} < 100 \text{ MeV}/c^2$. This is clearly visible in the three most central bins. A number of factors could be responsible
 773 for this deviation, such as scale errors in the cross pairs or the jet pairs. However, in this mass region the signal
 774 to background ratio is relatively good as shown in Fig. 18 and a deviation of the order of a few percent in the
 775 background is negligible. There also seems to be a deviation at $m_{ee} > 1 \text{ GeV}/c^2$ for the 10%-20% and 20%-40%
 776 centrality bins. This deviation could indicate underestimations of the flow or the back-to-back jet contributions, due
 777 to the precision in these measurements, or the existence of an additional correlation that is not taken into account
 778 in any of the calculated background components. To be conservative, this deviation is considered as evidence of
 779 unsubtracted background and its magnitude is assigned as a mass dependent systematic uncertainty of the signal.

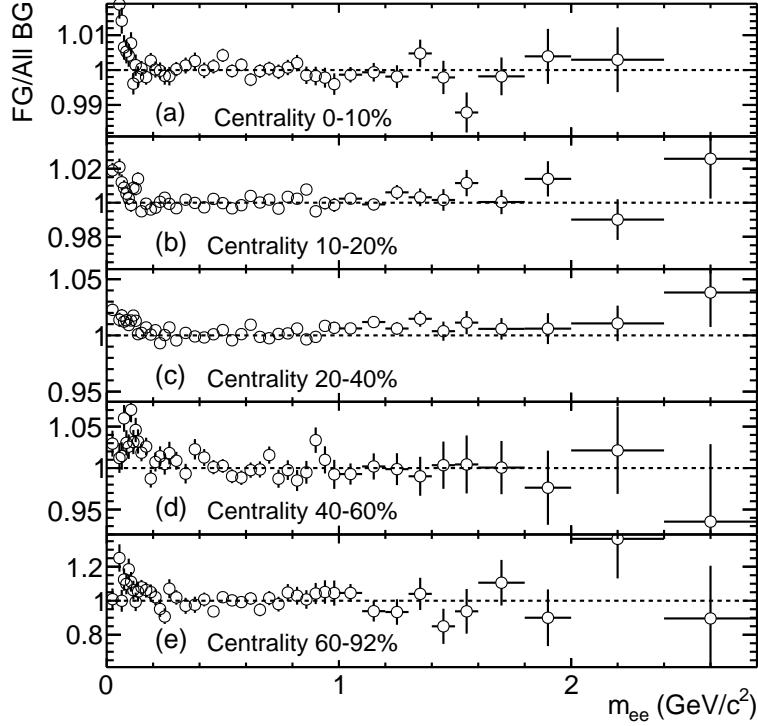


FIG. 17. Ratios of the like-sign foreground spectrum to the sum of all the background components for the five centrality bins used in this analysis.

780 Figure 18 shows the MB mass spectra of the foreground unlike sign events (FG_{+-}), the calculated total background
 781 (BG_{+-}) and the raw signal obtained by their subtraction. The signal to background ratio is shown in the bottom
 782 panel. This result will be discussed in reference to previously published PHENIX results in Section V C 1.

783 F. Raw Spectra and Efficiency Corrections

784 Figure 19 shows the raw mass spectra, obtained after subtracting the pair background, for the five centrality bins
 785 of this analysis.

786 To obtain the invariant mass spectrum inside the ideal PHENIX acceptance, the e^+e^- raw mass yield is corrected
 787 for reconstruction efficiency effects according to:

$$\frac{dN}{dm_{ee}} = \frac{1}{N_{\text{evt}}} \frac{N(m_{ee})}{\Delta m_{ee}} \frac{1}{\epsilon_{\text{pair}}^{\text{total}}} \quad (20)$$

788 where N_{evt} is the number of events, $N(m_{ee})$ is the number of e^+e^- pairs with invariant mass m_{ee} and Δm_{ee} is the
 789 mass bin width. $\epsilon_{\text{pair}}^{\text{total}}$ is the total pair reconstruction efficiency that includes the eID efficiency of the neural networks,

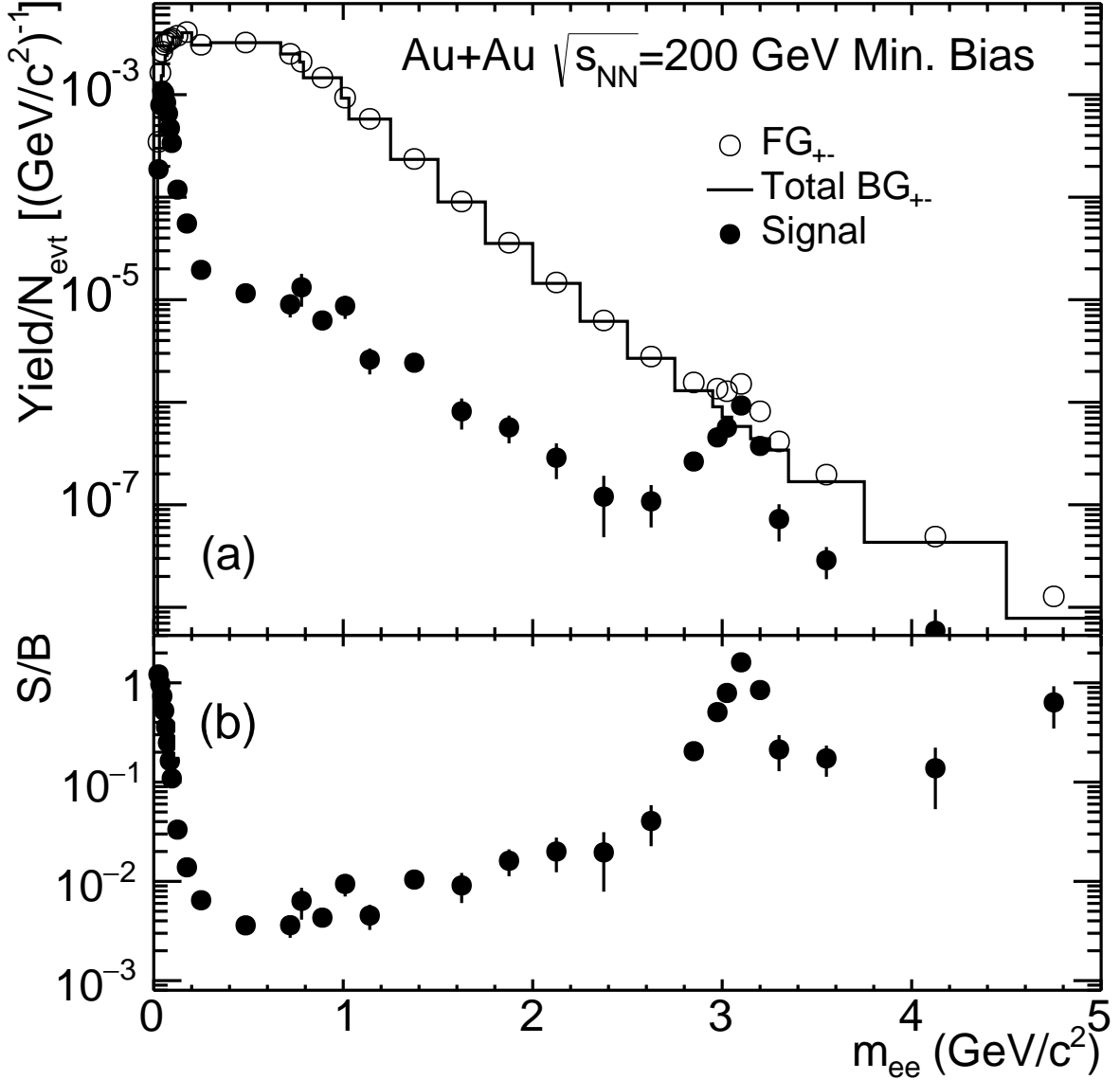


FIG. 18. (a) MB mass spectra of the unlike sign foreground events (FG_{+-}), the calculated total background (BG_{+-}) and the raw signal S . (b) The signal to background ratio.

790 losses incurred by dead or inactive areas in the detector, pair cut losses and detector occupancy effects. The total
 791 pair reconstruction efficiency $\epsilon_{\text{pair}}^{\text{total}}$ can thus be written as:

$$\epsilon_{\text{pair}}^{\text{total}} = \epsilon_{\text{pair}}^{\text{eID}} \cdot \epsilon_{\text{pair}}^{\text{live}} \cdot \epsilon_{\text{pair}}^{\text{ghost}} \cdot \epsilon_{\text{pair}}^{\text{mult}} \quad (21)$$

792 where $\epsilon_{\text{pair}}^{\text{eID}}$ is the e^+e^- pair reconstruction efficiency including the efficiency of all the electron identification cuts
 793 and the HBD double-hit rejection cut, $\epsilon_{\text{pair}}^{\text{live}}$ is the pair efficiency from the detector active area with respect to the
 794 ideal PHENIX detector acceptance, $\epsilon_{\text{pair}}^{\text{ghost}}$ reflects the efficiency loss due to the pair cuts that remove ghost pairs in
 795 the various detectors (see Section III D) and $\epsilon_{\text{pair}}^{\text{mult}}$ is the multiplicity dependent efficiency loss discussed below in this
 796 subsection.

797 The single electron reconstruction efficiency, defined as $\epsilon = \sqrt{\epsilon_{\text{pair}}^{\text{eID}} \cdot \epsilon_{\text{pair}}^{\text{mult}}}$ is shown in Fig. 20 vs p_T for the five
 798 centrality bins. This efficiency is not actually used in the analysis. It is shown here for illustration purposes. The
 799 change of efficiency below 0.3 GeV/c arises from the cut optimization in two p_T ranges (see Section III C 7).

800 The product $\epsilon_{\text{pair}}^{\text{eID}} \cdot \epsilon_{\text{pair}}^{\text{live}} \cdot \epsilon_{\text{pair}}^{\text{ghost}}$ is determined as follows. A cocktail of all the known hadronic sources contributing

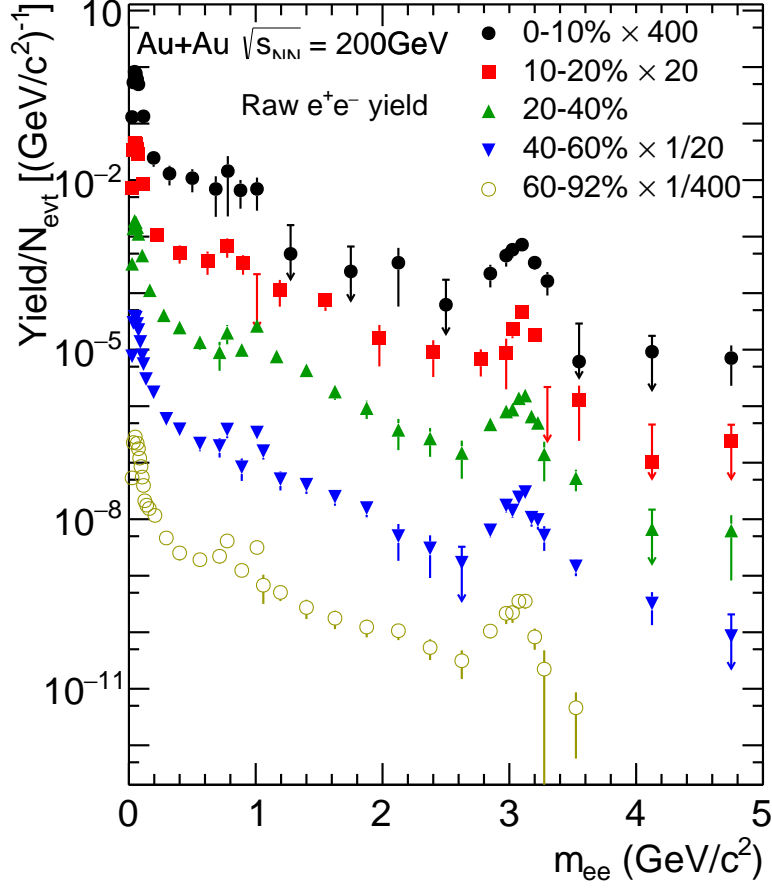


FIG. 19. (Color online) Raw mass spectra for the five centrality bins.

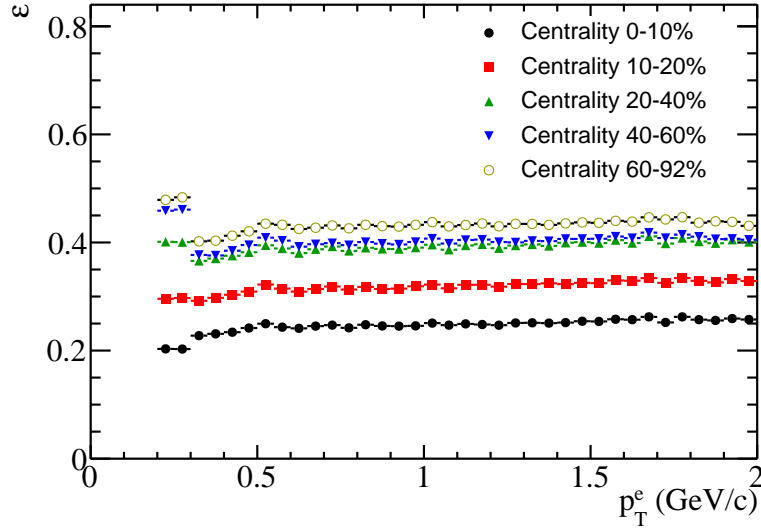


FIG. 20. (Color online) Single electron reconstruction efficiency vs. p_T for the five centrality bins.

⁸⁰¹ to the e^+e^- pair spectrum is generated within $|\eta| < 0.6$ and 2π in azimuthal angle. Details about the various sources
⁸⁰² of the cocktail are given in Section IV. The cocktail is passed through a full GEANT simulation of the PHENIX

803 detector [49] and analyzed in the same way as the data, including eID cuts, fiducial cuts and pair cuts. The resulting
 804 output is referred to as the reconstructed cocktail. The ratio of this reconstructed cocktail to the generated cocktail
 805 filtered through the ideal PHENIX acceptance (but without momentum smearing), gives the product $\epsilon_{\text{pair}}^{eID} \cdot \epsilon_{\text{pair}}^{\text{live}} \cdot \epsilon_{\text{pair}}^{\text{ghost}}$.
 806 This correction is derived in the two dimensional space of mass-pair p_T .

807 Special care is taken to tune the simulations to the data to ensure that the detector response in the simulations is
 808 the same as in real data for all the subsystems involved in the analysis. As an example, Fig. 21 shows a comparison of
 809 a few electron identification variables in data and simulations. For this comparison we use a clean sample of electrons
 810 provided by fully reconstructed π^0 Dalitz decays with an opening angle larger than 100 mrad from the 60%–92%
 811 centrality bin where the occupancy effects are very small and can be ignored. The eID variables of the two tracks
 812 from these pairs are compared to those of $\pi^0 \rightarrow e^+e^- \gamma$ simulations.

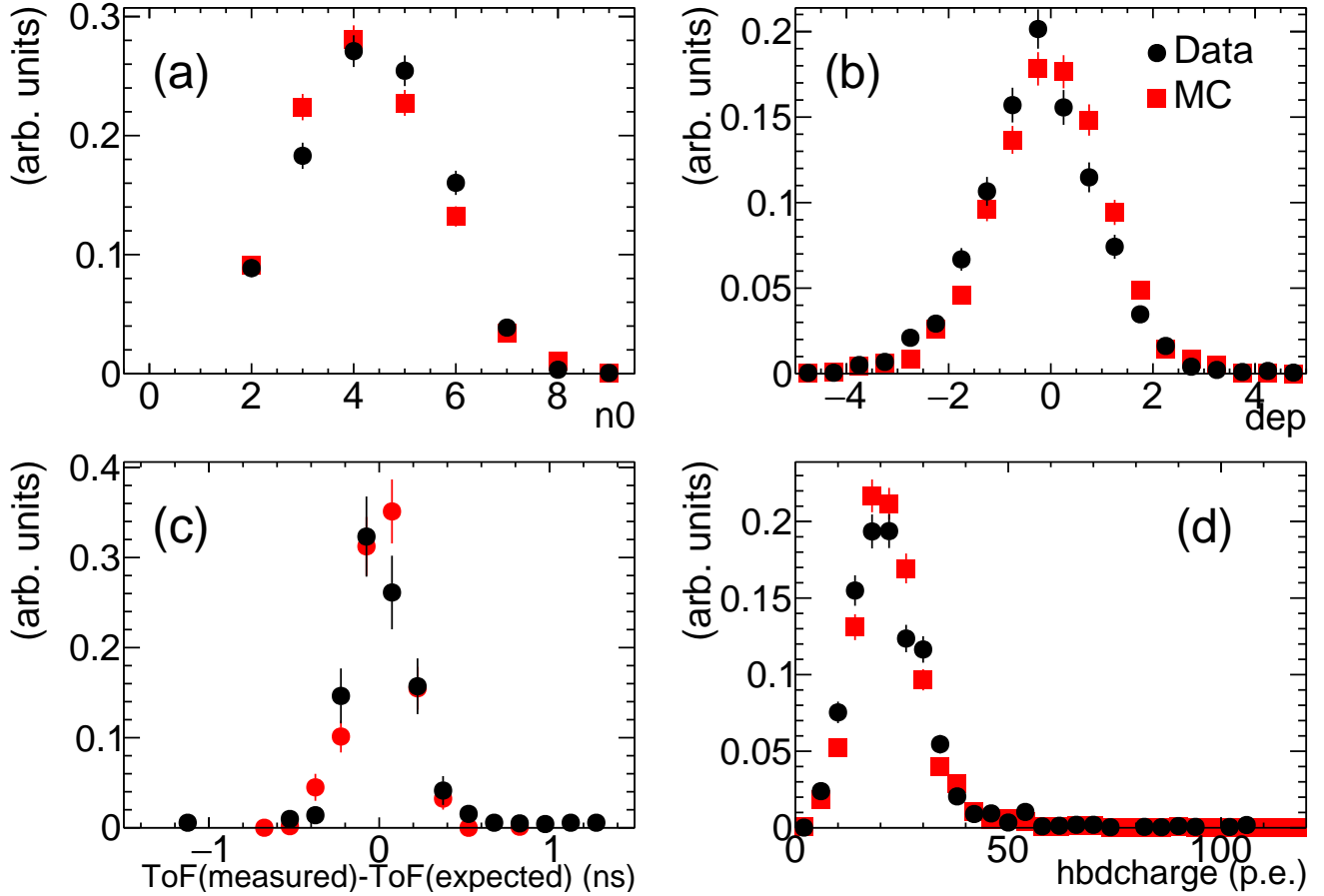


FIG. 21. (Color online) Comparison of electron identification variables in data (black) and in simulations (red). The variables are described in Section III C. electrons in data and simulations are from fully reconstructed π^0 Dalitz decays with opening angle larger than 100 mrad.

813 The HBD occupancy effects are taken into account by embedding the HBD hits from the cocktail simulation into
 814 real HBD events, and thus are included in the product $\epsilon_{\text{pair}}^{eID} \cdot \epsilon_{\text{pair}}^{\text{live}} \cdot \epsilon_{\text{pair}}^{\text{ghost}}$. There are two other occupancy effects in
 815 the central arms that need to be taken into account and are included in Eq. (21) by the additional multiplicative
 816 factor $\epsilon_{\text{pair}}^{\text{mult}}$. The first one is the decrease of track reconstruction efficiency as the detector occupancy increases with
 817 centrality. This loss is referred to as $\epsilon_{\text{pair}}^{\text{embed}}$ and is determined by an embedding procedure. Electrons from ϕ decays
 818 that are reconstructed in single particle simulations, are embedded into real Au+Au events. Then the embedded
 819 events are run through the full reconstruction software chain and analyzed in exactly the same way as the data. The
 820 embedding efficiency for single tracks $\epsilon_{\text{single}}^{\text{embed}}$ is determined as the ratio of the number of reconstructed electron tracks
 821 from embedded data to the number of embedded tracks. The pair embedding efficiency is calculated as the square of
 822 the single track embedding efficiency, $\epsilon_{\text{pair}}^{\text{embed}} = (\epsilon_{\text{single}}^{\text{embed}})^2$.

823 The second occupancy effect comes from the initial rejection of background electrons, discussed in Section III C 2,
 824 where PMTs fired by background electron tracks are removed. If such an electron is close to a signal electron in the

825 RICH, the associated PMTs of the signal electron are also removed. The probability for this to happen is relatively
 826 small and increases with multiplicity. This loss is referred to as $\epsilon_{\text{pair}}^{TPMT}$ and it is estimated by monitoring the yield of
 827 e^+e^- pairs below $20 \text{ MeV}/c^2$ before and after erasing the PMTs for each centrality bin. This mass region is dominated
 828 by Dalitz decays and γ conversions and provides a clean electron pair sample with a signal-to-background ratio of
 829 ~ 200 even for the most central events. Using these efficiency losses, $\epsilon_{\text{pair}}^{mult}$ can be expressed as:

$$\epsilon_{\text{pair}}^{mult} = \epsilon_{\text{pair}}^{embed} \cdot \epsilon_{\text{pair}}^{TPMT} \quad (22)$$

830 Table IV summarizes the values of $\epsilon_{\text{pair}}^{embed}$ and $\epsilon_{\text{pair}}^{TPMT}$ for the five centrality bins.

TABLE IV. Efficiency loss due to detector occupancy in the central arms $\epsilon_{\text{pair}}^{embed}$ and to the tagging of RICH PMTs discussed in Section III C 2 for the five centrality bins used in this analysis.

	Centrality				
	0%–10%	10%–20%	20%–40%	40%–60%	60%–92%
$\epsilon_{\text{pair}}^{embed}$	0.53	0.65	0.76	0.86	0.95
$\epsilon_{\text{pair}}^{TPMT}$	0.88	0.92	0.94	0.98	1.00

831 Figure 22 shows the total pair reconstruction efficiency $\epsilon_{\text{pair}}^{total}$ for pair p_T within $0.8\text{--}1.0 \text{ GeV}/c$ for each centrality
 832 bin.

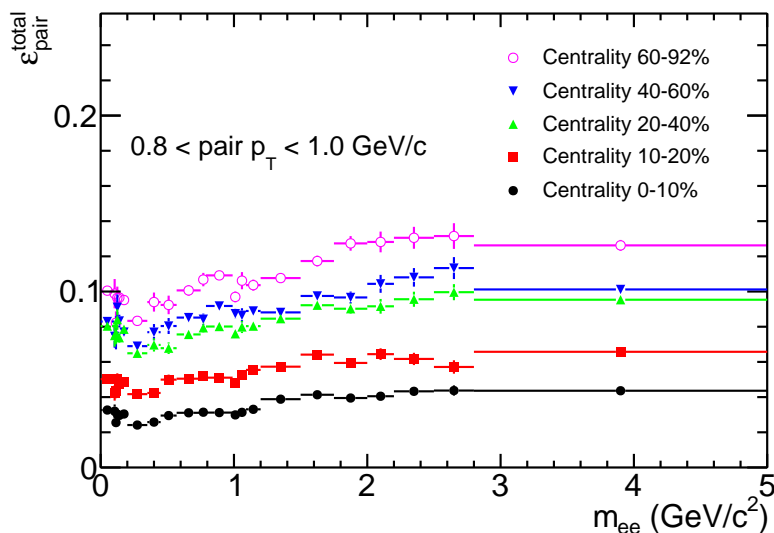


FIG. 22. (Color online) Pair efficiency correction for the pair p_T range between 0.8 and $1.0 \text{ GeV}/c$ for each centrality bin. This represents the total efficiency including the eID selection cuts based on neural networks, losses in the acceptance due to detector inactive areas, losses induced by the pair cuts and occupancy effects in the central arm detectors.

833

G. Systematic Uncertainties

834 The main systematic uncertainties on the corrected data arise from uncertainties on the electron identification, the
 835 acceptance and the background subtraction. They are discussed in detail below and summarized in Table V. These
 836 uncertainties move all data points in the same direction but not by the same factor

837

1. Systematic uncertainty on electron identification and occupancy effects

838 As described in Section III C, electron identification is achieved using three neural networks. Different threshold
 839 cuts for the neural networks result in different electron identification efficiency and occupancy effects. The thresholds

TABLE V. Summary of systematic uncertainties assigned to the corrected data for MB collisions.

Component	Mass range	Systematic uncertainty
eID + occupancy effects		$\pm 4\%$
Acceptance (time)		$\pm 8\%$
Acceptance (MC)		$\pm 4\%$
Combinatorial background	0–5 GeV/ c^2	$\pm 25\%$ ($m_{ee} = 0.6$ GeV/ c^2)
Residual yield	0–0.08 GeV/ c^2	-5% ($m_{ee} = 0.08$ GeV/ c^2)
Residual yield	1–5 GeV/ c^2	-15% ($m_{ee} = 1$ GeV/ c^2)

840 in the neural networks are varied by $\pm 20\%$ around the selected values and the variations of the electron pair yield
841 in the mass region $m_{ee} < 150$ MeV/ c^2 , after applying the efficiency correction, are used to assess the systematic
842 uncertainty of electron identification and occupancy effects.

843 By changing the thresholds by $\pm 20\%$ the raw electron pair yield changes by about $\pm 50\%$. However, once the
844 corresponding efficiency corrections are applied, the variations are below 4% for all the centrality bins. Based on
845 these results, we assign a $\pm 4\%$ systematic uncertainty on the electron identification.

846

2. Systematic uncertainty on the acceptance

847 We consider two sources of systematic uncertainties on the acceptance: variations of the pair acceptance vs time
848 and variations of the pair acceptance between data and MC simulations.

849 The pair acceptance systematic uncertainty vs time is studied by considering the variations of the number of electron
850 pairs per event for each run group. The weighted average of the *rms* of the number of electrons per event in the five
851 run groups is found to be 8% and it is taken as the systematic uncertainty of the acceptance variation over time.

852 The systematic uncertainty on the data vs MC pair acceptance is studied by comparing the reconstructed π^0
853 yield in data and simulations. In data we select reconstructed pairs with $m_{ee} < 100$ MeV/ c^2 , after subtracting the
854 combinatorial and correlated components of the background, using data from one of the run groups. In the MC
855 simulations we use reconstructed pairs in the same mass range from π^0 Dalitz decays applying the fiducial cuts for the
856 corresponding run group. The entire detector is divided into four sectors. Data and MC simulations are normalized
857 in one sector. The variations of the yield ratios between data and MC simulations in the other sectors ranges between
858 1% and 8%. The weighted average of these variations is found to be 4% and it is taken as the systematic uncertainty
859 of the acceptance agreement between data and MC simulations.

860

3. Systematic uncertainty on the background subtraction

861 We consider two sources of systematic uncertainties on the background subtraction:

862 (i) Uncertainty on the combinatorial background subtraction. It is primarily due to the uncertainty in the normal-
863 ization factor, and the latter is determined by the statistics in the normalization window, namely by $1/\sqrt{N_{LS}}$ (see
864 Section III E 6). This translates into a relative uncertainty of the signal $\delta S/S = 1/\sqrt{N_{LS}} \times B/S$. The ratio B/S
865 depends both on mass and centrality. In Table V we quote the uncertainty at $m_{ee} = 0.6$ GeV/ c^2 which represents
866 the worst case in mass, for MB events. The centrality dependence results in variations of the order of 15% from the
867 MB values.

868 (ii) In the ideal case, the like-sign residual yield, i.e. the like-sign yield after subtracting all the background sources,
869 should be zero. In practice it is not. As shown in Figs. 16 and 17, there is a small residual yield. In this analysis,
870 we assume that any residual yield is entirely due to unsubtracted background, and we take it as an additional source
871 of systematic uncertainty, after transforming it into unlike-sign residual yield via the acceptance correction factor α .
872 This uncertainty takes into account any possible discrepancy in shape or magnitude of the various subtracted sources
873 of background. The factor α accounts for the different acceptance of the PHENIX detector for like and unlike sign
874 pairs. It is calculated as a function of pair mass and pair p_T using the mixed event background as:

$$\alpha(m, p_T) = \frac{MIX_{+-}(m, p_T)}{MIX_{++}(m, p_T) + MIX_{--}(m, p_T)} \quad (23)$$

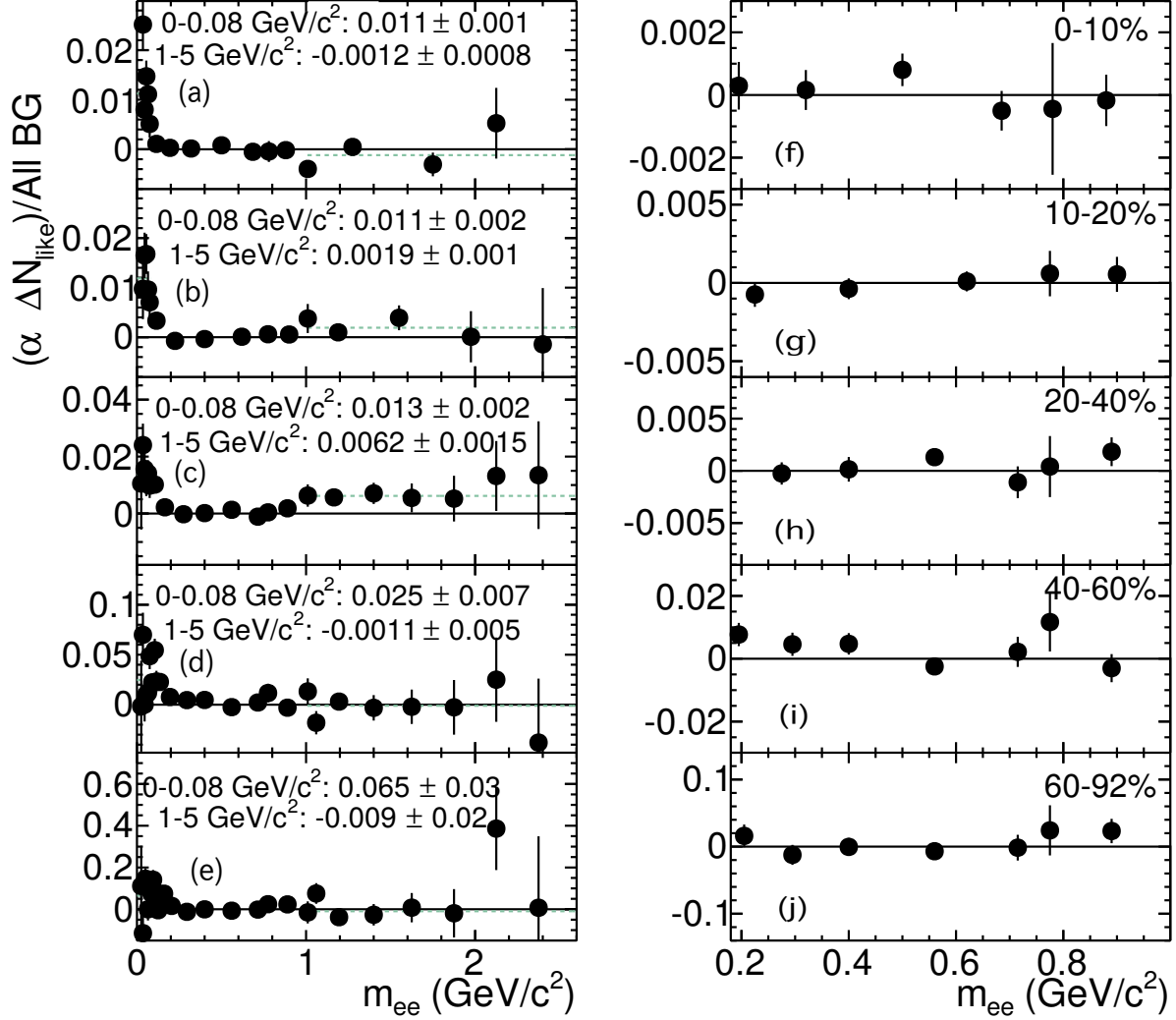


FIG. 23. (Color online) (a–e) Unlike-sign residual background yield derived from the like-sign residual yield, obtained after subtracting all background sources, via the acceptance correction factor α (see text). The legend and the dashed lines show the results of constant fits below $80 \text{ MeV}/c^2$ and above $1 \text{ GeV}/c^2$. (f–j) Zoomed views in the vertical axis for the $0.2-1 \text{ GeV}/c^2$ mass range.

875 Figure 23 panels (a)–(e) show α times the like-sign residual yield divided by the sum of all unlike-sign background
 876 sources as a function of mass for the five centrality bins, which represent the relative residual background yield
 877 in the unlike sign mass spectrum. The mass regions $m_{ee} < 0.08 \text{ GeV}/c^2$, $0.2 \text{ GeV}/c^2 < m_{ee} < 1.0 \text{ GeV}/c^2$ and
 878 $m_{ee} > 1 \text{ GeV}/c^2$ are fitted to a constant to quantify the magnitude of the residual unlike-sign yield. The fit results
 879 are also shown. Figure 23 panels (f)–(j) show zoomed views in the vertical axis for the $0.2-1 \text{ GeV}/c^2$ mass range. The
 880 fits in the mass region $m_{ee} = 0.2-1.0 \text{ GeV}/c^2$ give results that are consistent with zero for all centrality bins. For the
 881 other two mass ranges, the residual yields are considered as sources of systematic uncertainties if their significance is
 882 larger than 2σ .

883 The total systematic uncertainty in the background subtraction is obtained as the quadratic sum of the systematic
 884 uncertainties due to the combinatorial background subtraction and the residual yield. Both contributions are listed in
 885 Table V for MB collisions. It is worth noting that the systematic uncertainty of the background subtraction is much
 886 lower than the required accuracy to measure a signal with the S/B values shown in Section III E 7.

H. Cross checks

A second independent analysis was performed as a cross check. The key features of the second analysis are discussed here. A more detailed description is given in Appendix C. The second analysis is similar to the analysis described in Ref. [23], but it makes use of the HBD and includes all the important improvements developed in this work. In particular, it makes use of the time-of-flight information for better hadron rejection, implements the shape distortion of the mixed event background due to elliptic flow (Section III E 2), subtracts the correlated electron-hadron background (Section III E 5), and explicitly considers the away-side jet-pair component in the background subtraction (Section III E 4).

Important elements of the independent analysis are different from those of the main analysis. The most significant differences are: (i) The HBD underlying event subtraction is done using the average charge in the vicinity of a track as opposed to the average charge in a module as used in the main analysis. (ii) Electron identification is achieved by a sequence of independent one-dimensional cuts on each of the electron identification variables instead of the neural network approach. (iii) The normalization of each background source is determined from a fit to the like-sign spectra, in contrast to the main analysis where all the correlated background sources are absolutely normalized and only the combinatorial background is normalized to the like sign spectra.

The second analysis results in a factor of two smaller signal-to-background ratio and a 10% reduction in purity of the electron sample in central collisions. However, once corrected for efficiency, the results of the second analysis are consistent within uncertainties with those obtained with the main analysis described in this section.

IV. COCKTAIL OF HADRONIC SOURCES

In this section we describe the procedures used to calculate the expected dielectron yield from hadronic decays, commonly referred to as the hadronic cocktail, that will be compared to the experimental results in Section V. The known e^+e^- sources are calculated using the EXODUS, PYTHIA and MC@NLO event generators. EXODUS is a phenomenological generator that simulates phase space distributions of the relevant electron sources and their decays [50]. It generates the photonic sources, i.e. Dalitz decays of light neutral mesons: $\pi^0, \eta, \eta' \rightarrow e^+e^-\gamma$ and $\omega \rightarrow e^+e^-\pi^0$ and the nonphotonic sources, i.e. dielectron decays of mesons: $\rho, \omega, \phi, J/\psi \rightarrow e^+e^-$. PYTHIA [46] and MC@NLO [51, 52] are used to generate the correlated pairs from semi-leptonic decays of heavy flavor (charm and bottom) mesons. The hadrons are assumed to have uniform pseudorapidity density within $|\eta| < 0.35$ and uniform azimuthal distribution in 2π . Once generated, the sources are filtered through the ideal acceptance of the PHENIX detector and smeared with the detector resolution for comparison to the measured invariant mass spectrum.

A. Neutral pions

The dominant electron source as well as the fundamental input for EXODUS is π^0 . The shape of the π^0 p_T distribution is parameterized as:

$$E \frac{d^3\sigma}{d^3p} \propto \frac{1}{(e^{-ap_T - bp_T^2} + p_T/p_0)^n} \quad (24)$$

The parameters, a, b, p_0 and n , are obtained by a simultaneous fit of the PHENIX published results for π^0 [53, 54] and charged pions [55]. The resulting fit parameters are shown in Table VI for the five centrality bins of this analysis. The absolute magnitude of the π^0 rapidity density, dN_{π^0}/dy , is obtained by fitting the cocktail to the data (see Section IV D).

TABLE VI. Fit parameters derived from the π^0 and charged pion p_T distributions [53–55] for different centralities using Eq. (24).

Parameter	0%–10%	10%–20%	20%–40%	40%–60%	60%–92%
a [(GeV/c) $^{-1}$]	0.57	0.53	0.43	0.36	0.33
b [(GeV/c) $^{-2}$]	0.19	0.16	0.11	0.13	0.088
p_0 [GeV/c]	0.74	0.75	0.79	0.76	0.74
n	8.4	8.3	8.5	8.4	8.4

B. Other mesons

The p_T distributions of other light mesons are based on the parametrization of the pion spectrum assuming m_T scaling [23], i.e. Eq. (24) is used with p_T replaced by $\sqrt{p_T^2 + m_{meson}^2 - m_{\pi^0}^2}$. This assumption reproduces well the measured light meson p_T distributions in Au+Au collisions as demonstrated in [23]. The absolute normalization for each meson is provided by the ratio of the meson to π^0 invariant yield at high p_T ($p_T \geq 5$ GeV/ c). We use the values from Ref. [44], summarized in Table VII.

TABLE VII. Meson to π^0 ratio at high p_T ($p_T \geq 5$ GeV/ c) obtained from PHENIX data in $p+p$ collisions [44].

η/π^0	ρ/π^0	ω/π^0	η'/π^0	ϕ/π^0
0.48	1.0	0.90	0.25	0.40

The values were obtained from $p+p$ collisions and are taken to be valid for Au+Au collisions because at high p_T the suppression of all mesons is found to be very similar to the π^0 suppression and consequently the meson/ π^0 ratios in Au+Au collisions remain unchanged with respect to the ratios in $p+p$ collisions [56–58].

For the p_T distribution of the J/ψ we use the neutral pion p_T spectrum measured in $p+p$ collisions [47], assuming m_T scaling. Detector effects on the J/ψ line shape are taken into account by passing the decay e^+e^- through a GEANT simulation of the PHENIX detector. The resulting p_T integrated invariant e^+e^- mass distribution is then normalized to the measured cross section in $p+p$ collisions [23] and scaled to Au+Au collisions by the corresponding $\langle N_{coll} \rangle$ and the measured R_{AA} for each centrality bin [59].

C. Open heavy flavor

The correlated e^+e^- yield from open heavy flavor decays is simulated using two different $p+p$ event generators, PYTHIA and MC@NLO, and measured $c\bar{c}$ and $b\bar{b}$ production cross sections.

PYTHIA simulations are used to calculate gluon fusion, the dominant process for heavy-quark production, in leading-order perturbative QCD. Specifically, we use PYTHIA-6 [60]² and CTEQ5L as input parton distribution functions. The MC@NLO package (vers. 4.03) [51, 52] is a next-to-leading order simulation that generates hard scattering events. These events are subsequently fed to HERWIG (vers. 6.520) [61] for fragmentation in vacuum.

We use the $c\bar{c}$ - and $b\bar{b}$ -production cross sections measured by PHENIX [62], by fitting the event generator (PYTHIA or MC@NLO) output to the measured dielectron mass spectrum in $d+Au$ collisions for $m_{e^+e^-} > 1.15$ GeV/ c^2 . These cross sections were scaled by the average number of $d+Au$ binary collisions ($\langle N_{coll} \rangle$) to give the $p+p$ equivalent cross section. For $b\bar{b}$, both generators gave within uncertainties the same result for the cross section extrapolated to zero invariant mass [62]:

$$\left. \frac{d\sigma_{b\bar{b}}^{pp}}{dy} \right|_{y=0} = 1.36 \pm 0.32(\text{stat}) \pm 0.44(\text{syst}) \mu\text{b} \quad (25)$$

The $c\bar{c}$ cross section strongly depends on the event generator. The MC@NLO yields the following cross section [62]:

$$\left. \frac{d\sigma_{c\bar{c}}^{pp}}{dy} \right|_{y=0} = 287 \pm 29(\text{stat}) \pm 100(\text{syst}) \mu\text{b} \quad (26)$$

whereas PYTHIA gives:

$$\left. \frac{d\sigma_{c\bar{c}}^{pp}}{dy} \right|_{y=0} = 106 \pm 9(\text{stat}) \pm 33(\text{syst}) \mu\text{b} \quad (27)$$

This cross section, derived from e^+e^- data in $d+Au$ collisions, is consistent within uncertainties with the cross section derived from measurements of single electrons from semileptonic decays of heavy flavor mesons in $p+p$ collisions,

² We use PYTHIA-6 [60] with the following parameters MSEL[$c\bar{c}$]=4 or MSEL[$b\bar{b}$]=5, MSTP(91)=1, PARP(91)=1.5, MSTP(33)=1, PARP(31)=1.0, MSTP(32)=4, PMAS(4)=1.25, PMAS(5)=4.1.

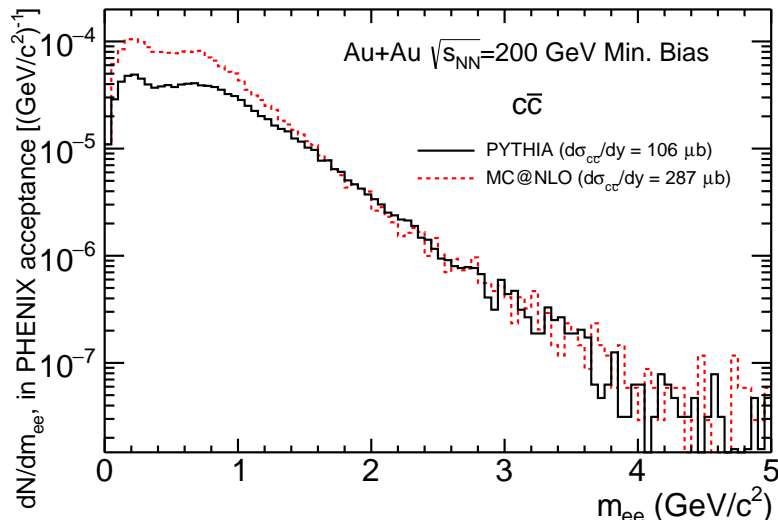


FIG. 24. (Color online) Comparison of the invariant dielectron yield from correlated heavy flavor meson decays for MB Au+Au collisions calculated with PYTHIA (solid line) and MC@NLO (dashed line) using the $d\sigma_{c\bar{c}}^{pp}/dy$ cross sections of $106 \mu\text{b}$ and $287 \mu\text{b}$, respectively [62], scaled by $\langle N_{\text{coll}} \rangle$.

953 extrapolated to $p_T = 0 \text{ GeV}/c$ using PYTHIA simulations [44]. MC@NLO was not used to derive the heavy flavor cross
 954 section from measurements of single electrons.

955 The two results, Eqs. (26) and (27), although consistent within $\sim 1.2 \sigma$, yield central values which differ by a factor
 956 of ~ 2.5 . This difference comes mainly from the extrapolation of the dilepton yield from $m_{ee} > 1.15 \text{ GeV}/c^2$ to m_{ee}
 957 $= 0 \text{ GeV}/c^2$, as illustrated in Fig. 24. Figure 24 also shows an absolute comparison of the PYTHIA and MC@NLO
 958 dielectron invariant yields from correlated heavy flavor meson decays in MB Au+Au collisions, obtained by N_{coll}
 959 scaling of the $p+p$ cross sections quoted in Eqs. (26) and (27). At high masses, $m_{ee} > 1.15 \text{ GeV}/c^2$, both generators
 960 give by construction the same yield, with a very small difference in shape. However, at low masses there is a large
 961 discrepancy in the absolute yield.

962 The $d+\text{Au}$ (as well as the $p+p$) inclusive dilepton yield is not very sensitive to this variation of the cross section
 963 because the large effect at low masses is diluted by the contributions from light meson decays. The situation is
 964 quite different in Au+Au collisions. The yield from light meson decays scales approximately with N_{part} , whereas the
 965 contribution from heavy flavor scales with N_{coll} making the latter dominant at low-masses in central collisions. The
 966 choice of the generator used to simulate the $c\bar{c}$ contribution will therefore affect the total cocktail yield at low masses
 967 and will influence the interpretation of the Au+Au data in terms of an excess with respect to the cocktail. The results
 968 will be presented in the next section using PYTHIA for an easier comparison with previously published results but
 969 both generators, PYTHIA and MC@NLO, will be considered in the discussion.

970 D. Cocktail normalization

971 In the present analysis we use the precisely measured e^+e^- data at low masses to derive the normalization of the
 972 cocktail of hadronic sources. In the restricted phase space defined by $m_{ee} < 0.1 \text{ GeV}/c^2$ and $p_T/m_{ee} > 5$ the inclusive
 973 e^+e^- yield is dominated by π^0 Dalitz decays with a small contribution of direct virtual photons and an even smaller
 974 contribution of η Dalitz decays. To a very good approximation the mass spectrum of these three sources has a $1/m_{ee}$
 975 dependence and their relative magnitude is well known. The ratio of direct photons to π^0 is known from PHENIX
 976 measurements [63, 64] and the ratio of η to π^0 can be easily obtained from the PHENIX measurement at high p_T [58]
 977 and the m_T scaling as described in Section IV B. By fitting the cocktail+direct virtual photons to the data in the
 978 restricted phase space defined above, one obtains the rapidity density dN_{π^0}/dy that determines the normalization of
 979 the cocktail. The values are found to be consistent with measurements of neutral and charged pions [53–55] within
 980 the systematic uncertainties of cocktail and data.

981 Alternatively, the cocktail can be absolutely normalized using the π^0 rapidity density dN_{π^0}/dy derived from these
 982 measurements as done in Ref. [23]. The cocktails obtained with these two procedures are compared in Fig. 25. The
 983 results differ at masses $m_{ee} < 100 \text{ MeV}/c^2$ by about 25% which is approximately the contribution of the virtual direct

984 photons. However, for the mass range of interest, that is typically $0.3\text{--}0.76\text{ GeV}/c^2$, the difference is smaller and
 985 amounts to only 15%. In this mass range, the yield is dominated by the contributions from correlated heavy flavor
 986 decays and changing dN_{π^0}/dy by $\sim 25\%$ has a minor effect on the inclusive e^+e^- yield. At even higher masses, m_{ee}
 987 $> 1\text{ GeV}/c^2$, the two procedures yield exactly the same results. The present procedure is adopted to be consistent
 988 with the known contribution of internal conversion.

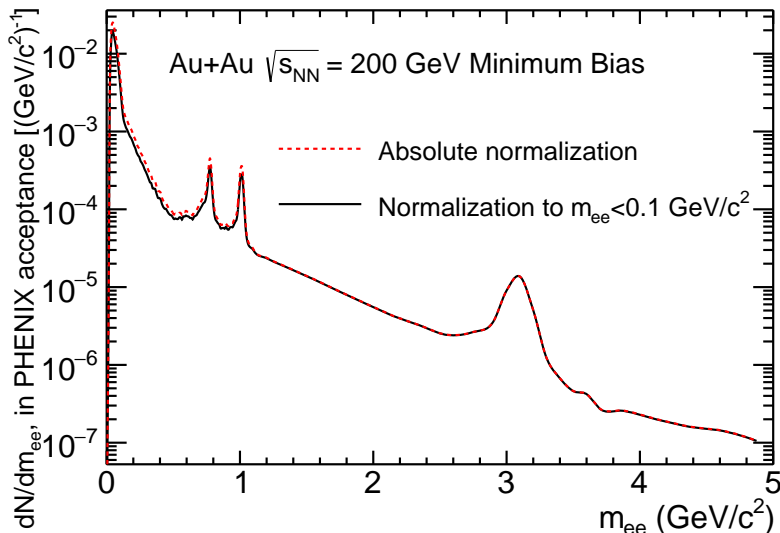


FIG. 25. (Color online) Cocktail of hadronic sources for the 2010 run with normalization provided by fitting to the present e^+e^- invariant yield at masses $m_{ee} < 0.1\text{ GeV}/c^2$ (black line) or with absolute normalization to the π^0 rapidity density derived from measurements of neutral and charged pions [53–55] (dashed line).

989 E. Systematic uncertainties on the cocktail

990 The systematic uncertainties of the cocktail ingredients are estimated and propagated to determine the total cocktail
 991 systematic uncertainty. The following uncertainties are considered:

992 (i) Light meson to π^0 ratio: We adopt the same systematic uncertainties used in Ref. [23], namely $\pm 30\%$ for η , ω
 993 and ϕ , $\pm 33\%$ for ρ and $\pm 100\%$ for η' .

994 (ii) Direct photon: The systematic uncertainties in the direct photon dN/dy are taken from Ref. [64]. They range
 995 from $\pm 24\%$ to $\pm 70\%$ from central to peripheral collisions, respectively.

996 (iii) Open heavy flavor ($c\bar{c}$, $b\bar{b}$): We use the systematic uncertainties of the open heavy flavor cross sections given
 997 in Eqs. (26) or (27) for $c\bar{c}$ and (25) for $b\bar{b}$, taken from Ref. [62]. The $\langle N_{\text{coll}} \rangle$ systematic uncertainties shown in Table
 998 II are added in quadrature when the $p+p$ cross sections are scaled to Au+Au collisions.

999 (iv) J/ψ : The systematic uncertainty of the J/ψ cross section in $p+p$ collisions is estimated to be $\pm 14\%$ [65]. The
 1000 systematic uncertainties in $\langle N_{\text{coll}} \rangle$ and $J/\psi R_{AA}$ are added in quadrature. The R_{AA} uncertainties are taken from
 1001 Ref. [59], ranging from $\pm 22\%$ to $\pm 35\%$ depending on centrality.

1002 A summary of the cocktail systematic uncertainties is presented graphically in Fig. 26, which shows the systematic
 1003 uncertainty of each cocktail component together with the total cocktail systematic uncertainty, determined as their
 1004 quadratic sum.

1005 F. The Au+Au Cocktail

1006 The cocktail, calculated as described above, using the PYTHIA generator for the open heavy flavor contributions, is
 1007 presented in Fig. 27 for MB Au+Au collisions together with the individual components of the cocktail. For comparison,
 1008 Fig. 27 also shows the total cocktail using MC@NLO for the open heavy flavor contributions. The differences discussed
 1009 above in Section IV C are clearly reflected in this comparison.

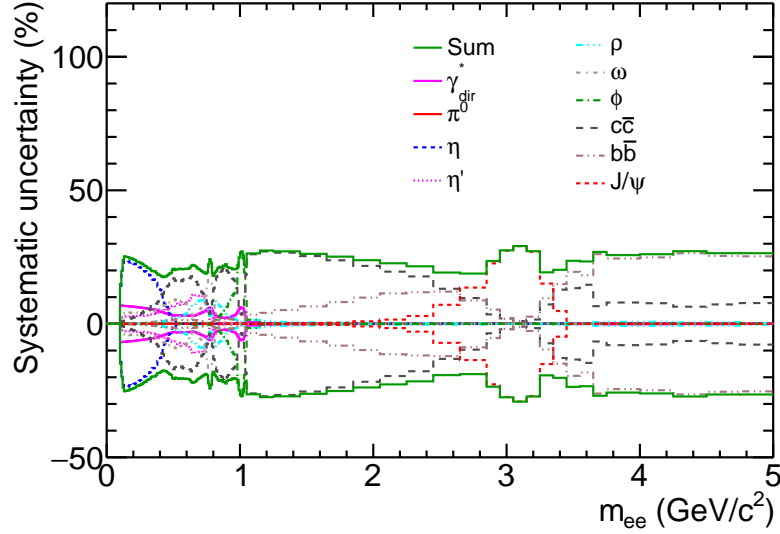


FIG. 26. (Color online) Systematic uncertainties assigned to each cocktail component and the total cocktail systematic uncertainty for MB events.

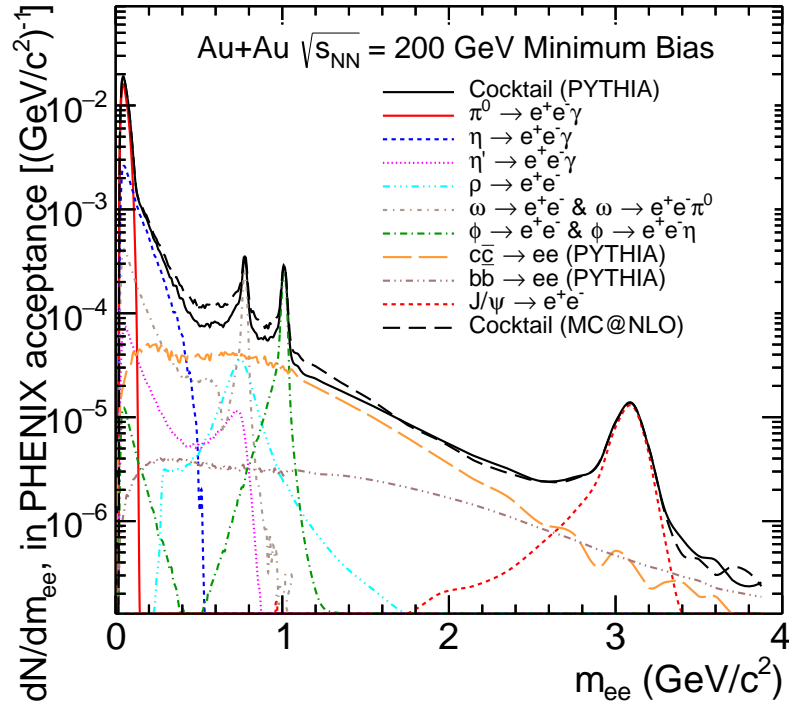


FIG. 27. (Color online) Cocktail of hadronic sources for the 2010 run (black solid line) using the PYTHIA generator for the open heavy flavor contributions. The individual components of the cocktail are also shown. For comparison, the total cocktail using MC@NLO is shown (black dashed line).

1010

V. RESULTS AND DISCUSSION

1011

A. Invariant mass spectra

1012 Figure 28 shows the invariant mass spectrum of e^+e^- pairs within the PHENIX acceptance (as defined in Section
1013 II E 1) for MB Au+Au collisions. The spectra are subject to a p_T cut of 0.2 GeV/c on the single electron tracks

1014 and to a 100 mrad cut on the pair opening angle. Statistical and systematic uncertainties on the data points are
 1015 shown separately by vertical bars and boxes, respectively. Figure 28 also compares the measured spectrum to the
 1016 cocktail of expected e^+e^- sources, where PYTHIA is used to calculate the correlated pairs from heavy flavor decays.
 1017 The individual contributions to the cocktail are shown in the figure.

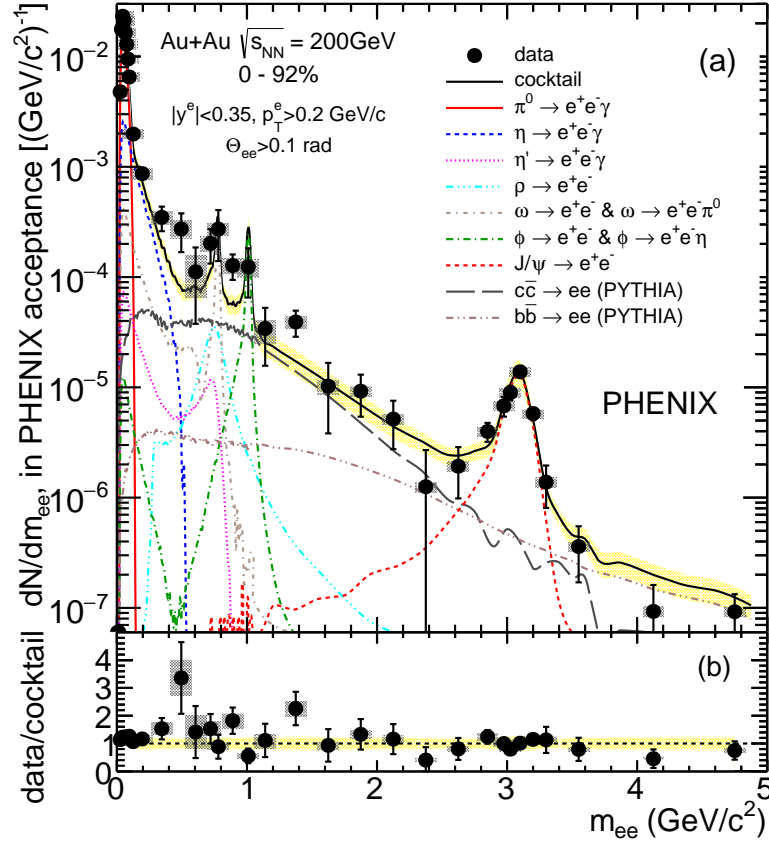


FIG. 28. (Color online) Invariant mass spectrum of e^+e^- pairs in MB Au+Au collisions within the PHENIX acceptance compared to the cocktail of expected decays.

1018 See Section IV for details about the cocktail calculation. The total systematic uncertainty of the cocktail is shown
 1019 by the yellow band. The bottom panel shows the ratio of data to cocktail.

1020 Figure 29 shows the invariant mass spectra of e^+e^- pairs for the five centrality bins analyzed in this work, compared
 1021 to the cocktail.

1022 For a more detailed discussion of the centrality and transverse momentum dependencies of the dielectron yield, we
 1023 consider three mass regions:

1024

1025 (a) the mass region $m_{ee} < 0.10 \text{ GeV}/c^2$ that is dominated by the π^0 Dalitz decay.

1026

1027 (b) the low-mass region (LMR), $0.30 < m_{ee} < 0.76 \text{ GeV}/c^2$, below the ρ meson mass, that is the most sensitive
 1028 region to in-medium effects.

1029

1030 (c) the intermediate-mass region (IMR), $1.2 < m_{ee} < 2.8 \text{ GeV}/c^2$, that is dominated by the correlated pairs from
 1031 the semi-leptonic decays of charm and bottom mesons.

1032

1033 Figure 30 shows the pair p_T distribution for these three mass intervals in MB collisions. In the following sections
 1034 we discuss the results in these three mass intervals.

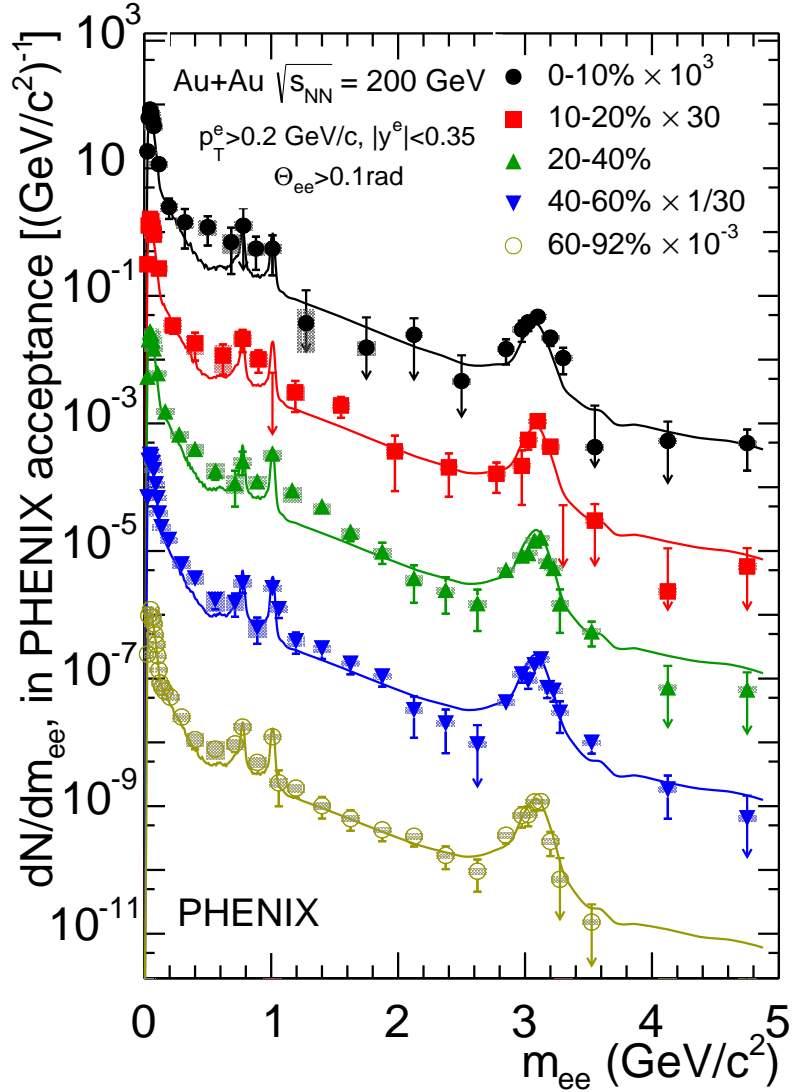


FIG. 29. (Color online) Invariant mass spectra of e^+e^- pairs in Au+Au collisions within the PHENIX acceptance for the various centrality bins. The lines represent the total expected yield from all the sources indicated in Fig. 28.

1035

B. π^0 Dalitz region

1036 The mass region $m_{ee} < 0.10 \text{ GeV}/c^2$ is dominated by the π^0 Dalitz decay with a small contribution of direct virtual
 1037 photons of $\sim 20\%$ and an even smaller contribution of the η Dalitz decay of $\sim 10\%$. We discuss here only the shape
 1038 of the p_T distribution because the integrated dielectron yield in this mass interval was used to normalize the cocktail
 1039 for the five centrality bins as described in Section IV. Figure 30 compares the measured dielectron p_T distribution
 1040 for MB collisions in this mass interval to the p_T distribution of the hadronic cocktail that uses the parametrization
 1041 for the π^0 and η mesons [Eq. (24)]. The agreement between the two distributions, in shape and magnitude, is very
 1042 good when adding the measured yield of direct virtual photons.

1043

C. Low-mass region (LMR)

1044 In the LMR, the yield is expected to be saturated by the light mesons (η, ρ and ω) and the $c\bar{c}$ contribution. Figure
 1045 28 shows an enhancement of e^+e^- pairs with respect to the cocktail in MB collisions. The enhancement develops with
 1046 centrality as shown in Fig. 29 and it appears to be distributed over the whole p_T range covered by the measurement,
 1047 as can be seen in Fig. 30. We quantify the effect by the enhancement factor defined as the ratio of the measured

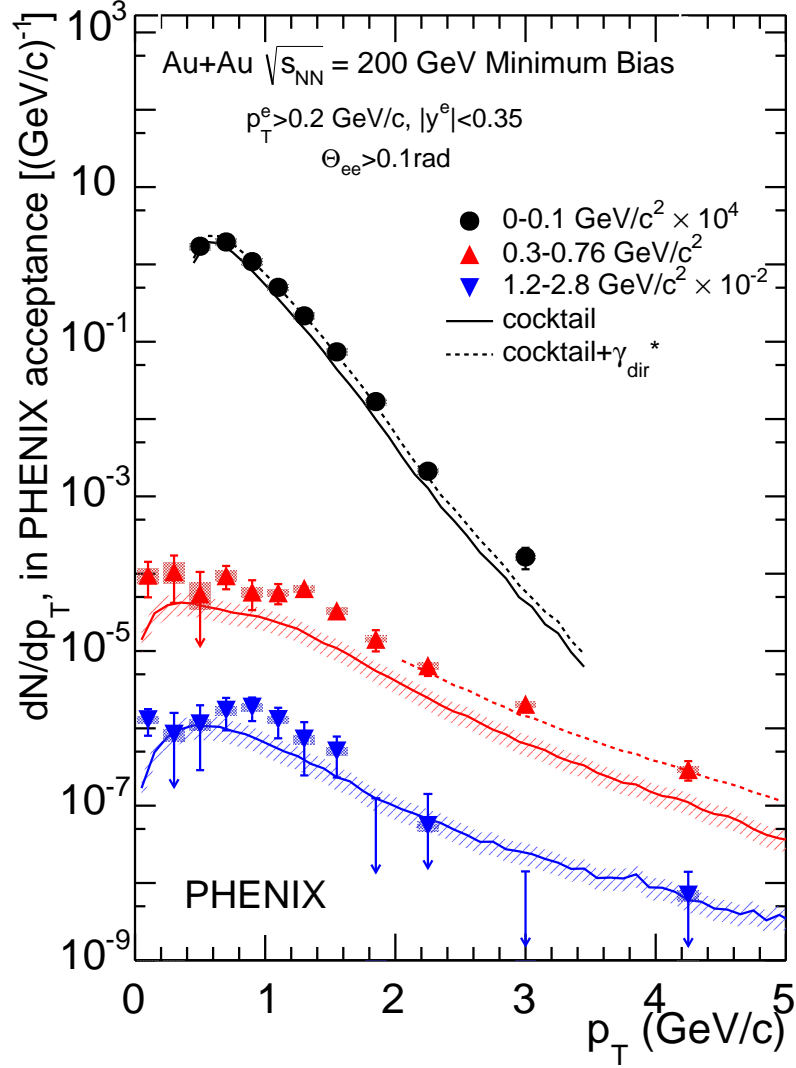


FIG. 30. (Color online) MB invariant p_T distributions for three mass windows as indicated in the legend. The solid lines represent the expected p_T distributions of the hadronic cocktail and the shadowed bands around the lines represent the cocktail systematic uncertainties. The dotted lines include the contribution from direct photons in the phase space region where they can reliably be calculated, i.e. $p_T/m_{ee} > 5$.

1048 over expected dilepton yield integrated in the LMR. As discussed in Section IV C, the cocktail yield in this mass
 1049 region depends on the generator, PYTHIA or MC@NLO, used to calculate the open heavy flavor contribution. The
 1050 enhancement factors obtained with PYTHIA are shown as a function of centrality in Fig. 31 and they are listed in
 1051 in Table VIII for the two cases. The enhancement factors are approximately 40% higher when PYTHIA is used to
 1052 calculate the open heavy flavor contribution instead of MC@NLO.

1053

1. Comparison to previous PHENIX results

1054 The enhancement factors quoted above are significantly smaller than those previously reported by PHENIX [23]
 1055 in the same Au+Au collision system at the same energy of $\sqrt{s_{NN}} = 200$ GeV. There are a number of significant
 1056 differences, both qualitative and quantitative, between the two analyses:

- 1057 • Hadron contamination: The purity of the electron sample is very different in the two cases. In [23] the hadron
 1058 contamination was 30% in central Au+Au collisions, whereas in the present analysis, the HBD enabled this
 1059 contamination to be reduced to less than 5% at all centralities.

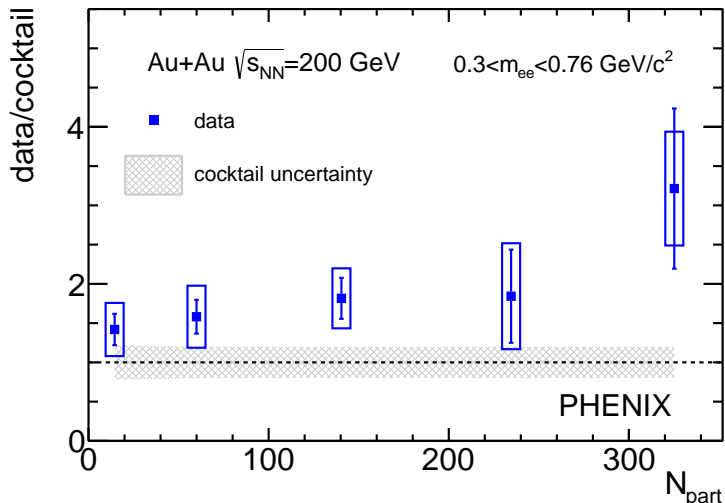


FIG. 31. (Color online) Data to cocktail (using PYTHIA for heavy flavor contribution) ratio in the LMR versus centrality. The shaded band around one represents the cocktail systematic uncertainty.

TABLE VIII. Enhancement factors, defined as the ratio of measured over expected dilepton yield in the mass region $m_{ee} = 0.30\text{--}0.76 \text{ GeV}/c^2$, for the five centrality bins and for MB. The enhancement factors are quoted separately for the two cases where the correlated yield from $c\bar{c}$ decays is calculated with PYTHIA or MC@NLO. The \pm model uncertainties represent the cocktail systematic uncertainties.

Centrality	Enhancement factor \pm stat \pm syst \pm model	
	MC@NLO $c\bar{c}$	PYTHIA $c\bar{c}$
MB	$1.7 \pm 0.3 \pm 0.3 \pm 0.2$	$2.3 \pm 0.4 \pm 0.4 \pm 0.2$
0%–10%	$2.3 \pm 0.7 \pm 0.5 \pm 0.2$	$3.2 \pm 1.0 \pm 0.7 \pm 0.2$
10%–20%	$1.3 \pm 0.4 \pm 0.5 \pm 0.2$	$1.8 \pm 0.6 \pm 0.7 \pm 0.2$
20%–40%	$1.4 \pm 0.2 \pm 0.3 \pm 0.2$	$1.8 \pm 0.3 \pm 0.4 \pm 0.2$
40%–60%	$1.2 \pm 0.2 \pm 0.3 \pm 0.2$	$1.6 \pm 0.2 \pm 0.4 \pm 0.2$
60%–92%	$1.0 \pm 0.1 \pm 0.2 \pm 0.2$	$1.4 \pm 0.2 \pm 0.3 \pm 0.2$

- 1060
- Signal sensitivity: The signal sensitivity is usually quantified by the signal to background S/B ratio. The S/B values displayed in Fig. 18 are similar to those quoted in Ref. [23]. This is however, a misleading comparison, because in a situation of subpercent S/B ratio, the magnitude of S critically depends on the accuracy of the background subtraction. A better way to assess the sensitivity of the measurement is provided by the cocktail/background, C/B , ratio. From the signal/background ratio and the enhancement factors quoted in Ref. [23], we estimate an average value of C/B over the mass range $m_{ee} = 0.15\text{--}0.75 \text{ GeV}/c^2$ of $\sim 1/600$ in MB collisions. In the present analysis the same ratio is found to be $\sim 1/250$. In addition to that, one should take into account that in the 2010 run with the $+-$ field configuration there is a larger track acceptance of $\sim 20\%$. This rough estimate indicates that at the same multiplicity the signal sensitivity in the present analysis is larger by a factor of ~ 3.5 compared to the previous one.
- 1070
- Pair cuts: Loose pair cuts were applied in Ref. [23] compared to the cuts used in this analysis. The cuts used in Ref. [23] are found to leave a sizable amount of detector induced correlation in the mass region $m_{ee} = 0.4\text{--}0.6 \text{ GeV}/c^2$.
- 1073
- Flow: As demonstrated in Section III E 2 the collective flow that is inherent to nuclear collisions, affects the shape of the combinatorial component of the background and violates the square root relation [Eq. (17)]. These two effects were not taken into account in the data analysis of Ref. [23].
- 1076
- Electron-hadron pairs: As shown in Section III E 5, the $e-h$ pairs originate in the central arm detectors and in particular in the RICH detector. This source of correlated pairs was not considered in [23].
- 1077

- Away-side jet component: The away-side jet component of the correlated background was found to be negligible in [23] and only the near-side jet component was considered. In the present analysis, both components are absolutely calculated. The away-side component is indeed relatively small but both components are considered and subtracted.
- Background subtraction procedure: In Ref. [23], the shapes of the three components of the background (combinatorial background, cross pairs and near-side jet) were calculated whereas their absolute scales were obtained by fitting to the like-sign spectra. In the present analysis, all components of the correlated background (cross pairs, jet pairs and electron-hadron pairs) are calculated and subtracted in absolute terms. There is only one free parameter in the background subtraction procedure, namely the normalization factor of the combinatorial background.

In conclusion, we do not confirm our previous report of a large excess seen in the LMR [23]. The differences listed above affect the yield in the mass region where the excess was reported but not always in the same direction. For example, the loose pair cuts lead to under subtraction of the background whereas neglecting the flow modulation, has the opposite effect namely it leads to over subtraction in the mass region where the excess was observed. These differences also do not affect the unlike-sign yield by a similar magnitude. The hadron contamination, the loose pair cuts and the electron-hadron pairs are the most significant ones in this respect. Taking all the differences together, the present analysis is much improved compared to the previous one and we thus consider the previous result on the low-mass excess to be superseded by the results presented here.

2. Comparison to STAR results

Recently, STAR published results on e^+e^- production in Au+Au collisions at $\sqrt{s_{NN}} = 200$ GeV [66, 67]. In the same mass range of $m_{ee} = 0.30\text{--}0.76$ GeV/ c^2 , STAR observes an excess of dielectrons and quotes a value of $1.77 \pm 0.11^{stat} \pm 0.24^{syst} \pm 0.33^{model}$ in MB collisions, for the ratio of the dielectron yield to the hadronic cocktail excluding the ρ meson contribution. There are two factors that should be taken into account when comparing the STAR results with those quoted in Table VIII. First, excluding the ρ contribution results in an increase of about 10% of the data to cocktail ratio. Second, STAR uses PYTHIA with a charm cross section $d\sigma_{c\bar{c}}/dy = 171 \pm 26 \mu\text{b}$ [66] which is between the PHENIX cross sections quoted in Section IV for PYTHIA and MC@NLO. Taking those two differences into account, as well as the experimental uncertainties, we find that the results of the two experiments are consistent in the LMR. The centrality and p_T dependencies of the enhancement reported in [67] are also consistent with our results.

D. Intermediate-mass region (IMR)

The IMR is dominated by correlated pairs from the semi-leptonic decays of $D\bar{D}$ mesons, with a small contribution from $B\bar{B}$ mesons and an even smaller contribution from Drell Yan. The latter is neglected in the cocktail calculation. This mass interval is singled out by theory as the most sensitive window to identify the thermal radiation of the QGP in the dilepton spectrum [68, 69].

The results displayed in Figs. 28 and 29 show a small enhancement of dileptons in the IMR with respect to the yield from $c\bar{c}$ decays calculated using PYTHIA. The enhancement factors are shown in Fig. 32 as a function of centrality and the values are listed in Table IX. The results are consistent with those of Ref. [23] within the large experimental uncertainties of the latter. There is very little difference in the dilepton yield in this mass interval if MC@NLO is used instead of PYTHIA, as demonstrated in Fig. 27. The shapes are very similar and the integral yields in the IMR differ by less than 10% in the two cases.

Using PYTHIA, the enhancement factor in MB events is ~ 1 standard deviation away from unity. However, the data to cocktail comparison discussed above, represents an extreme case in which it is assumed that the correlations between the $c\bar{c}$ pairs in Au+Au collisions are the same as in $p+p$ collisions. It is however, well known that heavy flavor quarks exhibit energy loss and collective flow in the medium formed in Au+Au collisions, as manifested for example in measurements of single electrons [44, 70]. This should affect the correlation between the e^+e^- pairs from $c\bar{c}$ decays. Lacking a suitable generator to model this effect, we consider also the opposite extreme approach in which we assume that the pair is totally decorrelated. The invariant mass is calculated using two electrons randomly selected from the measured p_T distribution of single electrons from heavy flavor decays [44], with uniform distributions in pseudorapidity and azimuthal angle. The pair is filtered through the ideal PHENIX acceptance and the integral is normalized to the calculated PYTHIA yield from $c\bar{c}$ decays. This extreme case results in a softer mass distribution in the IMR as can be seen in Fig. 33.

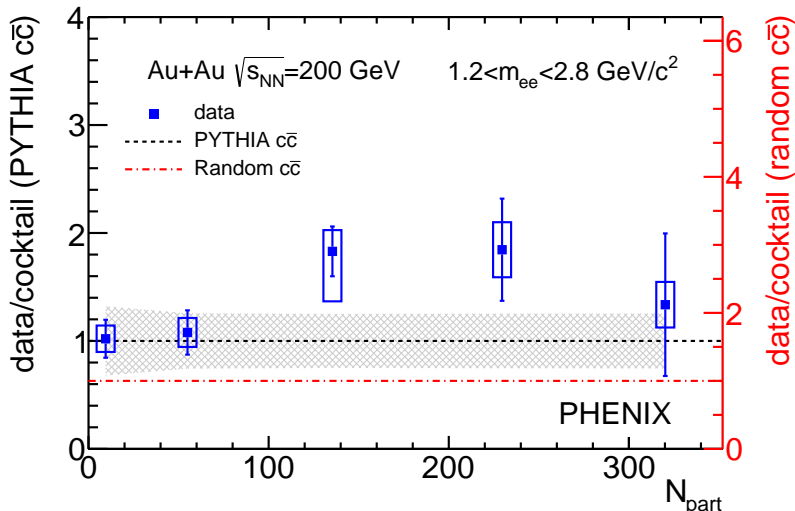


FIG. 32. (Color online) Data to cocktail ratio in the IMR versus centrality. The cocktail uses PYTHIA for the $c\bar{c}$ contribution (left scale) or random $c\bar{c}$ contribution (right scale). The shaded band represents the PYTHIA cocktail systematic uncertainty. The same uncertainty applies also to the random $c\bar{c}$ cocktail.

TABLE IX. Enhancement factors, defined as the ratio of measured to expected dilepton yield in the mass region $m_{ee} = 1.2$ – 2.8 GeV/c^2 , calculated using PYTHIA for the five centrality bins and for minimum bias. The last line gives the enhancement factor assuming random correlation (see text).

	Centrality	Enh. factor $\pm\text{stat}$ $\pm\text{syst}$ $\pm\text{model}$
PYTHIA $c\bar{c}$	0%–10%	$1.3 \pm 0.7 \pm 0.2 \pm 0.3$
	10%–20%	$1.8 \pm 0.5 \pm 0.3 \pm 0.3$
	20%–40%	$1.8 \pm 0.2 \pm_{-0.5}^{+0.2} \pm 0.3$
	40%–60%	$1.1 \pm 0.2 \pm 0.1 \pm 0.3$
	60%–92%	$1.0 \pm 0.2 \pm 0.1 \pm 0.3$
	MB	$1.5 \pm 0.3 \pm 0.2 \pm 0.3$
MB (random $c\bar{c}$)		$2.5 \pm 0.5 \pm 0.3 \pm 0.3$

1129 There is a small yield depletion at high masses compensated by a higher yield at low masses. The integral in the
 1130 IMR is lower resulting in enhancement factors that are $\sim 70\%$ larger compared to those derived from PYTHIA. The
 1131 enhancement factor in MB collisions is quoted in the last line of Table IX and the centrality dependence is seen by
 1132 comparing the data points to the dot-dashed line in Fig. 32.

1133 E. Comparison to theory

1134 In this section we compare our results to the model originally developed by Rapp and Wambach [71, 72]. The model
 1135 uses an effective Lagrangian and a many body approach to compute the electromagnetic spectral function which is
 1136 the main factor in the calculation of the dilepton production rates. In the LMR, the spectral function is saturated
 1137 via vector meson dominance, by the light vector mesons, in particular the ρ meson, whereas at larger masses it is
 1138 dominated by multipion states or equivalently, via quark-hadron duality, by $q\bar{q}$ annihilation. The dilepton yields are
 1139 obtained by an appropriate integration of the thermal rates over the space-time evolution of the fireball. This model
 1140 was very successful in reproducing the low-mass dilepton enhancement discovered at SPS by the CERES experiment
 1141 and later further studied by the NA60 experiment. In the comparison below, we use an improved version of the model
 1142 that incorporates recent developments, a nonperturbative QGP equation of state and QGP emission rates, i.e. $q\bar{q}$

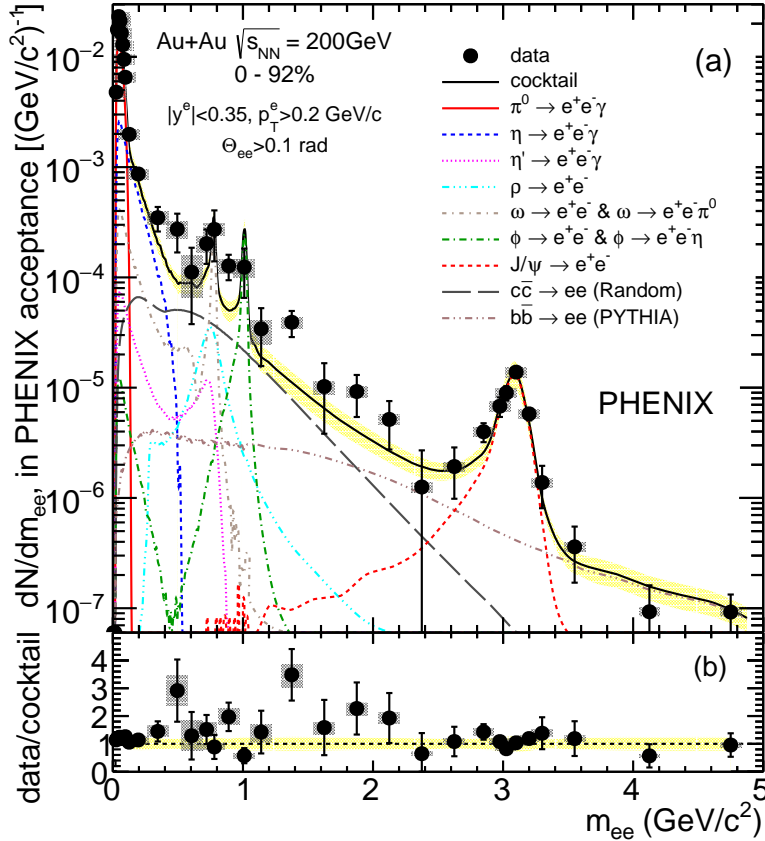


FIG. 33. (Color online) Invariant mass spectrum of e^+e^- pairs in MB Au+Au collisions within the PHENIX acceptance compared to the cocktail of expected decays when the $c\bar{c}$ decay component is calculated assuming no correlation between the c and \bar{c} .

1143 annihilation at temperatures higher than the critical temperature, both based on lattice QCD [73]. It is important
 1144 to note that this updated version preserves the agreement with the SPS data and also reproduces the RHIC results
 1145 from STAR.

1146 Figures 34 and 35 compare the invariant mass spectrum and the LMR pair p_T distribution with the model calcu-
 1147 lations for MB collisions [74]. The main components, in-medium ρ broadening, QGP thermal radiation and cocktail
 1148 excluding the ρ , together with their sum, are shown separately.

1149 In both figures the data are consistent with the calculations. Within this model, the enhancement in the LMR
 1150 originates from the in-medium ρ broadening, i.e. the thermal radiation of the hadronic phase, with a very small
 1151 contribution from the QGP.

1152 In the model, the centrality dependence of the thermal radiation is reasonably well described, within an uncertainty
 1153 of $\sim 10\%$, by a power-law scaling of the charged particle rapidity density $(dN_{ch}/dy)^\alpha$, with $\alpha \simeq 1.45$ [73], very similar to
 1154 the scaling of the thermal photon yield [64, 69]. Within uncertainties, the present data are consistent with this scaling
 1155 as illustrated in Fig. 36, which also shows the centrality dependence of the excess, i.e. the data after subtracting the
 1156 cocktail without the vacuum ρ , together with the expected power-law scaling (dashed line).

1157 VI. SUMMARY AND CONCLUSIONS

1158 PHENIX has measured invariant mass spectra, p_T distributions and the centrality dependence of the e^+e^- pair
 1159 production in Au+Au collisions at $\sqrt{s_{NN}} = 200$ GeV. The use of the HBD provided additional electron identification
 1160 to the central arm detectors, additional hadron rejection and increased rejection of the combinatorial background.

1161 A new analysis procedure based on neural networks has been developed that combines in an efficient way the
 1162 information from the HBD and the central arm detectors, RICH, TOF and EMCal. This results in three independent
 1163 parameters for electron identification, hadron rejection and close pair rejection, instead of the fourteen parameters of
 1164 the four detectors involved in these tasks. A quantitative understanding of the total background at the subpercent level

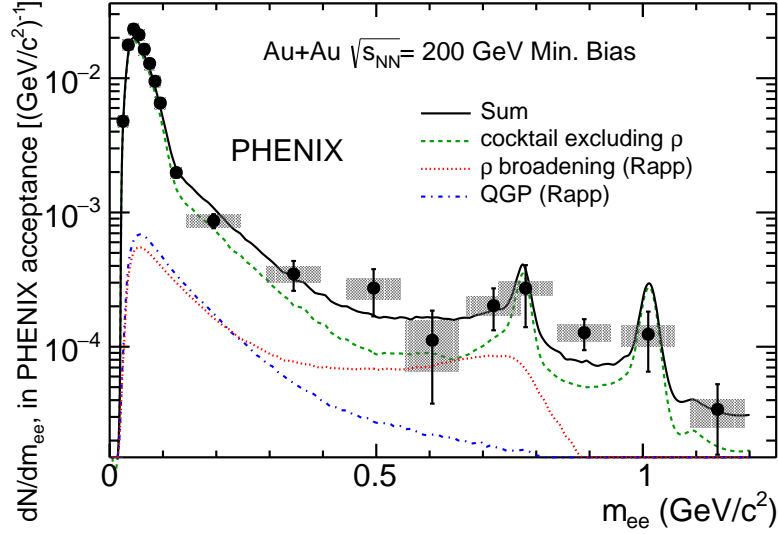


FIG. 34. (Color online) MB invariant mass spectrum compared to the model calculations of Rapp (solid line) [74]. The main contributions, the in-medium ρ broadening (dotted line), the QGP thermal radiation (dot-dashed line) and the cocktail excluding the ρ (dashed line) are also shown.

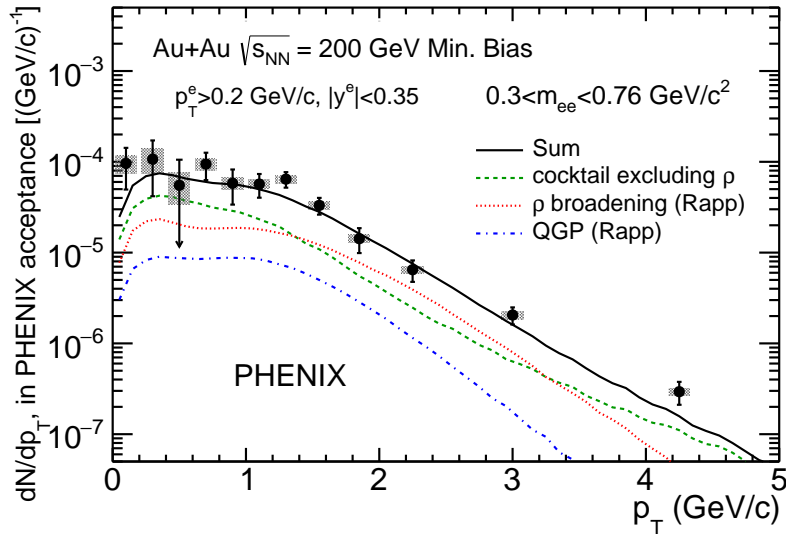


FIG. 35. (Color online) Dielectron p_T distribution in the LMR compared to model calculations (solid line) [74]. The main contributions, the in-medium ρ broadening (dotted line), the QGP thermal radiation (dot-dashed line) and the cocktail excluding the ρ (dashed line) are also shown.

1165 is achieved in the most central collisions. This is realized by a precise evaluation of all the background sources. The
 1166 combinatorial background is determined by the event mixing technique together with an exact weighting procedure
 1167 to take into account the flow effects that are inherent in the foreground events and cannot be reproduced in the
 1168 mixed events. All the correlated background sources are calculated in absolute terms using simulations and published
 1169 results.

1170 The results are compared with a cocktail of the known e^+e^- sources. The contributions from light hadron decays
 1171 that dominate the e^+e^- yield at low masses $m_{ee} < 1 \text{ GeV}/c^2$, are determined using PHENIX measurements for pions
 1172 and m_T scaling for other mesons. The contributions from semileptonic decays of heavy flavor (charm and bottom)
 1173 mesons are calculated with the PYTHIA or MC@NLO generators using $\langle N_{\text{coll}} \rangle$ scaled $p+p$ cross sections. Both generators
 1174 give very similar yields in the IMR. However, they predict very dissimilar results that differ from each other by a
 1175 factor of ~ 2 in the LMR. Precise measurements of the charm cross section over the entire phase space are needed to

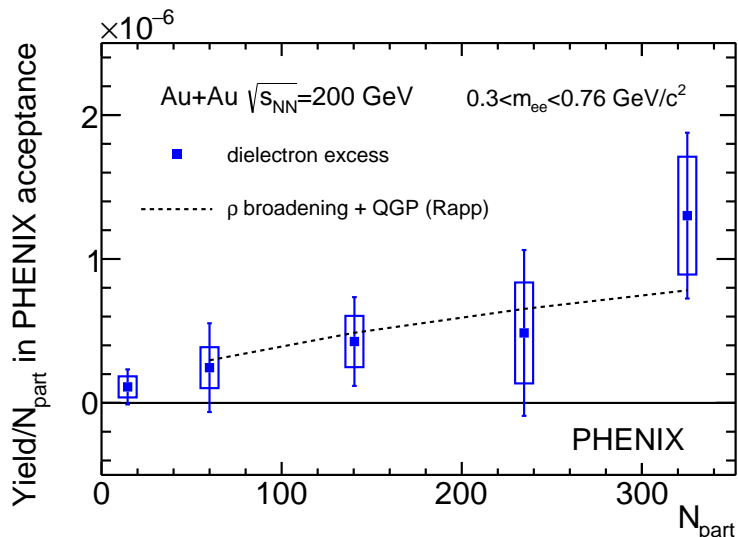


FIG. 36. (Color online) Centrality dependence of the dielectron excess, defined as (data – cocktail excluding ρ) compared to the thermal radiation from the hadronic (ρ broadening) and QGP phases from model calculations (dashed line) [74].

1176 resolve this discrepancy.

1177 A small enhancement of e^+e^- is observed in the LMR with respect to the cocktail. The enhancement is distributed
 1178 over the entire p_T range measured ($p_T < 5$ GeV/ c). It increases with centrality and amounts to $2.3 \pm 0.4(\text{stat}) \pm$
 1179 $0.4(\text{syst}) \pm 0.2^{\text{model}}$ for MB collisions when PYTHIA is used to calculate the open heavy flavor contribution. If instead
 1180 MC@NLO is used, the enhancement factors are $\sim 40\%$ smaller and for MB collisions it is found to be $1.7 \pm 0.3(\text{stat}) \pm$
 1181 $0.3(\text{syst}) \pm 0.2^{\text{model}}$. The large enhancement of e^+e^- pairs in the LMR previously reported by PHENIX, in Au+Au
 1182 collisions at $\sqrt{s_{NN}} = 200$ GeV [23], is not confirmed by the results of the present improved analysis. In particular,
 1183 the concentration of the excess at low p_T ($p_T < 1$ GeV/ c) is not observed here. The present results are consistent
 1184 with those recently published by the STAR Collaboration [66] within the uncertainties of the two experiments.

1185 In the IMR, the results are compared with calculations of the expected yield from the semileptonic decays of heavy
 1186 flavor mesons in two extreme scenarios. In the first scenario, the heavy flavor contribution is calculated assuming that
 1187 the correlations between the $c\bar{c}$ are the same in Au+Au as in $p+p$ collisions, ignoring decorrelation effects produced
 1188 by the interactions of heavy flavor quarks with the medium. A small enhancement is observed with respect to the
 1189 yield predicted by PYTHIA. It amounts to $1.5 \pm 0.3(\text{stat}) \pm 0.2(\text{syst}) \pm 0.3^{\text{model}}$ for MB collisions. In the other
 1190 scenario, the opposite extreme approach is adopted where the pair is assumed to be totally decorrelated. In this case,
 1191 the enhancement factor becomes $2.5 \pm 0.5(\text{stat}) \pm 0.3(\text{syst}) \pm 0.3^{\text{model}}$. The reality is somewhere between these two
 1192 extreme cases and we conclude that there is room in the data for a significant additional contribution, for example of
 1193 thermal radiation, in the IMR. The nature of the IMR pairs will be studied with high statistics Au+Au data in 2014
 1194 data taking with the silicon vertex tracker (VTX) installed in PHENIX.

1195 The results in the LMR are compared to calculations based on the model originally developed by Rapp and
 1196 Wambach [71, 72] with subsequent improvements that incorporate recent developments [73]. The model includes
 1197 thermal radiation emission from the QGP phase ($q\bar{q}$ annihilation) as well as from the hadronic phase (mainly from
 1198 the ρ meson copiously produced by pion annihilation, $\pi^+\pi^- \rightarrow \rho \rightarrow e^+e^-$). The invariant mass and p_T distributions
 1199 as well as the centrality dependence are well reproduced by the calculations. The enhancement observed in the LMR
 1200 from SPS up to RHIC energies is thus consistently reproduced by a single model. Within this model, the enhancement
 1201 originates from the melting of the ρ meson resonance as the system approaches chiral symmetry restoration.

1202 ACKNOWLEDGMENTS

1203 We thank the staff of the Collider-Accelerator and Physics Departments at Brookhaven National Laboratory and
 1204 the staff of the other PHENIX participating institutions for their vital contributions. We also thank R. Rapp for
 1205 providing us the results of his model calculations and for helpful discussions. We acknowledge support from the Office
 1206 of Nuclear Physics in the Office of Science of the Department of Energy, the National Science Foundation, Abilene
 1207 Christian University Research Council, Research Foundation of SUNY, and Dean of the College of Arts and Sciences,

1208 Vanderbilt University (U.S.A), Ministry of Education, Culture, Sports, Science, and Technology and the Japan Society
 1209 for the Promotion of Science (Japan), Conselho Nacional de Desenvolvimento Científico e Tecnológico and Fundação
 1210 de Amparo à Pesquisa do Estado de São Paulo (Brazil), Natural Science Foundation of China (People's Republic
 1211 of China), Croatian Science Foundation and Ministry of Science, Education, and Sports (Croatia), Ministry of Edu-
 1212 cation, Youth and Sports (Czech Republic), Centre National de la Recherche Scientifique, Commissariat à l'Énergie
 1213 Atomique, and Institut National de Physique Nucléaire et de Physique des Particules (France), Bundesministerium
 1214 für Bildung und Forschung, Deutscher Akademischer Austausch Dienst, and Alexander von Humboldt Stiftung (Ger-
 1215 many), National Science Fund, OTKA, Károly Róbert University College, and the Ch. Simonyi Fund (Hungary),
 1216 Department of Atomic Energy and Department of Science and Technology (India), Israel Science Foundation (Israel),
 1217 Basic Science Research Program through NRF of the Ministry of Education (Korea), Physics Department, Lahore
 1218 University of Management Sciences (Pakistan), Ministry of Education and Science, Russian Academy of Sciences,
 1219 Federal Agency of Atomic Energy (Russia), VR and Wallenberg Foundation (Sweden), the U.S. Civilian Research and
 1220 Development Foundation for the Independent States of the Former Soviet Union, the Hungarian American Enterprise
 1221 Scholarship Fund, and the US-Israel Binational Science Foundation.

1222

Appendix A: Introducing Flow in the Mixed Events

1223 In this section, we analytically derive the weighting factor introduced in Eq. (10). We start from the azimuthal
 1224 distribution of a particle that follows the expression:

$$P(\phi - \Psi) = \epsilon(\phi)(1 + 2v_2 \cos 2(\phi - \Psi)) \quad (\text{A1})$$

1225 where ϕ is the azimuthal angle of the particle, Ψ is the reaction plane azimuthal angle of the event and $\epsilon(\phi)$ is the
 1226 detection efficiency of the spectrometer at ϕ .

1227 The $\Delta\phi$ distribution of any two particles in the same event (foreground pairs) can be calculated as:

$$\begin{aligned} P_{FG}(\Delta\phi) & \quad (\text{A2}) \\ &= \frac{1}{\pi} \int_{-\pi/2}^{\pi/2} d\Psi \int_{\phi_1 - \phi_2 = \Delta\phi} d\phi_1 d\phi_2 P(\phi_1 - \Psi) P(\phi_2 - \Psi) \\ &= \frac{1}{\pi} \int_{-\pi/2}^{\pi/2} d\Psi \int_{-\pi}^{\pi} d\phi_1 P(\phi_1 - \Psi) P(\phi_1 + \Delta\phi - \Psi) \end{aligned}$$

1228 Replacing $P(\phi - \Psi)$ by its expression in (A1) allows one to write P_{FG} as the sum of four integrals:

$$P_{FG}(\Delta\phi) = \frac{1}{\pi} \int_{-\pi/2}^{\pi/2} d\Psi \int_{-\pi}^{\pi} d\phi_1 (A + B + C + D) \quad (\text{A3})$$

$$A = \epsilon(\phi_1)\epsilon(\phi_1 + \Delta\phi) \quad (\text{A4})$$

1229

$$B = 2v_2\epsilon(\phi_1)\epsilon(\phi_1 + \Delta\phi) \cos 2(\phi_1 - \Psi) \quad (\text{A5})$$

1230

$$C = 2v_2\epsilon(\phi_1)\epsilon(\phi_1 + \Delta\phi) \cos 2(\phi_1 + \Delta\phi - \Psi) \quad (\text{A6})$$

$$\begin{aligned} D &= 4v_2v_2\epsilon(\phi_1)\epsilon(\phi_1 + \Delta\phi)(\cos 2(\phi_1 - \Psi)) \\ &\quad \times (\cos 2(\phi_1 + \Delta\phi - \Psi)) \end{aligned} \quad (\text{A7})$$

1231 It is easy to show that the integrals of B and C are equal to 0 and the integral of D leads to:

$$\begin{aligned} \frac{1}{\pi} \int_{-\pi/2}^{\pi/2} d\Psi \int_{-\pi}^{\pi} d\phi_1 D &= 2v_2v_2 \cos 2\Delta\phi \\ &\quad \times \int_{-\pi}^{\pi} \epsilon(\phi_1)\epsilon(\phi_1 + \Delta\phi) \end{aligned} \quad (\text{A8})$$

1232 Therefore,

$$P_{FG}(\Delta\phi) = \left(\int_{-\pi}^{\pi} d\phi_1 \epsilon(\phi_1) \epsilon(\phi_1 + \Delta\phi) \right) \times (1 + 2v_2 v_2 \cos 2\Delta\phi) \quad (\text{A9})$$

1233 In a similar way one can calculate the $\Delta\phi$ distribution of mixed BG pairs produced without reaction plane binning:

$$P_{MIX}(\Delta\phi) = \frac{1}{\pi^2} \int_{-\pi/2}^{\pi/2} d\Psi_1 \int_{-\pi/2}^{\pi/2} d\Psi_2 \int_{\phi_1 - \phi_2 + \Delta\phi} \times d\phi_1 d\phi_2 P(\phi_1 - \Psi_1) P(\phi_2 - \Psi_2) \quad (\text{A10})$$

1234 where $\phi_{1(2)}$ and $\Psi_{1(2)}$ represents the azimuthal angle of particle 1(2) and the reaction plane azimuthal angle of the
1235 events from which the particles are taken. Replacing $P(\phi - \Psi)$ by (A1):

$$P_{MIX}(\Delta\phi) = \frac{1}{\pi^2} \int_{-\pi/2}^{\pi/2} d\Psi_1 \int_{-\pi/2}^{\pi/2} d\Psi_2 \int_{\phi_1 - \phi_2 + \Delta\phi} \times d\phi_1 d\phi_2 (E + F + G + H) \quad (\text{A11})$$

1236

$$E = \epsilon(\phi_1) \epsilon(\phi_1 + \Delta\phi) \quad (\text{A12})$$

1237

$$F = 2v_2 \epsilon(\phi_1) \epsilon(\phi_1 + \Delta\phi) \cos 2(\phi_1 - \Psi_1) \quad (\text{A13})$$

$$G = 2v_2 \epsilon(\phi_1) \epsilon(\phi_1 + \Delta\phi) \cos 2(\phi_1 + \Delta\phi - \Psi_2) \quad (\text{A14})$$

1238

$$H = 4v_2 v_2 \epsilon(\phi_1) \epsilon(\phi_1 + \Delta\phi) \cos 2(\phi_1 - \Psi_1) \times \cos 2(\phi_1 + \Delta\phi - \Psi_2) \quad (\text{A15})$$

1239 Because F , G and H are again easily proved to be 0, $P_{MIX}(\Delta\phi)$ can now be written as:

$$P_{MIX}(\Delta\phi) = \int_{-\pi}^{\pi} d\phi_1 \epsilon(\phi_1) \epsilon(\phi_1 + \Delta\phi) \quad (\text{A16})$$

1240 The weighting factor to introduce the flow correlation into the mixed BG pairs is then given by the ratio between
1241 Eq. (A10) and Eq. (A16):

$$w(\Delta\phi) = \frac{P_{FG}(\Delta\phi)}{P_{MIX}(\Delta\phi)} = 1 + 2v_2 v_2 \cos 2\Delta\phi \quad (\text{A17})$$

1242

Appendix B: Violation of $CB_{+-} = 2\sqrt{CB_{++}CB_{--}}$ due to flow

1243 In this appendix, we demonstrate that the combination of elliptic flow and nonuniform detection efficiency violates
1244 the well-known relation between unlike-sign and like-sign combinatorial background:

$$\langle CB_{+-} \rangle = 2\sqrt{\langle CB_{++} \rangle \langle CB_{--} \rangle} \quad (\text{B1})$$

1245 where $\langle CB_{+-/+ + / - -} \rangle$ are the unlike-sign and like-sign integral yields or average numbers of pairs per event.

1246 We start from the case without elliptic flow. Then, as proven in Ref [23], if e^+ and e^- are always produced in pairs
1247 independent of each other, the average number of unlike-sign and like-sign combinatorial pairs can be calculated as:

$$\langle CB_{+-} \rangle = [\varepsilon_p + \varepsilon_+(1 - \varepsilon_p)][\varepsilon_p + \varepsilon_-(1 - \varepsilon_p)] \times (\langle N^2 \rangle - \langle N \rangle) \quad (\text{B2})$$

$$\langle CB_{++} \rangle = \frac{1}{2}[\varepsilon_p + \varepsilon_+(1 - \varepsilon_p)]^2(\langle N^2 \rangle - \langle N \rangle) \quad (\text{B3})$$

$$\langle CB_{--} \rangle = \frac{1}{2}[\varepsilon_p + \varepsilon_-(1 - \varepsilon_p)]^2(\langle N^2 \rangle - \langle N \rangle) \quad (\text{B4})$$

1248 where ε_p is the probability to reconstruct both tracks of a pair, $\varepsilon_{+/-}$ is the probability to reconstruct only a single
1249 track and N is the number of pairs in an event.

1250 If $\varepsilon_{p/+/-}$ are assumed to be constants, Eq. (B1) can easily be proven from Eqs. (B2-B4). However, in the presence
1251 of elliptic flow, the probabilities $\varepsilon_{p/+/-}$ depend on the reaction plane angle:

$$\varepsilon_{p/+/-}(\psi) = \int d\phi \varepsilon_{p/+/-}(\phi)(1 + 2v_2 \cos(\phi - \psi)) \quad (\text{B5})$$

$$\langle CB_{+-}(\psi) \rangle = [A(\psi)B(\psi)] \times (\langle N^2 \rangle - \langle N \rangle) \quad (\text{B6})$$

$$\langle CB_{++}(\psi) \rangle = \frac{1}{2}[A(\psi)]^2 \times (\langle N^2 \rangle - \langle N \rangle) \quad (\text{B7})$$

$$\langle CB_{--}(\psi) \rangle = \frac{1}{2}[B(\psi)]^2 \times (\langle N^2 \rangle - \langle N \rangle) \quad (\text{B8})$$

$$A(\psi) = \varepsilon_p(\psi) + \varepsilon_+(\psi)(1 - \varepsilon_p(\psi)) \quad (\text{B9})$$

$$B(\psi) = \varepsilon_p(\psi) + \varepsilon_-(\psi)(1 - \varepsilon_p(\psi)) \quad (\text{B10})$$

1252 Taking the average over ψ within $[-\frac{\pi}{2}, \frac{\pi}{2}]$ gives:

$$\langle CB_{+-} \rangle = (\langle N^2 \rangle - \langle N \rangle) \int d\psi A(\psi)B(\psi) \quad (\text{B11})$$

$$\langle CB_{++} \rangle = \frac{1}{2}(\langle N^2 \rangle - \langle N \rangle) \int d\psi A(\psi)^2 \quad (\text{B12})$$

$$\langle CB_{--} \rangle = \frac{1}{2}(\langle N^2 \rangle - \langle N \rangle) \int d\psi B(\psi)^2 \quad (\text{B13})$$

1253 Using the Cauchy-Schwarz inequality, one obtains:

$$\left[\int d\psi A(\psi)B(\psi) \right]^2 \leq \int d\psi A(\psi)^2 \cdot \int d\psi B(\psi)^2 \quad (\text{B14})$$

1254 and consequently,

$$\langle CB_{+-} \rangle \leq 2\sqrt{\langle CB_{++} \rangle \langle CB_{--} \rangle} \quad (\text{B15})$$

1255

Appendix C: A second, independent analysis

1256 A subset of the data, 4.8×10^9 MB events, was analyzed by a second independent team. The second analysis follows
1257 the analysis strategy presented in Ref. [23], but includes the information provided by the HBD and other important
1258 improvements developed in this work.

1259 In this appendix we present the key features of the second analysis with an emphasis on the most important
1260 differences to the main analysis: (i) the HBD underlying event subtraction and cluster algorithm, (ii) the electron
1261 identification cuts and (iii) the background normalization. All analysis steps not explicitly mentioned are identical

1262 between the two analyses. In particular, identical cuts on the acceptance and inactive detector areas, and the same
 1263 pair cuts are applied. At the end of this appendix we discuss the efficiency correction and compare the results of both
 1264 analyses.

1265 The net number of photo electrons in an HBD cluster was calculated with a different algorithm than discussed
 1266 in Section IID, using a local estimate of the scintillation background rather than a module average. As an electron
 1267 typically fires three HBD readout cells, 3-cell triplets are used to initiate the cluster search. All possible triplets are
 1268 formed. The photo-electron background due to scintillation light is estimated by the median amplitude in the first
 1269 and second neighboring cells around the triplet. The background subtracted triplet charge is calculated as:

$$q_{net} = q_t - A_t \times \frac{\langle q_{fn} \rangle + \langle q_{sn} \rangle}{2} \quad (C1)$$

1270 where q_t is the total charge in the triplet, A_t the number of cells with charge in the triplet, and $\langle q_{fn} \rangle$, $\langle q_{sn} \rangle$ are
 1271 the median charge in the first and second neighboring cells, respectively. Only triplets with $0 < q_{net} < 60$ p.e. are
 1272 recorded.

1273 Electron candidates are projected to the HBD, and triplets within 1.5 cm of the track are merged to form a cluster.
 1274 The net charge of the cluster q_r is calculated starting from the sum of the charge of all cells in the cluster:

$$q_r = q_{totclust} - A_{clust} \times \frac{\langle q_{fn} \rangle + \langle q_{sn} \rangle}{2} \quad (C2)$$

1275 where $q_{totclust}$ is the sum of the charge of all cells in the cluster, A_{clust} is the number of cells in the cluster, $\langle q_{fn} \rangle$,
 1276 $\langle q_{sn} \rangle$ are again the median charge per cell in the first and second neighbors but now around the cluster.

1277 This analysis uses a number of sequential one-dimensional cuts to identify electrons. The variables used for the
 1278 electron identification are defined in Section III C 1. The following cuts are used:

- 1279 • $n0 > 2$: The exclusion of RICH photo-multipliers fired by background electrons (Section III C 2) is not used in
 1280 this analysis.
- 1281 • $disp < 5.5$ cm
- 1282 • $chi2/npe0 < 20$
- 1283 • $emcsdr < 3$
- 1284 • $|dep| < 2$
- 1285 • $m_{TOF}^2 < 1.5\sigma$: Calculated based on the time-of-flight measured by either the EMCal or the TOF-E detectors.
- 1286 • $10 < q_r < 40$ p.e.: Cluster charge as defined in Eq. (C2)

1287 With these cuts, a purity of the electron sample of 86% is achieved for the most central bin, which quickly increases
 1288 to above 99% for the most peripheral collisions.

1289 The combinatorial background is calculated by event mixing. We use the method outlined in [23], but included the
 1290 weighting for the azimuthal anisotropy as implemented in the main analysis and described in Section III E 2. For the
 1291 correlated background both analyses use the same MC simulations. For cross-pairs and jet-pairs the simulated pairs
 1292 were reanalyzed with the track selection cuts and HBD cluster algorithm mentioned above. The shapes of the mass
 1293 spectra are consistent within systematic uncertainties for the two analysis methods. For the electron-hadron and $B\bar{B}$
 1294 contributions the simulated pairs were not reanalyzed.

1295 The normalizations of all the background components were fitted simultaneously to the full mass and p_T range of
 1296 the like-sign spectra:

$$FG_{++--} = a_0 BG_{++--} + a_1 CP_{++--} + a_2 JP_{++--}^{same} + a_3 JP_{++--}^{opposite} + a_4 EH_{++--} + a_5 BB_{++--} \quad (C3)$$

1297 The parameters a_i are the individual normalization constants. Figure 37 shows the like-sign foreground divided by
 1298 the sum of all background sources for the five centrality classes. The uncertainty on the combinatorial background
 1299 normalization is shown as a gray band on each panel. No systematic deviation from unity is observed, indicating that
 1300 the sum of the different background components gives a sufficiently accurate description over the mass range up to
 1301 2 GeV/ c^2 with no indication of any shape variation within the shown uncertainties. Above 2 GeV/ c^2 the statistical
 1302 significance makes a comparison at the shown scale meaningless.

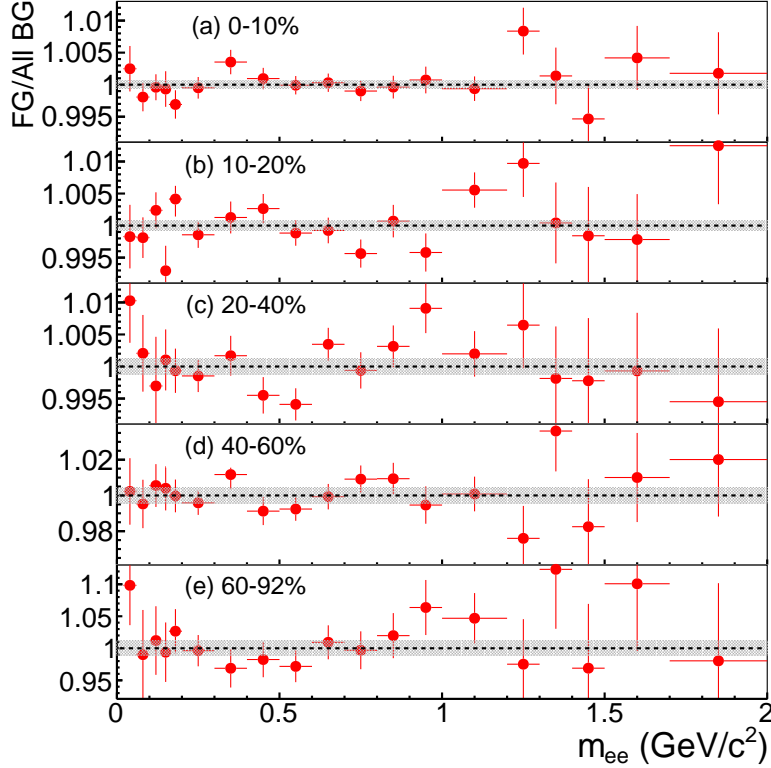


FIG. 37. (Color online) The ratio of the foreground like-sign pairs to the sum of combinatorial and correlated pair sources in centrality bins 0%–10%, 10%–20%, 20%–40%, 40%–60% and 60%–92%.

1303 After fixing the normalization of all background sources so that a satisfactory description of the like-sign pairs is
 1304 achieved, the analysis is extended to unlike-sign pairs. The normalizations for the unlike-sign cross-pairs, jet-pairs
 1305 and electron-hadron pairs are taken from Eq. (C4). For the combinatorial unlike-sign pairs we use unlike-sign mixed
 1306 event pairs. The normalization is also taken from Eq. (C4), but needs to be corrected to account for the different
 1307 effect of the pair cuts on like- and unlike-sign pairs as done in Ref. [23].

1308 To estimate the uncertainty on the raw yield due to the background subtraction one needs to consider the signal-
 1309 to-background ratio S/B . The uncertainties on the a_i are multiplied by B/S and added in quadrature. This results
 1310 in $\sim 55\%$ systematic uncertainties at $0.6 \text{ GeV}/c^2$ for MB collisions.

1311 We factorize the efficiency into 3 terms, which are determined separately.

$$\epsilon_{\text{pair}}^{\text{total}} = \epsilon_{\text{pair}} \cdot \epsilon_{\text{pair}}^{\text{TOF}} \cdot \epsilon_{\text{pair}}^{\text{embed}} \quad (\text{C4})$$

1312 The first factor describes the effect of all reconstruction algorithms and cuts except for the time-of-flight cut and the
 1313 centrality dependence of the reconstruction efficiency in the central arms, which are treated separately. It is obtained
 1314 by a MC simulation of e^+e^- pairs that are processed through the full PHENIX detector simulation, including the
 1315 HBD. The simulated HBD hits are embedded into real HBD data as discussed in Section III F. These events are then
 1316 analyzed with the same electron identification, fiducial, and pair cuts used in the independent analysis, with exception
 1317 of the time-of-flight cut. The systematic uncertainty of ϵ_{pair} is about 12%. It was determined from the measured
 1318 yield of pairs in the π^0 Dalitz decay region when varying electron identification cuts in a way that changes the raw
 1319 pair yields by factors between 0.5 and 1.5.

1320 The efficiency $\epsilon_{\text{pair}}^{\text{TOF}}$ is determined from tracks measured in peripheral collisions, where the hadron contamination is
 1321 negligible, by comparing data obtained with a 1.5σ cut to the case with no time-of-flight cut. We find that on average
 1322 the TOF efficiency for tracks is 93% above $0.4 \text{ GeV}/c$, but drops to 80% at $0.2 \text{ GeV}/c$ independent of centrality. This
 1323 drop results from a failure of the electronics to properly record time for low amplitude signals. In the main analysis
 1324 this issue was avoided by treating tracks with no time information separately. The systematic uncertainty due to this
 1325 cut is a few percent at $0.6 \text{ GeV}/c^2$.

1326 The efficiency $\epsilon_{\text{pair}}^{\text{embed}}$ was determined by embedding MC-simulation tracks into the data of all used central arm
 1327 detectors and analyzing these embedded tracks using the same cuts as used in the data. The values are found to be

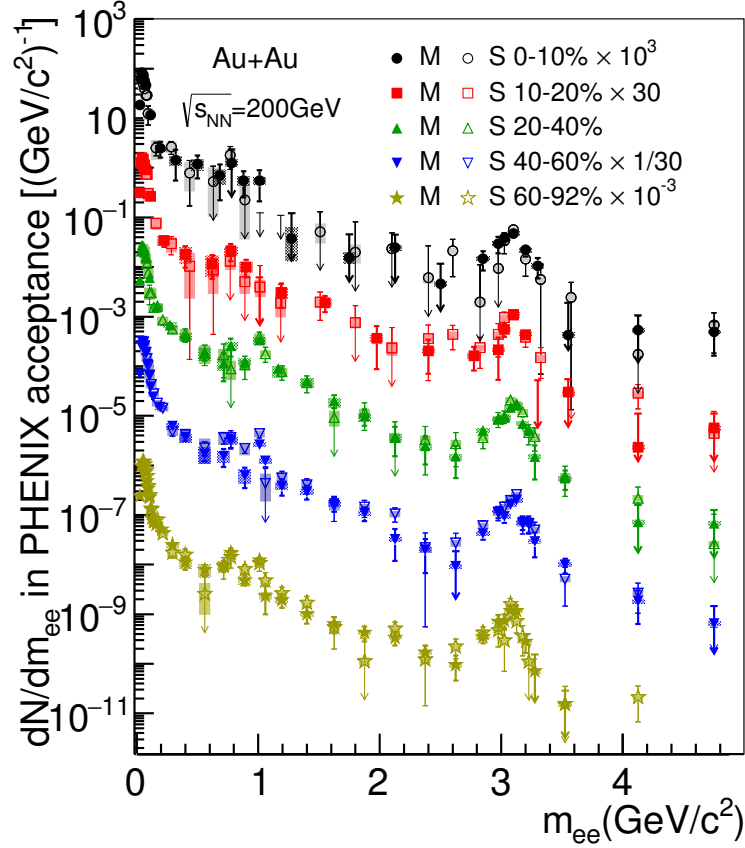


FIG. 38. (Color online) Comparison of final spectra from the main (M) and second (S) analyses.

1328 very similar to those derived in the main analysis. For central collisions an additional 8% systematic uncertainty is
 1329 added.

1330 Compared to the main analysis, the total reconstruction efficiency $\epsilon_{\text{pair}}^{\text{total}}$ is a factor of ~ 2 smaller for central collisions.
 1331 The difference drops to $\sim 30\%$ for the most peripheral collisions.

1332 The fully corrected mass spectra from the independent analysis are compared to those from the main analysis in
 1333 Fig. 38 for all five centrality bins. The results are consistent within uncertainties.

-
- 1334 [1] Edward V. Shuryak, “Quark-Gluon Plasma and Hadronic Production of Leptons, Photons and Psions,” Phys. Lett. B **78**,
 1335 150 (1978), [Yad. Fiz. **28**, 796 (1978)].
 1336 [2] P. Petreczky, “Lattice QCD at non-zero temperature,” J. Phys. G **39**, 093002 (2012).
 1337 [3] C. A. Dominguez, M. Loewe, and Y. Zhang, “Chiral symmetry restoration and deconfinement in QCD at finite tempera-
 1338 ture,” Phys. Rev. D **86**, 034030 (2012), [Erratum: Phys. Rev. DD90,no.3,039903(2014)].
 1339 [4] For recent theoretical and experimental reviews see the articles by R. Rapp *et al.* (arXiv:0901.3289) et al. and I. Tserruya
 1340 (arXiv:0903.0415) in Landolt-Borstein New Series **I/23A** (2010).
 1341 [5] G. Agakichiev *et al.* (CERES Collaboration), “Enhanced production of low mass electron pairs in 200 GeV/u S- Au
 1342 collisions at the CERN SPS,” Phys. Rev. Lett. **75**, 1272 (1995).
 1343 [6] G. Agakishiev *et al.* (CERES/NA45), “Low mass $e^+ e^-$ pair production in 158/A GeV Pb- Au collisions at the CERN
 1344 SPS, its dependence on multiplicity and transverse momentum,” Phys. Lett. B **422**, 405 (1998).
 1345 [7] D. Adamova *et al.*, “Modification of the rho-meson detected by low-mass electron-positron pairs in central Pb-Au collisions
 1346 at 158-A GeV/c,” Phys. Lett. B **666**, 425 (2008).
 1347 [8] D. Adamova *et al.* (CERES/NA45), “Enhanced production of low mass electron pairs in 40-AGeV Pb- Au collisions at
 1348 the CERN SPS,” Phys. Rev. Lett. **91**, 042301 (2003).

- [9] R. Arnaldi *et al.* (NA60 Collaboration), “First measurement of the rho spectral function in high-energy nuclear collisions,” *Phys. Rev. Lett.* **96**, 162302 (2006).
- [10] R. Arnaldi *et al.* (NA60 Collaboration), “Evidence for radial flow of thermal dileptons in high-energy nuclear collisions,” *Phys. Rev. Lett.* **100**, 022302 (2008).
- [11] R. Arnaldi *et al.* (NA60 Collaboration), “Evidence for the production of thermal-like muon pairs with masses above 1 GeV/ c^2 in 158-A GeV Indium-Indium Collisions,” *Eur. Phys. J. C* **59**, 607 (2009).
- [12] R. Arnaldi *et al.* (NA60 Collaboration), “NA60 results on thermal dimuons,” *Eur. Phys. J. C* **61**, 711 (2009).
- [13] H. van Hees and R. Rapp, “Dilepton Radiation at the CERN Super Proton Synchrotron,” *Nucl. Phys. A* **806**, 339 (2008).
- [14] H. van Hees and R. Rapp, “Comprehensive interpretation of thermal dileptons at the SPS,” *Phys. Rev. Lett.* **97**, 102301 (2006).
- [15] J. Ruppert, C. Gale, T. Renk, P. Lichard, and Joseph I. Kapusta, “Low mass dimuons produced in relativistic nuclear collisions,” *Phys. Rev. Lett.* **100**, 162301 (2008).
- [16] K. Dusling, D. Teaney, and I. Zahed, “Thermal dimuon yields at NA60 Collaboration,” *Phys. Rev. C* **75**, 024908 (2007).
- [17] E. L. Bratkovskaya, W. Cassing, and O. Linnyk, “Low mass dilepton production at ultrarelativistic energies,” *Phys. Lett. B* **670**, 428 (2009).
- [18] O. Linnyk, E. L. Bratkovskaya, V. Ozvenchuk, W. Cassing, and C. M. Ko, “Dilepton production in nucleus-nucleus collisions at top SPS energy within the Parton-Hadron-String Dynamics (PHSD) transport approach,” *Phys. Rev. C* **84**, 054917 (2011).
- [19] G. E. Brown and Mannque Rho, “Scaling effective Lagrangians in a dense medium,” *Phys. Rev. Lett.* **66**, 2720 (1991).
- [20] G. E. Brown and Mannque Rho, “Chiral restoration in hot and/or dense matter,” *Phys. Rept.* **269**, 333 (1996).
- [21] G.-Q. Li, C. M. Ko, and G. E. Brown, “Enhancement of low mass dileptons in heavy ion collisions,” *Phys. Rev. Lett.* **75**, 4007 (1995).
- [22] P. M. Hohler and R. Rapp, “Is ρ -Meson Melting Compatible with Chiral Restoration?” *Phys. Lett. B* **731**, 103 (2014).
- [23] A. Adare *et al.* (PHENIX Collaboration), “Detailed measurement of the e^+e^- pair continuum in $p+p$ and Au+Au collisions at $\sqrt{s_{NN}}=200$ GeV and implications for direct photon production,” *Phys. Rev. C* **81**, 034911 (2010).
- [24] O. Linnyk, W. Cassing, J. Manninen, E. L. Bratkovskaya, and C. M. Ko, “Analysis of dilepton production in Au+Au collisions at $\sqrt{s_{NN}}=200$ GeV within the Parton-Hadron-String Dynamics (PHSD) transport approach,” *Phys. Rev. C* **85**, 024910 (2012).
- [25] A. Kozlov, I. Ravinovich, Lev I. Shekhtman, Z. Fraenkel, M. Inuzuka, and I. Tserruya, “Development of a triple GEM UV photon detector operated in pure CF(4) for the PHENIX experiment,” *Nucl. Instrum. Methods Phys. Res., Sec. A* **523**, 345 (2004).
- [26] Z. Fraenkel *et al.*, “A Hadron blind detector for the PHENIX experiment at RHIC,” *Nucl. Instrum. Methods Phys. Res., Sec. A* **546**, 466 (2005).
- [27] W. Anderson *et al.*, “Design, Construction, Operation and Performance of a Hadron Blind Detector for the PHENIX Experiment,” *Nucl. Instrum. Methods Phys. Res., Sec. A* **646**, 35 (2011).
- [28] K. Adcox *et al.* (PHENIX Collaboration), “PHENIX detector overview,” *Nucl. Instrum. Methods Phys. Res., Sec. A* **499**, 469 (2003).
- [29] M. Allen *et al.* (PHENIX Collaboration), “PHENIX inner detectors,” *Nucl. Instrum. Methods Phys. Res., Sec. A* **499**, 549 (2003).
- [30] A. Adare *et al.* (PHENIX Collaboration), “Spectra and ratios of identified particles in Au+Au and d +Au collisions at $\sqrt{s_{NN}}=200$ GeV,” *Phys. Rev. C* **88**, 024906 (2013).
- [31] S. H. Aronson *et al.* (PHENIX Collaboration), “PHENIX magnet system,” *Nucl. Instrum. Methods Phys. Res., Sec. A* **499**, 480 (2003).
- [32] K. Adcox *et al.* (PHENIX Collaboration), “PHENIX central arm tracking detectors,” *Nucl. Instrum. Methods Phys. Res., Sec. A* **499**, 489 (2003).
- [33] K. Adcox *et al.*, “Construction and performance of the PHENIX pad chambers,” *Nucl. Instrum. Methods Phys. Res., Sec. A* **497**, 263 (2003).
- [34] Y. Akiba *et al.*, “Ring imaging Cherenkov detector of PHENIX experiment at RHIC,” *Proceedings, 3rd International Workshop on Ring Imaging Cherenkov Detectors: Advances in Cherenkov light imaging techniques and applications (RICH 1998)*, *Nucl. Instrum. Methods Phys. Res., Sec. A* **433**, 143 (1999).
- [35] L. Aphecetche *et al.* (PHENIX Collaboration), “PHENIX calorimeter,” *Nucl. Instrum. Methods Phys. Res., Sec. A* **499**, 521 (2003).
- [36] M. Aizawa *et al.* (PHENIX Collaboration), “PHENIX central arm particle ID detectors,” *Nucl. Instrum. Methods Phys. Res., Sec. A* **499**, 508 (2003).
- [37] F. Sauli, “GEM: A new concept for electron amplification in gas detectors,” *Nucl. Instrum. Methods Phys. Res., Sec. A* **386**, 531 (1997).
- [38] B. Azmoun *et al.*, “A Study of Gain Stability and Charging Effects in GEM Foils,” *Proceedings, 2006 IEEE Nuclear Science Symposium and Medical Imaging Conference (NSS/MIC 2006)*, *IEEE Nucl. Sci. Symp. Conf. Rec.* **6**, 3847–3851 (2006).
- [39] M. Makek (PHENIX Collaboration), “Measurement of low mass dielectrons with the HBD upgrade of PHENIX Collaboration,” *Quark matter. Proceedings, 22nd International Conference on Ultra-Relativistic Nucleus-Nucleus Collisions, Quark Matter 2011, Annecy, France, May 23-28, 2011*, *J. Phys. G* **38**, 124135 (2011).
- [40] M. L. Miller, K. Reygers, S. J. Sanders, and Peter Steinberg, “Glauber modeling in high energy nuclear collisions,” *Ann. Rev. Nucl. Part. Sci.* **57**, 205 (2007).
- [41] S. S. Adler *et al.* (PHENIX Collaboration), “Transverse-energy distributions at midrapidity in $p+p$, $d+Au$, and Au+Au

- collisions at $\sqrt{s_{NN}}=62.4-200$ GeV and implications for particle-production models,” Phys. Rev. C **89**, 044905 (2014).
- [42] C. Delaere, R. Brun, and F. Rademakers, “Neural Network TMultiLayerPerceptron: ROOT Data Analysis Framework,” <https://root.cern.ch/root/html/TMultiLayerPerceptron.html>.
- [43] S. S. Adler *et al.* (PHENIX Collaboration), “Measurement of single electron event anisotropy in Au+Au collisions at $\sqrt{s_{NN}} = 200$ GeV,” Phys. Rev. C **72**, 024901 (2005).
- [44] A. Adare *et al.* (PHENIX Collaboration), “Heavy Quark Production in $p + p$ and Energy Loss and Flow of Heavy Quarks in Au+Au Collisions at $\sqrt{s_{NN}}=200$ GeV,” Phys. Rev. C **84**, 044905 (2011).
- [45] A. Adare *et al.* (PHENIX Collaboration), “Measurements of Higher-Order Flow Harmonics in Au+Au Collisions at $\sqrt{s_{NN}}=200$ GeV,” Phys. Rev. Lett. **107**, 252301 (2011).
- [46] T. Sjostrand, P. Eden, C. Friberg, L. Lonnblad, G. Miu, M. Stephen, and E. Norrbin, “High-energy physics event generation with PYTHIA 6.1,” Comput. Phys. Commun. **135**, 238 (2001).
- [47] A. Adare *et al.* (PHENIX Collaboration), “Inclusive cross-section and double helicity asymmetry for π^0 production in $p + p$ collisions at $\sqrt{s}=200$ GeV: Implications for the polarized gluon distribution in the proton,” Phys. Rev. D **76**, 051106 (2007).
- [48] A. Adare *et al.* (PHENIX Collaboration), “Dihadron azimuthal correlations in Au+Au collisions at $\sqrt{s_{NN}} = 200$ GeV,” Phys. Rev. C **78**, 014901 (2008).
- [49] GEANT Users Guide, 3.15, CERN Program Library.
- [50] A. Adare *et al.* (PHENIX Collaboration), “Dilepton mass spectra in p+p collisions at $\sqrt{s} = 200$ GeV and the contribution from open charm,” Phys. Lett. B **670**, 313 (2009).
- [51] S. Frixione and B. R. Webber, “Matching NLO QCD computations and parton shower simulations,” J. High Energy Phys. **06**, 029 (2002).
- [52] S. Frixione, P. Nason, and B. R. Webber, “Matching NLO QCD and parton showers in heavy flavor production,” J. High Energy Phys. **08**, 007 (2003).
- [53] S. S. Adler *et al.* (PHENIX Collaboration), “A Detailed Study of High-p(T) Neutral Pion Suppression and Azimuthal Anisotropy in Au+Au Collisions at $\sqrt{s_{NN}} = 200$ GeV,” Phys. Rev. C **76**, 034904 (2007).
- [54] A. Adare *et al.* (PHENIX Collaboration), “Suppression pattern of neutral pions at high transverse momentum in Au + Au collisions at $\sqrt{s_{NN}} = 200$ GeV and constraints on medium transport coefficients,” Phys. Rev. Lett. **101**, 232301 (2008).
- [55] S. S. Adler *et al.* (PHENIX Collaboration), “Identified charged particle spectra and yields in Au+Au collisions at $\sqrt{s_{NN}} =$,” Phys. Rev. C **69**, 034909 (2004).
- [56] A. Adare *et al.*, “Production of ω mesons in $p + p$, d+Au, Cu+Cu, and Au+Au collisions at $\sqrt{s_{NN}} = 200$ GeV,” Phys. Rev. C **84**, 044902 (2011).
- [57] A. Adare *et al.* (PHENIX Collaboration), “Nuclear modification factors of ϕ mesons in d+Au, Cu+Cu and Au+Au collisions at $\sqrt{s_{NN}} = 200$ GeV,” Phys. Rev. C **83**, 024909 (2011).
- [58] A. Adare *et al.* (PHENIX Collaboration), “Transverse momentum dependence of meson suppression η suppression in Au+Au collisions at $\sqrt{s_{NN}}= 200$ GeV,” Phys. Rev. C **82**, 011902 (2010).
- [59] A. Adare *et al.* (PHENIX Collaboration), “ J/ψ Production vs Centrality, Transverse Momentum, and Rapidity in Au+Au Collisions at $\sqrt{s_{NN}}=200$ GeV,” Phys. Rev. Lett. **98**, 232301 (2007).
- [60] T. Sjostrand, S. Mrenna, and P. Z. Skands, “PYTHIA 6.4 Phys. and Manual,” J. High Energy Phys. **05**, 026 (2006).
- [61] G. Corcella, I. G. Knowles, G. Marchesini, S. Moretti, K. Odagiri, P. Richardson, M. H. Seymour, and B. R. Webber, “HERWIG 6: An Event generator for hadron emission reactions with interfering gluons (including supersymmetric processes),” J. High Energy Phys. **01**, 010 (2001).
- [62] A. Adare *et al.* (PHENIX Collaboration), “Cross section for $b\bar{b}$ production via dielectrons in d+Au collisions at $\sqrt{s_{NN}}=200$ GeV,” Phys. Rev. C **91**, 014907 (2015).
- [63] A. Adare *et al.* (PHENIX Collaboration), “Enhanced production of direct photons in Au+Au collisions at $\sqrt{s_{NN}}=200$ GeV and implications for the initial temperature,” Phys. Rev. Lett. **104**, 132301 (2010).
- [64] A. Adare *et al.* (PHENIX Collaboration), “Centrality dependence of low-momentum direct-photon production in Au+Au collisions at $\sqrt{s_{NN}}=200$ GeV,” Phys. Rev. C **91**, 064904 (2015).
- [65] A. Adare *et al.* (PHENIX Collaboration), “Ground and excited charmonium state production in $p+p$ collisions at $\sqrt{s} = 200$ GeV,” Phys. Rev. D **85**, 092004 (2012).
- [66] L. Adamczyk *et al.* (STAR Collaboration), “Dielectron Mass Spectra from Au+Au Collisions at $\sqrt{s_{NN}} = 200$ GeV,” Phys. Rev. Lett. **113**, 022301 (2014), [Addendum: Phys. Rev. Lett. **113** 049903E (2014)].
- [67] L. Adamczyk *et al.* (STAR Collaboration), “Measurements of Dielectron Production in Au+Au Collisions at $\sqrt{s_{NN}} = 200$ GeV from the STAR Experiment,” Phys. Rev. C **92**, 024912 (2015).
- [68] P. V. Ruuskanen, “Electromagnetic probes of quark- gluon plasma in relativistic heavy ion collisions,” *Quark matter '91. Proceedings, 9th International Conference on UltraRelativistic Nucleus-Nucleus Collisions, Gatlinburg, USA, November 11-15, 1991*, Nucl. Phys. A **544**, 169 (1992).
- [69] S. Turbide, R. Rapp, and C. Gale, “Hadronic production of thermal photons,” Phys. Rev. C **69**, 014903 (2004).
- [70] A. Adare *et al.* (PHENIX Collaboration), “Energy Loss and Flow of Heavy Quarks in Au+Au Collisions at $\sqrt{s_{NN}} = 200$ GeV,” Phys. Rev. Lett. **98**, 172301 (2007).
- [71] R. Rapp and J. Wambach, “Low mass dileptons at the CERN SPS: Evidence for chiral restoration?” Eur. Phys. J. C **6**, 415 (1999).
- [72] R. Rapp, “Signatures of thermal dilepton radiation at RHIC,” Phys. Rev. C **63**, 054907 (2001).
- [73] R. Rapp, “Dilepton Spectroscopy of QCD Matter at Collider Energies,” Adv. High Energy Phys. **2013**, 148253 (2013).
- [74] R. Rapp, private communication, based on [71, 72].